

# **Opto-mechanics in a Michelson-Sagnac interferometer**

Von der QUEST-Leibniz-Forschungsschule  
der Gottfried Wilhelm Leibniz Universität Hannover  
zur Erlangung des Grades

**Doktor der Naturwissenschaften  
Dr. rer. nat.**

genehmigte Dissertation  
von

**Dipl.-Phys. Henning Kaufer**

geboren am 18. November 1983 in Lehrte

2014

Referent: Prof. Dr. Roman Schnabel  
Korreferent: Prof. Dr. Karsten Danzmann  
Tag der Promotion: 30. August 2013

In any field, find the strangest thing  
and then explore it.

*John Archibald Wheeler*



## Abstract

The quantum nature of light associates the process of optical reflection with the transfer of photon momentum. As the number of photons in a coherent and even in the vacuum state is subject to quantum fluctuations, this opto-mechanical interaction imposes a fundamental limit in high-precision laser interferometric setups such as gravitational wave detectors. In order to develop and test experimental strategies to minimise the disturbing back-action in these detectors, smaller, less complex experiments with perceivable measurement back-action effects are appropriate. Devoted opto-mechanical experiments are typically carried out in linear optical cavities.

This thesis presents a novel approach to enable opto-mechanical interaction, using a signal-recycled Michelson-Sagnac laser interferometer. In this topology, the interferometer acts as a compound mirror in an effective cavity. Its reflectivity and therefore, the effective cavity finesse is modified by the displacement of a micro-mechanical oscillator inside the interferometer, giving rise to a *dissipative coupling*.

In the framework of this thesis, a Michelson-Sagnac interferometer was realised and characterised within a high-vacuum system. A shot noise limited displacement sensitivity of  $1.9 \cdot 10^{-16} \text{ m}/\sqrt{\text{Hz}}$  was achieved for frequencies above 60 kHz. Subsequently, the interferometer was extended by a high-reflective mirror in the interferometer output. The resulting topology is described analytically and was investigated in the experiment. It features a complex optical spring with non-canonical properties such as the existence of a conditional instability, which could be observed in the experiments. Moreover, parametric heating and optical damping of the oscillator were observed, reducing the oscillator's effective quality factor by more than two orders of magnitude.

In second experiment, a Michelson-Sagnac interferometer was operated at cryogenic temperatures as low as 8 K. In this way, the oscillator thermal noise around the mechanical resonance frequency was reduced significantly and the interferometer displacement sensitivity could thus be enhanced.

The results presented in this thesis demonstrate the potential of the Michelson-Sagnac topology and render it a unique addition to the toolbox of opto-mechanical experiments.

**Keywords:** SiN membranes, opto-mechanics, cryogenics



## Kurzfassung

Der Teilchencharakter des Lichts assoziiert den Prozess optischer Reflexion mit einem Impulsübertrag des Photons. Die Anzahl der Photonen in einem kohärenten Zustand unterliegt Quantenfluktuationen, was zu einer fundamentalen Empfindlichkeitsgrenze in hochpräzisen Laserinterferometern wie Gravitationswellendetektoren führt. Zur Entwicklung und zum Test experimenteller Strategien, um den störenden Einfluss der Rückwirkung der Messung zu verringern sind weniger komplexe Experimente erforderlich, in welchen die Messrückwirkung ebenfalls beobachtbar ist. Solche, opto-mechanischen Experimente werden typischerweise mit linearen Resonatoren realisiert.

Diese Arbeit präsentiert einen neuen Ansatz zur Erzeugung opto-mechanischer Wechselwirkungen - innerhalb eines signalüberhöhten Michelson-Sagnac Interferometers. Dieses übernimmt die Funktion eines Quasi-spiegels innerhalb eines effektiven Resonators. Dessen Finnesse wird durch die Auslenkung eines mikro-mechanischen Oszillators innerhalb des Interferometers modifiziert, was zu einer *dissipativen Kopplung* führt.

In dieser Arbeit wurde ein Michelson-Sagnac Interferometer realisiert und innerhalb eines Hochvakuum-Systems charakterisiert. Eine Schrot-rausch-begrenzte Positionsempfindlichkeit von  $1.9 \cdot 10^{-16} \text{ m}/\sqrt{\text{Hz}}$  konnte für Frequenzen oberhalb von 60 kHz erreicht werden. Ein hoch reflektierender Spiegel wurde im Ausgang des Interferometers installiert und die entstandene Topologie analytisch sowie experimentell untersucht. Die resultierende optische Feder besitzt nicht-kanonische Eigenschaften, wie die Existenz einer bedingten Instabilität, die im Experiment beobachtet wurde. Neben parametrischem Heizen war es möglich, die mechanische Güte des Oszillators durch optische Dämpfung um mehr als zwei Größenordnungen zu reduzieren.

In einem zweiten Experiment wurde ein Michelson-Sagnac Interferometer innerhalb eines kryogenen Systems bei einer Temperatur von 8 K betrieben. So konnte das thermisch getriebene Positionsrauschen um die mechanische Resonanzfrequenz des Oszillators erheblich verringert und die Positionsgenauigkeit der Messung gesteigert werden. Die Ergebnisse dieser Arbeit demonstrieren das Potential der Michelson-Sagnac Topologie, welche die Konzepte bisheriger opto-mechanischer Experimente in einzigartiger Weise erweitert.

**Schlagnworte:** SiN Membranen, Opto-mechanik, Kryogenik





# Contents

<b>Contents</b>	<b>IX</b>
<b>List of Figures</b>	<b>XIII</b>
<b>List of Tables</b>	<b>XVII</b>
<b>List of Abbreviations</b>	<b>XIX</b>
<b>1 Introduction</b>	<b>1</b>
<b>2 Basic concepts of quantum interferometry</b>	<b>7</b>
2.1 Spectral density . . . . .	7
2.2 Quantisation of light fields . . . . .	9
2.3 Performing measurements on light fields . . . . .	13
2.3.1 Direct detection . . . . .	13
2.3.2 Balanced homodyne detection . . . . .	13
<b>3 The mechanical oscillator</b>	<b>15</b>
3.1 The oscillator transfer function . . . . .	15
3.2 Mechanical quality factor . . . . .	18
3.3 Thermal noise . . . . .	19
3.4 Silicon Nitride membrane . . . . .	21
3.4.1 Optical properties . . . . .	21
3.4.2 Modes of motion and effective mass . . . . .	22
3.4.3 Resonance frequencies . . . . .	24
3.4.4 Membrane mechanical quality factor . . . . .	25
<b>4 Michelson-Sagnac interferometer</b>	<b>27</b>
4.1 Interferometer topology . . . . .	27
4.2 Interferometric signals and noise . . . . .	32
4.2.1 The shot noise limit . . . . .	32
4.2.2 Quantum back-action noise . . . . .	33
4.2.3 Standard quantum limit . . . . .	35

## CONTENTS

4.3	Influence and suppression of laser noise . . . . .	38
4.3.1	Interferometer contrast . . . . .	38
4.3.2	Interferometer arm length differences . . . . .	40
4.3.3	Laser frequency noise . . . . .	41
4.3.4	Laser intensity noise . . . . .	43
4.3.5	Laser light preparation . . . . .	46
4.4	Realisation of the Michelson-Sagnac interferometer . . . . .	48
4.4.1	Interferometer design . . . . .	50
4.4.2	Vibration isolation . . . . .	51
4.4.3	Membrane holding . . . . .	53
4.4.4	Interferometer alignment . . . . .	54
4.4.5	Vacuum requirements . . . . .	56
4.4.6	Remote alignment . . . . .	57
4.5	Interferometer calibration . . . . .	58
4.5.1	Calibration via the interferometer fringe . . . . .	58
4.5.2	Obtaining the membrane displacement spectrum . . . . .	59
4.5.3	Calibration using a marker peak . . . . .	61
4.6	Achieved displacement sensitivity . . . . .	61
4.6.1	Readout with a single photo detector . . . . .	61
4.6.2	Balanced homodyne readout . . . . .	63
4.7	Chapter summary . . . . .	66
<b>5</b>	<b>Signal-recycled Michelson-Sagnac interferometer</b>	<b>69</b>
5.1	Optical cavity . . . . .	69
5.1.1	Effective cavity output power . . . . .	73
5.1.2	Signal-Recycling . . . . .	74
5.1.3	Design considerations for the effective cavity . . . . .	78
5.1.4	The impact of optical losses . . . . .	79
5.1.5	Loss in the cavity . . . . .	81
5.2	Realisation of the recycled interferometer . . . . .	82
5.2.1	Cavity length stabilisation scheme . . . . .	83
5.2.2	Effective cavity optical linewidth . . . . .	86
5.2.3	Displacement sensitivity . . . . .	87
5.3	Opto-mechanical interaction . . . . .	89
5.3.1	Parametric instability . . . . .	91
5.3.2	Optical cooling . . . . .	92
5.3.3	Optical spring in the Michelson-Sagnac interferometer . . . . .	95
5.3.4	Conditional instability . . . . .	98
5.3.5	Observation of optical damping . . . . .	102

5.3.6	Reduction of interferometer loss . . . . .	106
5.4	Chapter summary . . . . .	107
<b>6</b>	<b>Cryogenic cooling of the interferometer</b>	<b>109</b>
6.1	The need for low temperatures . . . . .	109
6.2	Concepts for cryogenic cooling . . . . .	110
6.3	The Gifford-McMahon cryocooler . . . . .	111
6.3.1	Thermodynamic cycle . . . . .	112
6.3.2	Cryocooler components . . . . .	114
6.4	Interferometer prototype for cryogenic environment . .	115
6.4.1	Membrane alignment and positioning . . . . .	117
6.4.2	The optical setup . . . . .	119
6.4.3	Interferometer installation procedure . . . . .	120
6.5	Results . . . . .	123
6.5.1	Cryogenic interferometer performance . . . . .	124
6.5.2	Influence of low temperatures on the membrane	126
6.5.3	Identified problems . . . . .	129
6.5.4	Next steps . . . . .	130
6.6	Chapter summary . . . . .	130
<b>7</b>	<b>Summary</b>	<b>133</b>
<b>8</b>	<b>Appendix A</b>	<b>135</b>
8.1	Finesse Simulation File . . . . .	135
8.2	Matlab Files . . . . .	138
	<b>Bibliography</b>	<b>141</b>
	<b>List of publications</b>	<b>155</b>
	<b>Acknowledgements</b>	<b>157</b>
	<b>Curriculum Vitae</b>	<b>159</b>



## List of Figures

1.1	Second generation GW detector schematic and anticipated Advanced LIGO strain sensitivity . . . . .	2
2.1	Balanced homodyne detection scheme . . . . .	14
3.1	Oscillator transfer function . . . . .	19
3.2	Comparison of structural and viscous damping . . . . .	20
3.3	SiN membrane and silicon frame . . . . .	21
3.4	SiN membrane power reflectivity for different optical wavelengths . . . . .	22
3.5	Graphical illustration of the membrane fundamental oscillation mode . . . . .	23
3.6	Higher-order mode spectrum . . . . .	24
3.7	Ring-down measurement . . . . .	26
4.1	Michelson-Sagnac Interferometer . . . . .	28
4.2	Interferometer output power . . . . .	30
4.3	Quantum and thermal noise . . . . .	34
4.4	Noise budget at cryogenic temperatures, with signal-recycling . . . . .	35
4.5	Illustration of interferometric contrast . . . . .	38
4.6	Interferometer contrast influence to achievable displacement sensitivity . . . . .	39
4.7	Interferometer contrast with arm length difference . . . . .	40
4.8	Mephisto NPRO laser frequency noise projection into apparent length noise for various interferometer arm length inequalities . . . . .	42
4.9	Laser intensity stabilisation performance . . . . .	45
4.10	Mach-Zehnder and EOAM power stabilisation schemes . . . . .	46
4.11	Schematic of the laser light preparation . . . . .	47
4.12	Laser intensity stabilisation performance . . . . .	47
4.13	Interferometer output spectrum in 2010 . . . . .	49
4.14	Typical spectrum prior to interferometer isolation . . . . .	49
4.15	CAD Design for the Michelson-Sagnac Interferometer . . . . .	50

## LIST OF FIGURES

4.16	Passive isolation stages of the interferometer . . . . .	51
4.17	Performance of the passive isolation of the interferometer baseplate in vertical direction . . . . .	52
4.18	Schematic of the membrane holder for the room temperature experiment . . . . .	53
4.19	Sagnac interferometer alignment . . . . .	54
4.20	Alignment of the Michelson-Sagnac interferometer . . . . .	55
4.21	Q-factor as function of environmental pressure . . . . .	56
4.22	Vacuum setup for the experiment . . . . .	58
4.23	The redesigned Michelson-Sagnac interferometer . . . . .	59
4.24	Interferometer fringe and output power derivative . . . . .	60
4.25	Spectrum around the fundamental mode . . . . .	62
4.26	Balanced homodyne detector locking scheme for the homodyne phase $\theta$ to the amplitude quadrature . . . . .	63
4.27	Homodyne detector DC Signal and demodulated error signal . . . . .	64
4.28	Homodyne output spectrum . . . . .	65
4.29	Broadband homodyne output spectrum . . . . .	66
4.30	Variation of the homodyne read out quadrature . . . . .	67
5.1	Schematic of a two mirror cavity . . . . .	70
5.2	Cavity resonance peaks . . . . .	72
5.3	Schematic of the signal-recycled Michelson-Sagnac effective cavity . . . . .	73
5.4	Normalised output power of the recycled Michelson-Sagnac interferometer as function of membrane and mirror detuning . . . . .	74
5.5	Normalised transmitted power through signal recycling cavity . . . . .	75
5.6	Scans of the signal-recycling cavity length and the membrane position . . . . .	76
5.7	Displacement sensitivity for various signal-recycling mirror reflectivities and detunings . . . . .	77
5.8	Signal-recycling gain as function of recycling mirror transmissivity including loss . . . . .	80
5.9	Optical loss channels within the cavity . . . . .	82
5.10	Signal-recycled Michelson-Sagnac with balanced homodyne readout . . . . .	83
5.11	SR Cavity output power with $R_{\text{SR}} = 99.97\%$ . . . . .	84
5.12	Cavity output power and derivative . . . . .	85

*LIST OF FIGURES*

5.13	Schematic setup for measuring the effective cavity linewidth . . . . .	86
5.14	Minimum measured effective cavity linewidth . . . . .	87
5.15	Displacement sensitivity of the recycled interferometer and transmitted optical power fraction in case of loss and no loss . . . . .	88
5.16	Single-ended, opto-mechanical cavity . . . . .	90
5.17	Scans of the signal-recycling cavity length with different velocities . . . . .	93
5.18	Signal-recycled Michelson-Sagnac interferometer . . . . .	95
5.19	Optical spring in the Michelson-Sagnac interferometer . . . . .	97
5.20	Modification of the membrane mechanical quality factor . . . . .	98
5.21	Conditional instability and parametric instability on two different sides of signal-recycling cavity resonance . . . . .	99
5.22	Conditional instability threshold . . . . .	101
5.23	Interferometer output spectra with recycling-mirror . . . . .	102
5.24	Numerical calculation of the optical damping for the experimental parameters . . . . .	103
5.25	Calibrated output power spectrum with recycling mirror close to cavity resonance . . . . .	105
5.26	Modification of the mechanical quality factor with reduced optical losses . . . . .	107
6.1	Gifford McMahon cycle . . . . .	113
6.2	Schematic of the cryogenic system . . . . .	116
6.3	CAD Design of the cryogenic interferometer . . . . .	117
6.4	Cryogenic membrane alignment . . . . .	118
6.5	RIN measurement of the 1550 nm laser . . . . .	120
6.6	Installation procedure into the cryo chamber . . . . .	121
6.7	Photos of the cryocooler setup . . . . .	122
6.8	Cryocooler cool down sequence with installed interferometer . . . . .	123
6.9	Switching the compressor off / on . . . . .	124
6.10	Schematic of the cryogenic experiment . . . . .	125
6.11	Drift of mechanical resonance frequencies due to reduction of oscillator temperature . . . . .	126
6.12	SiN membrane ring-down measurements at cryogenic and close-to ambient temperatures . . . . .	127
6.13	Displacement spectrum at various temperatures . . . . .	128
6.14	CCD output for the cryogenic interferometer . . . . .	129





## List of Tables

3.1	Relevant SiN membrane parameters for the membrane used in the 1064 nm and 1550 nm cryogenic experiment	26
5.1	Effective quality factors $Q_{\text{eff}}$ due to optical damping of the oscillator fundamental mode for $P_{\text{in}} = 10$ mW, 50 mW and 200 mW . . . . .	103
6.1	<i>Attocube</i> remote positioner data for membrane alignment and positioning at cryogenic temperatures . . . .	119



## List of Abbreviations

AC	Alternating Current
AEI	Albert Einstein Institute (in Hannover)
AR	Anti-Reflective
BS	Beam Splitter
CAD	Computer Aided Design
CCD	Charge-Coupled Device
CLIO	Cryogenic Laser Interferometer Observatory
DC	Direct Current
DFT	Discrete Fourier Transform
EOAM	Electro-Optic Amplitude Modulator
EOM	Electro-Optic Modulator
FFT	Fast Fourier Transform
FSR	Free Spectral Range
FWHM	Full-Width at Half Maximum
GM	Gifford-McMahon
GW	Gravitational Wave Detector
HR	High-Reflective
HV	High Voltage
HWHM	Half-Width at Half Maximum
ifo	Interferometer
KAGRA	Kamioka Gravitational Wave Detector

## *List of Abbreviations*

LIGO	Laser Interferometer Gravitational Wave Observatory
LO	Local Oscillator
LP	Low-Pass
MC	Mode Cleaner
Nd:YAG	Neodymium-Doped Yttrium Aluminium Garnet
OB	Optical Bench
OPD	Optical Path length Difference
PBS	Polarising Beam Splitter
PC	Personal Computer
PD	Photodetector
PI	Physics Instruments
PI	Proportional-Integral (controller)
PID	proportional-integral-derivative
PLL	Phase-Locked Loop
pp	peak-to-peak
ppm	parts per million
QPD	Quadrant Photodiode
RBW	Resolution Bandwidth
RF	Radio Frequency
RIN	Relative Intensity Noise
SiN	Silicon Nitride
SQL	Standard Quantum Limit
SR	Signal-recycling
SRM	Signal Recycling Mirror
TMP	Turbo Molecular Pump

# 1

## Chapter 1

### Introduction

In his Nobel prize rewarded work, Albert Einstein explained the photo electric effect by assuming that the physical phenomenon 'light' is quantised [1]. A quantum of light is called a photon. The energy of a single photon is  $E_{\text{ph}} = \hbar\omega$ , with  $\hbar$  being the reduced Planck's constant [2] and  $\omega$  being the optical frequency. Photons travel at the speed of light  $c$ , and carry a certain momentum  $\mathbf{p} = \hbar\mathbf{k}$ , with the wave vector  $\mathbf{k} = \omega/c$ . Any reflection of a photon causes a force on the reflecting object due to the conservation of momentum. Hence, a beam of photons with an average power  $P$  will result in an average force  $F = 2P/c$  in the case of retro-reflection. It is due to the large speed of light that this force is weak. An optical power of 1 W results in a radiation force of 6 nN. Yet, it was observed more than a century ago [3, 4]. Opto-mechanical interaction becomes relevant in case of high optical powers or small mechanical masses.

High optical powers became available with Einstein's later work about the stimulated emission of radiation [5]. It led to the development of the first optical laser by Theodore Maiman in 1960 [6], after it was proposed by Charles Townes and Arthur Shawlow in 1958 [7]. Maiman described the laser as '*A solution seeking for a problem*'. Due to rapid technological development, modern lasers are highly monochromatic, frequency stable and provide high optical powers. For these reasons, lasers make an excellent tool in high-precision experiments, such as the continuous measurement of test mass position. The light reflected from the test mass exhibits a position dependent phase shift, which can be accessed by interfering the reflected beam with a reference beam, for example in a Michelson interferometer.

# 1 Introduction

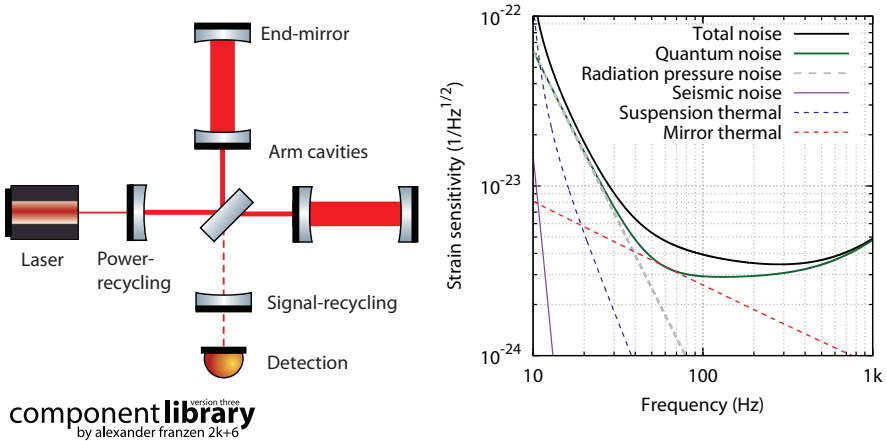


**Figure 1.1:** Left: schematic of a second generation GW detector. The laser power is enhanced by a power-recycling mirror and resonant arm cavities. The signals are detected after resonant amplification by a signal-recycling cavity. Right: anticipated strain sensitivity of the Advanced LIGO detector (Tuned signal recycling, no squeezing injection) simulated with *GWINC* [18]. Quantum noise dominates for high and low frequencies. Brownian thermal noise of the mirrors is dominant around 80 Hz.

## Gravitational wave detection

A prominent examples for interferometric measurement for differential arm length changes are large scale Michelson-type gravitational wave (GW) detectors [8–10], such as LIGO [11, 12], GEO600 [13], Virgo [14] and TAMA300 [15]. Their sensitivity reaches the astonishing level of  $10^{-19} \text{ m}/\sqrt{\text{Hz}}$  around a frequency of 1 kHz. Vacuum fluctuations of the phase and amplitude of the electro-magnetic field entail two quantum noise contributions in the detectors described above. Phase fluctuations manifest in form of quantum read out noise, the so-called shot noise. It can be reduced by increasing the optical input power. However, amplitude fluctuations are thereby enhanced and induce a stronger, fluctuating back-action force on the suspended (free-falling) mirror test masses. It was first recognised by Caves [16] that this back-action actually results in a standard-quantum limit (SQL) for the measurement precision [17]. If amplitude and phase fluctuations are assumed uncorrelated, there exists an optimum optical power for every observation frequency, minimising the uncorrelated sum of both, quantum read out and back-action noise. In this case, the experiment operates at the SQL for this particular frequency.

---

Currently, most detectors are being upgraded from first to second generation. For Advanced LIGO [19], this upgrade is expected to provide a significant reduction in classical noise. The anticipated strain sensitivity is depicted in Fig. 1.1. For high frequencies, the sensitivity will be limited by optical shot noise. Thermal noise is expected to dominate between 40 – 80 Hz, while radiation pressure noise is limiting the achievable sensitivity at frequencies from 40 – 10 Hz. For lower frequencies, seismic noise is limiting the sensitivity. There are several ideas and proposed concepts of how to beat the SQL. They include the injection of a squeezed vacuum state with a frequency dependent squeezing angle [17, 20–23], variational read out [24] or combinations of both methods [25].

However, GW detectors themselves are not best-suited for testing those concepts for the two following reasons. First, their purpose is a continuous operation with little scalability in their experimental parameters and second, they are designed to operate with a minimal amount of quantum noise. Therefore, smaller and less complex interferometric setups with a high susceptibility to (quantum) back-action noise are eligible. Typically, the approach in these experiment is to reduce the mirror mass drastically and enhance the laser power within optical resonators. This renders such experiments a subset of the quickly growing field of opto-mechanics.

## Opto-mechanics

The interaction of light and mechanical objects, e.g. the modification of the center-of-mass motion of a mechanical object by radiation forces is subject to the fundamental field of opto-mechanics. It was pioneered in 1967 by Braginsky [26, 27], who observed damping of an excited oscillator due to microwave radiation. A few years later, Dorsel [28] was able to observe opto-mechanical interaction in the optical regime. The field received increasing scientific attention with the emerging availability of high-quality, micro-mechanical devices with low optical losses, allowing for strong opto-mechanical coupling by incorporation into high-quality optical setups.

Today, a variety of oscillators is well-established in numerous opto-mechanical experiments, including monolithically suspended, kilogram-scale mirrors (as in GW detectors), gram-scale mirrors [29], micro-mirrors on cantilevers [30, 31] or nanobeams [32, 33], microtoroids [34, 35], thin membranes [36, 37] or opto-mechanical crystals [38].

## 1 Introduction

---

Their mass, mechanical quality factors and resonance frequencies span over several orders of magnitude. For recent reviews about opto-mechanical setups, the reader is kindly referred to [39–43].

The typical opto-mechanical setup consists of a single-ended Fabry-Perot cavity with one end-mirror (the oscillator) exhibiting one harmonic degree of freedom. In this case, the intra-cavity field and hence, the optical force acting on the oscillator depends on the cavity length, e.g. the oscillator position. This coupling gives rise to an optical spring [44], modifying the oscillator spring constant. Due to the finite cavity decay rate, its response to length variations is not instantaneous, causing optical (anti-) damping of the oscillator motion. This damping is associated with a reduction of the oscillator thermal motion, which has first been observed in the microwave [45] and later in the optical domain [46]. The 'good cavity' limit describes the situation in which the optical linewidth  $\gamma$  fulfils  $\gamma < 2\omega_m$ , where  $\omega_m$  is the mechanical resonance frequency of the oscillator. In this situation, the cavity operates in the *resolved side band* regime. If the optical power is high enough, it can be shown [40, 41, 47, 48] that the minimal achievable mean phonon occupation number of the oscillator in such a setup is given by

$$\bar{n}_{\min} = \left( \frac{\kappa_{\text{cav}}}{4\omega_m} \right)^2, \quad (1.1)$$

where  $\kappa_{\text{cav}}$  is the optical ring-down rate of the cavity and  $\omega_m$  is the mechanical resonance frequency of the oscillator. Thus, a high finesse (low decay rate) and a high mechanical resonance frequency will result in a small occupation number. Recently, several experiments achieved a mean occupation number  $\bar{n} < 1$ , and thus prepared the oscillator in the mechanical ground state [49, 50]. The mechanical ground state has also been achieved by pure cryogenic cooling of a 6 GHz oscillator, as demonstrated in [51].

The achievement of the mechanical ground state with micro-mechanical oscillators is an important milestone for quantum-mechanical experiments. It provides the basis for fundamental research in follow-up experiments, allowing to investigate decoherence effects in massive objects or to produce superposition of mechanical states. Other applications are expected in quantum information processing in photonic circuits [40] such as switching or storage.

However, macroscopic oscillators exhibit rather small resonance fre-



---

quencies. With reasonable cavity lengths and finesse values, achieving the resolved side band regime becomes more and more difficult with a lower mechanical resonance frequency of the oscillator in use.

This thesis presents the realisation of a signal-recycled Michelson-Sagnac interferometer. The topology can be regarded as an effective cavity that consists of the recycling mirror and a compound mirror established by the interferometer. The reflectivity of the interferometer depends on the microscopic position of a translucent oscillator within the interferometer. Unlike Fabry-Perot type opto-mechanical setups, the interaction in this topology can exhibit a purely dissipative character [52], e.g. the oscillator motion couples to the effective cavity linewidth rather than to the cavity resonance frequency. This holds the potential for strong optical cooling (close to ground-state) in the unresolved side band regime [53].

## Structure of the thesis

The thesis is structured as follows.

**Chapter 2** holds basic terms of (quantum) interferometric measurements such as the spectral density and the concept of a quantised electro-magnetic wave. This chapter briefly addresses two possible optical read out schemes, which were used throughout this thesis: A direct detection with a single photo detector and the balanced homodyne detection.

An analytical description of a damped harmonic oscillator is given in **Chapter 3**. The chapter also presents silicon nitride membranes, which were used as high quality micro-mechanical oscillators throughout this thesis.

**Chapter 4** focusses on the Michelson-Sagnac interferometer, which allows to incorporate the translucent oscillator as a common end-mirror in a two-path optical interferometer. The experimental setup is described, and relevant sources of noise are discussed. The chapter closes with a presentation of the experiment and the achieved interferometer displacement sensitivity.

The extension of this interferometer by an additional, high-reflective mirror in the interferometer output port is addressed in **Chapter 5**. This mirror gives rise to an effective cavity setup, which can be used to enhance the interferometer displacement sensitivity and to enable strong opto-mechanical interaction. The opto-mechanical interaction

## 1 Introduction

---

results in a anomalous, complex optical spring, which is described and observed in the experiment. In gravitational wave detectors, this mirror in the interferometer output port is used to resonantly enhance interferometric signals, and is therefore referred to as signal-recycling mirror [54–56].

**Chapter 6** presents the first application of cryogenic cooling to a full Michelson-Sagnac interferometer. A description of the experiment is given, including the cryogenic system and its principle of operation. An interferometer prototype for operation at cryogenic temperatures is presented. The chapter closes with the report of a successful operation of a Michelson-Sagnac interferometer at temperatures below 10 K.

The research presented in this thesis is summarised in **Chapter 7**.

## 2

## Chapter 2

## Basic concepts of quantum interferometry

### 2.1 Spectral density

A time dependent quantity  $x$  can either be analysed in the time domain  $x(t)$  or, alternatively in the frequency domain  $x(\omega)$ . The correlation between both descriptions is the Fourier transformation of  $x(t)$

$$x(\omega) = \int_{-\infty}^{\infty} x(t)e^{-i\omega t} dt \quad . \quad (2.1)$$

The Fourier transform of a function only exists for square-integrable functions. For example,  $f(t) = \sin(\omega t)$  is not square-integrable. For practical reasons, one therefore defines the Fourier transform for finite measurement intervals  $T$ , called  $x_T(\omega)$

$$x_T(\omega) = \int_{-T/2}^{T/2} x(t)e^{-i\omega t} dt \quad , \quad (2.2)$$

such that

$$\lim_{T \rightarrow \infty} x_T(\omega) = x(\omega) \quad (2.3)$$

is fulfilled. In an optical experiment,  $x(t)$  might be the output voltage of a photo detector. In case of measuring a random process,  $x(t)$  cannot even be written as an analytic function of  $t$ . Instead, only probabilities  $p_i$  for a certain measurement outcome  $x_i$  can be given when measuring on an ensemble of possible states  $i$ . It is then convenient to consider the expectation value of a large number of measurements

## 2 Basic concepts of quantum interferometry

---

$$\langle x(t) \rangle = \sum p_i x_i \quad , \quad (2.4)$$

The so-called *correlation-function*

$$S_{xy}(t_1, t_2) = \langle x(t_1)y(t_2) \rangle \quad (2.5)$$

is a measure of how the measurement of  $y$  at time  $t_2$  relates to the measurement  $x$  at time  $t_1$ . The correlation-function of a quantity with itself at a different time  $t + \tau$  is referred to as the *auto-correlation function* and is written as

$$S_x(t, \tau) = \langle x(t)x(t + \tau) \rangle \quad . \quad (2.6)$$

It expresses how much the measurement outcome  $x$  at time  $t$  is linked to measuring  $x$  again at some point  $\tau$  later in time. It thus depicts the self-similarity of the quantity. The Fourier transform of the auto-correlation function

$$|G_x(\omega)|^2 = \int_{-\infty}^{\infty} \langle x(t)x(t + \tau) \rangle e^{-i\omega t} dt \quad , \quad (2.7)$$

is referred to as the spectral density. Equation 2.7 is symmetric in  $\omega$ ,  $|G_x(\omega)|^2 = |G_x(-\omega)|^2$ , such that the consideration can be restricted to positive frequencies (one-sided spectral density). In this case, an additional factor of 2 is required to maintain equality. Back-transformation with  $S_x(t, 0) = \Delta^2 x$  yields

$$\langle x^2 \rangle = \int_{-\infty}^{\infty} \frac{d\omega}{2\pi} |G_x(\omega)|^2 = \int_0^{\infty} \frac{d\omega}{2\pi} 2 |G_x(\omega)|^2 \quad . \quad (2.8)$$

It can be shown that in case of stationary random processes [57], the following statement holds,

$$|G_x(\omega)|^2 = \lim_{T \rightarrow \infty} \frac{|x_T(\omega)|^2}{T} \quad , \quad (2.9)$$

which is known as the *Wiener-Khintchine theorem* [58, 59].

### Optical shot noise

The typical example for noise in optical experiments is photon shot noise. If a photodetector is measuring the number of arriving photons (which are assumed to have a mean flux  $\bar{I}$ ), the arrival of each individual photon is completely random and unrelated to the arrival

of another photon. In the time domain, this can be expressed by assuming [57]

$$I(t) = \sum_k \delta(t - t_k), \quad \bar{I} = \bar{n} \quad . \quad (2.10)$$

The Fourier transform of its auto-correlation function yields the one-sided spectral density [60] (compare Sec. 2.2)

$$|G_I(\omega)|^2 = 2\bar{n} \quad . \quad (2.11)$$

The optical shot noise is frequency independent and the power spectral density is proportional to the number of photons. To get to the spectral density of power fluctuations, the power charge  $\hbar\omega$  of each photon has to be considered in Eq. (2.11), giving

$$|G_P(\omega)|^2 = 2\hbar\omega P = 2\hbar \frac{2\pi c}{\lambda} P \quad . \quad (2.12)$$

Often, it is more convenient to consider the linear spectral density, given by

$$\sqrt{|G_P|^2} = G_P = \sqrt{\frac{4\pi\hbar c}{\lambda}} P \quad . \quad (2.13)$$

## 2.2 Quantisation of light fields

An electro-magnetic field is classically described as a solution of Maxwell's Equations [61]. The one dimensional solutions in absence of charge or currents are plane, sinusoidal waves [62]

$$E_x(z, t) = \left( \frac{2\omega^2}{V\epsilon_0} \right)^{1/2} q(t) \sin(kz) \quad , \quad (2.14)$$

$$B_y(z, t) = \left( \frac{\mu_0\epsilon_0}{k} \right) \left( \frac{2\omega^2}{V\epsilon_0} \right)^{1/2} \dot{q}(t) \cos(kz) \quad . \quad (2.15)$$

Here,  $V$  is the effective quantisation volume,  $k = \omega/c$  is the wave vector satisfying given boundary conditions.  $\epsilon_0$  is the vacuum permittivity and  $\mu_0$  the vacuum permeability, which are connected to the speed of light  $c = 1/\sqrt{\mu_0\epsilon_0}$ .  $\dot{q}(t) = p(t)$  is the canonical momentum and  $q(t)$  the position. The quantisation is performed by considering the classical Hamilton function and replacing the classical quantities  $q(t)$  and  $p(t)$  by the canonical position and momentum operators  $\hat{P}$

## 2 Basic concepts of quantum interferometry

---

and  $Q$ . This yields the Hamilton operator  $\mathcal{H}$  for a single optical mode of frequency  $\omega$

$$\mathcal{H}(P, Q) = \frac{1}{2}(P^2 + \omega^2 Q^2) \quad . \quad (2.16)$$

The position and momentum operator fulfil the commutation relation

$$[Q, P] = QP - PQ = i\hbar \quad . \quad (2.17)$$

Using the so-called *raising* and *lowering operators*  $A$  and  $A^\dagger$ , and setting  $\varepsilon_0 = (\hbar\omega/\epsilon_0 V)^{1/2}$ , the electric field (now as an operator) writes [62]

$$E_x(z, t) = \varepsilon_0(A + A^\dagger) \sin(kz) \quad . \quad (2.18)$$

The raising and lowering operators arise as a combination of position and momentum operators

$$A = \frac{1}{\sqrt{2\hbar\omega}}(\omega Q + iP) \quad . \quad (2.19)$$

$$A^\dagger = \frac{1}{\sqrt{2\hbar\omega}}(\omega Q - iP) \quad . \quad (2.20)$$

These operators also lead to an elegant expression for the Hamilton operator  $\mathcal{H}$

$$\mathcal{H} = \hbar\omega \left( A^\dagger A + \frac{1}{2} \right) \quad . \quad (2.21)$$

The eigenstates of the Hamilton operators are thus eigenstates of the so-called *number operator*  $N = A^\dagger A$ . They are referred to as *Fock states* and labeled  $|n\rangle$ . A Fock state contains an exactly defined number of photons  $n$  of energy  $\hbar\omega$ .

$$N |n\rangle = n |n\rangle \quad . \quad (2.22)$$

The effect of  $A^\dagger$  and  $A$  on a Fock state are given by

$$A |n\rangle = \sqrt{n} |n-1\rangle, \quad A^\dagger |n\rangle = \sqrt{n+1} |n+1\rangle \quad . \quad (2.23)$$

Raising and lowering operator do not commute, which is expressed in their commutator

$$[A, A^\dagger] := AA^\dagger - A^\dagger A = 1 \quad . \quad (2.24)$$

A prominent example of a Fock state is the vacuum state. It contains no photons and therefore is just written as  $|0\rangle$ . Any Fock state  $|n\rangle$  can be generated by applying the raising operator to the ground state  $n$  times

$$|n\rangle = \frac{1}{\sqrt{n!}} \left( A^\dagger \right)^n |0\rangle . \quad (2.25)$$

Fock states are a complete basis every optical state can be developed in. It is then expressed as a weighted sum of Fock states. This is especially true for the eigenstates  $|\varphi\rangle$  of the lowering operator  $A$  with  $A|\varphi\rangle = \varphi|\varphi\rangle$ . These states are referred to as *coherent* states. They are a good approximation for a sinusoidal electro-magnetic wave [63] and thus a valid representation of a laser output field. The eigenvalues  $\varphi$  are complex in general, and  $\varphi^*$  denotes the complex conjugate of  $\varphi$ . Any coherent state can be written as

$$|\varphi\rangle = \sum_{n=0}^{\infty} C_n |n\rangle = D(\varphi) |0\rangle , \quad (2.26)$$

with  $D(\varphi) = \exp(\varphi A^\dagger - \varphi^* A)$ , called the *displacement* operator [62], such that the coherent state is given by

$$|\varphi\rangle = \exp\left(-\frac{1}{2}|\varphi|^2\right) \sum_{n=0}^{\infty} \frac{\varphi^n}{\sqrt{n!}} |n\rangle . \quad (2.27)$$

A coherent state  $|\varphi\rangle$  thus exhibits an expectation value  $\bar{n}$  given by

$$\bar{n} = \langle N \rangle = \langle \varphi | N | \varphi \rangle = |\varphi|^2 . \quad (2.28)$$

The mean number of detected photons is thus given by the coherent excitation  $|\varphi|^2$ . The variance is defined and given by

$$\Delta^2 N := \langle N^2 \rangle - \langle N \rangle^2 = \bar{n} . \quad (2.29)$$

In contrast to a Fock state, the number of photons in a coherent state is therefore not exactly defined. The probability of detecting  $n$  photons in a coherent state  $|\varphi\rangle$  is then given by a Poisson distribution

$$P_n(\varphi) = |\langle n | \varphi \rangle|^2 = \frac{\bar{n}^n}{n!} e^{-\bar{n}} , \quad (2.30)$$

which, for large  $\bar{n}$  is a Gaussian distribution

## 2 Basic concepts of quantum interferometry

---

$$P_n(\varphi) \approx \frac{1}{\sqrt{2\pi\bar{n}}} \exp\left(-\frac{(n - \bar{n})^2}{2\bar{n}}\right) . \quad (2.31)$$

Two other operators can be defined using the raising and lowering operators. These are the so-called *amplitude quadrature operator*  $X_1$  and the *phase quadrature operator*  $X_2$ , which are defined as

$$X_1 = (A + A^\dagger) , \quad X_2 = i(A^\dagger - A) . \quad (2.32)$$

These operators obey the commutator relation  $[X_1, X_2] = 2i$ . Their expectation values for a coherent state  $|\varphi\rangle$  are given by

$$\langle X_1 \rangle = (\varphi + \varphi^*) = 2\Re[\varphi] , \quad \langle X_2 \rangle = 2\Im[\varphi] . \quad (2.33)$$

For any coherent state  $|\varphi\rangle$ , the variances are

$$\Delta^2 X_1 = \Delta^2 X_2 = 1 . \quad (2.34)$$

Coherent states exhibit a minimal uncertainty product [64]. Since the vacuum state is a coherent state, a measurement on the vacuum state will exhibit noise, as its variance is non-vanishing. Note that the amplitude and phase quadrature operators also allow to define arbitrary readout quadratures  $X_\theta$ , [65]

$$X_\theta = X_1 \cos(\theta) + X_2 \sin(\theta) = A^\dagger e^{i\theta} + A e^{-i\theta} . \quad (2.35)$$

### Operator linearisation

In the case of large coherent amplitudes  $\varphi$  that outweigh the fluctuations, the raising and lowering operators write [66, 67]

$$A = \varphi + \delta A , \quad A^\dagger = \varphi^* + \delta A^\dagger . \quad (2.36)$$

The expectation values for the (time-dependent) fluctuating terms are  $\langle \delta A \rangle = \langle \delta A^\dagger \rangle = 0$ . This allows to rewrite the number operator. Assuming  $\varphi$  is real, it is given by

$$\begin{aligned} N &= A^\dagger A = (\varphi^* + \delta A^\dagger)(\varphi + \delta A) \\ &= |\varphi|^2 + \varphi^* \delta A + \varphi \delta A^\dagger + \delta A^\dagger \delta A \\ &\approx |\varphi|^2 + \varphi \delta X_1 , \end{aligned} \quad (2.37)$$

where in the last step the higher order terms  $\delta A^\dagger \delta A$  were neglected [65], and the operator is thus linearised.



## 2.3 Performing measurements on light fields

Measurements on light fields are typically performed with reverse biased semi-conductor photo diodes. Within the diode, electrons can be excited within the depleted zone of a p-n or PIN junction by absorption of photons. For a sufficient photon energy, free electrons are created and result in an electric current. The intensity of this current is proportional to the number of arriving photons.

Within this thesis, two methods were used to perform measurements on an interferometer output optical mode, and shall be presented here briefly.

### 2.3.1 Direct detection

The simplest measurement on a laser beam is a direct detection with a single photodiode. Equation (2.37) implies that such a measurement can only provide access to the fluctuations in the amplitude quadrature, as the photocurrent of a single photo diode is proportional to the number of arriving photons. For a coherent laser beam, the detected photo current can be written as

$$i_{\text{PD}} \propto N = |\varphi|^2 + \varphi \delta X_1 \quad , \quad (2.38)$$

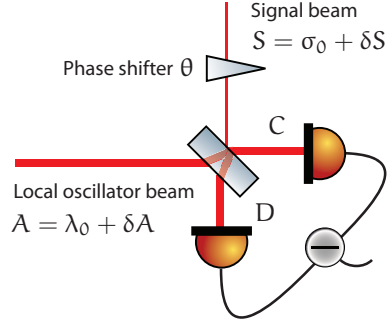
if higher order terms are neglected, e.g. when the Number operator is linearised. The detected photo current consists of a constant term and time-dependent, fluctuating term  $\delta X_1$ , which is scaled by the coherent excitation  $\varphi$  (which is assumed real). Each term can be accessed by electronic high- or low pass filtering. This method is also referred to as *self-homodyne* detection.

### 2.3.2 Balanced homodyne detection

Balanced homodyne detection [68] allows to detect arbitrary quadratures of the optical field. In this scheme, a signal beam is interfered with another light beam of the same optical wavelength (local oscillator) on a balanced beam splitter. The relative phase  $\theta$  between both light fields can typically be adjusted by a phase shifting device, such as an electro-optic modulator or a piezo actuated mirror. Here, it will be referred to as  $\theta$ . Both ports of the beam splitter are read out with a photo detector. The individual photo currents yield

## 2 Basic concepts of quantum interferometry

**Figure 2.1:** Balanced homodyne detection scheme. The signal beam is overlapped on a balanced beam splitter with a stronger second light field of the same wavelength, the so-called local oscillator. The relative phase  $\theta$  is adjusted by some phase shifting device.



$$C^\dagger C = \frac{1}{2}(A^\dagger + S)(A + S^\dagger) \quad , \quad (2.39)$$

$$D^\dagger D = \frac{1}{2}(-A^\dagger + S^\dagger)(-A + S) \quad . \quad (2.40)$$

The sum and differences of the individual photo currents are given by  $i_\pm \propto C^\dagger C \pm D^\dagger D$ . They can be expressed according to [65] as

$$i_+ \propto \lambda_0^2 + \sigma_0^2 + \lambda_0 \delta X_{1,A} + \sigma_0 \delta X_{1,S} \quad , \quad (2.41)$$

$$i_- \propto 2\lambda_0 \sigma_0 \cos(\theta) + \lambda_0 \delta X_{\theta,S} + \sigma_0 \delta X_{-\theta,A} \quad . \quad (2.42)$$

Under the assumption that  $\sigma_0 = 0$ , which is fulfilled for the case of a vacuum state, the above expressions simplify to

$$i_+ \propto \lambda_0^2 + \lambda_0 \delta X_{1,A} \quad , \quad (2.43)$$

$$i_- \propto 2\lambda_0 \sigma_0 \cos(\theta) + \lambda_0 \delta X_{\theta,S} \quad . \quad (2.44)$$

When  $\sigma_0 \neq 0$ , e.g. when the signal beam is 'just' weak instead of vacuum, then this approximation does not necessarily hold: The coherent amplitude  $\sigma_0$  of the signal beam enhances the fluctuations of the local oscillator. Especially for low frequencies, these (classical) fluctuations may be huge. Thus,  $\sigma_0 \delta X_{-\theta,S} \ll \lambda_0 \delta X_{\theta,S}$  has to be fulfilled.

## 3

## Chapter 3

## The mechanical oscillator

This chapter provides a brief mathematical description of a harmonic oscillator, introducing the oscillator mechanical transfer function, the quality factor, and the thermal noise of a damped harmonic oscillator. Next, the silicon nitride membrane is described, which is the oscillator investigated throughout this thesis. The chapter ends with a short description of the membrane's optical and mechanical properties.

### 3.1 The oscillator transfer function

Starting with Newton's law for a system with a position dependent restoring force  $F_{\text{spring}} = -kx(t)$  of spring constant  $k$  and some arbitrary damping force  $F_{\text{arb.}}(x(t), \dot{x}(t))$ , the equation of motion  $x(t)$  can be derived by solving the differential equation

$$\left[ m \frac{d^2}{dt^2} + F_{\text{arb.}}(x(t), \dot{x}(t)) + k \right] x(t) = F_{\text{ext}}(t) \quad . \quad (3.1)$$

The approach is similar to the one given in [57]. It is convenient to solve the latter equation by Fourier transformation, which can be defined as follows:

$$x(\omega) = \int_{-\infty}^{\infty} dt e^{-i\omega t} x(t), \quad x(t) = \frac{1}{2\pi} \int_{-\infty}^{\infty} d\omega e^{i\omega t} x(\omega) \quad . \quad (3.2)$$

Multiplication of both sides of Eq. (3.1) with  $e^{-i\omega t}$  and integration over all times  $t$  yields

### 3 The mechanical oscillator

---

$$\begin{aligned} \int_{-\infty}^{\infty} dt e^{-i\omega t} \left[ m \frac{d^2}{dt^2} + F_{\text{arb.}}(x(t), \dot{x}(t)) + m\omega_0^2 \right] x(t) \\ = \int_{-\infty}^{\infty} dt e^{-i\omega t} F_{\text{ext}}(t) \quad . \end{aligned} \quad (3.3)$$

Here, the resonance frequency  $\omega_0^2 = k/m$  is introduced. For physical functions  $x(t = \pm\infty) = 0$ , the Fourier transform of the time derivative  $\dot{x}(\omega)$  can be written as

$$\dot{x}(\omega) = \int_{-\infty}^{\infty} dt e^{-i\omega t} \frac{d}{dt} x(t) \quad (3.4)$$

$$= \underbrace{\left[ e^{-i\omega t} x(t) \right]_{-\infty}^{+\infty}}_{=0} - (-i\omega) \underbrace{\int_{-\infty}^{\infty} dt e^{-i\omega t} x(t)}_{x(\omega)} \quad . \quad (3.5)$$

With  $\left(\frac{d}{dt}\right)^n x(\omega) = (i\omega)^n x(\omega)$ , it directly follows from Eq. (3.3) that

$$\left[ -m\omega^2 + i \frac{F_{\text{arb.}}(x(\omega), \dot{x}(\omega))}{ix(\omega)} + m\omega_0^2 \right] x(\omega) = F_{\text{ext}}(\omega) \quad . \quad (3.6)$$

With the definition

$$k_{\text{arb.}}(x(\omega), \dot{x}(\omega)) = \frac{F_{\text{arb.}}(x(\omega), \dot{x}(\omega))}{ix(\omega)} \quad , \quad (3.7)$$

the algebraic Eq. (3.6) can be rearranged, such that if  $F_{\text{ext}}(\omega)$  is known,  $x(\omega)$  can be retrieved easily

$$x(\omega) = \frac{1}{m(\omega_0^2 - \omega^2) + ik_{\text{arb.}}(x(\omega), \dot{x}(\omega))} F_{\text{ext}}(\omega) \quad (3.8)$$

$$= \left[ \frac{1}{m\omega_0^2} \frac{1 - \frac{\omega^2}{\omega_0^2} - i \frac{k_{\text{arb.}}}{m\omega_0^2}}{\left(1 - \frac{\omega^2}{\omega_0^2}\right)^2 + \left(\frac{k_{\text{arb.}}}{m\omega_0^2}\right)^2} \right] F_{\text{ext}}(\omega) \quad (3.9)$$

$$= G(\omega) F_{\text{ext}}(\omega) \quad , \quad (3.10)$$

where  $G(\omega)$  represents the complex oscillator transfer function. The modulus of this function gives the real displacement, whereas the phase difference  $\phi(\omega)$  between excitation and reaction is given by the imaginary part

$$\phi(\omega) = \arg(G(\omega)) \quad . \quad (3.11)$$

### Damping mechanisms

An ideal harmonic oscillator can be described by

$$F_{\text{arb.}}(\mathbf{x}(t), \dot{\mathbf{x}}(t)) = 0 \quad . \quad (3.12)$$

In this case,  $k_{\text{arb.}} = 0$ , and the oscillator transfer function is singular at  $\omega_0$ .

### Viscous damping

Typically, a velocity dependent damping is assumed. It basically arises from the idea that the oscillator motion is damped by residual gas [69] in which the oscillator performs motion. In this case, the damping force can be written as

$$F_{\text{arb.}}(t) = -\gamma \dot{\mathbf{x}}(t) \quad . \quad (3.13)$$

Inserting Eq. (3.13) into Eq. (3.7) yields  $k_{\text{arb.}}(\omega) = \gamma\omega$ .

### Structural damping

Another damping mechanism is subject to internal loss of the oscillator itself. It can be modeled by assuming a repulsive internal force

$$F_{\text{int.}} = -k(1 + i\phi(\omega))\mathbf{x}(\omega) \quad . \quad (3.14)$$

Comparison with Eq. (3.6) yields  $k_{\text{arb.}}(\omega) = k\phi(\omega)$ . The form of  $\phi(\omega)$  is commonly assumed to be constant over a large band of frequencies, although this approximation can not be fulfilled for arbitrarily low frequencies. For linear systems, the damping forces  $F_{\text{arb.}}$ , acting on the oscillator simply add up

$$F_{\text{arb.}} = \sum_i F_{\text{arb.,}i} \quad . \quad (3.15)$$

## 3.2 Mechanical quality factor

An important quantity for a harmonic oscillator is the mechanical quality factor  $Q$ . It is a measure of energy dissipation

$$E(t) = E_0 e^{-\frac{\omega_0 t}{Q}} . \quad (3.16)$$

In this definition it determines the time it needs for the oscillator's energy to drop to a fraction of  $1/e$  of any initial value  $E_0$ , which is given by  $t = Q/\omega_0$ . For viscous and structural damping the quality factors are determined by

$$Q_{\text{vis.}} = \frac{m\omega_0^2}{\gamma}, \quad Q_{\text{st.}} = \frac{1}{\phi} . \quad (3.17)$$

In the case of viscous or structural damping, the oscillator transfer function can be written as

$$G_{\text{vis.}}(\omega) = \frac{1}{m\omega_0^2} \frac{1}{\left(1 - \frac{\omega^2}{\omega_0^2}\right) + i\left(\frac{1}{Q_{\text{vis.}}} \frac{\omega}{\omega_0}\right)} , \quad (3.18)$$

$$G_{\text{struc.}}(\omega) = \frac{1}{m\omega_0^2} \frac{1}{\left(1 - \frac{\omega^2}{\omega_0^2}\right) + i\left(\frac{1}{Q_{\text{struc.}}} \frac{1}{m\omega_0^2}\right)} . \quad (3.19)$$

It is remarkable that in case  $Q \gg 1$  (which is always fulfilled in the experiment),  $G_{\text{vis.}}(\omega) \approx G_{\text{struc.}}(\omega)$  and therefore will only be referred to as  $G(\omega)$  in the following. For multiple damping mechanisms acting on the system, the mechanical quality factors add up inversely:

$$\frac{1}{Q_{\text{total}}} = \sum_i \frac{1}{Q_i} . \quad (3.20)$$

Another possibility to define the mechanical quality factor is [69]

$$Q = \frac{G(\omega_0)}{G(0)} = \frac{\omega_0}{\Delta\omega} , \quad (3.21)$$

where  $\Delta\omega$  is the full width at half maximum (FWHM) of the oscillator transfer function. This also gives an intuitive meaning to the quality factor as can be seen in Fig. 3.1. Here, the quality factor is 20, which corresponds to the ratio of  $|G(\omega \rightarrow 0)|$  and the transfer function peak value  $|G(\omega_0)|$ .

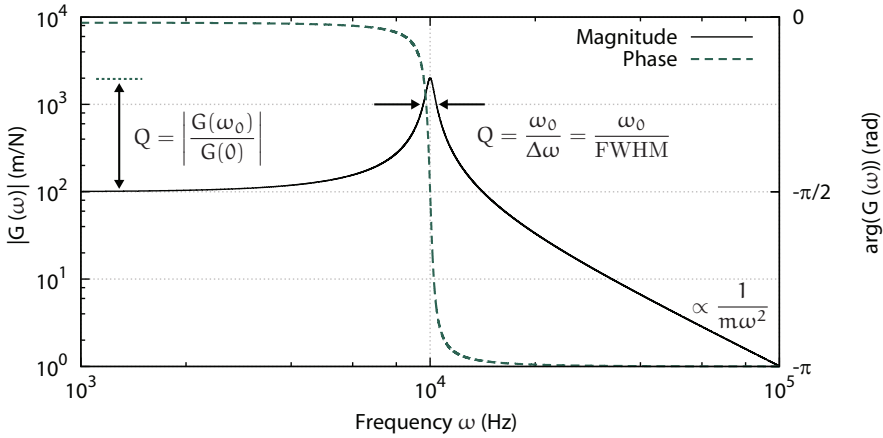


**Figure 3.1:** Oscillator transfer function for a mass of  $m = 100$  ng, resonance frequency  $\omega_0 = 10$  kHz and a spring constant  $k_{\text{arb.}} = 5.0 \cdot 10^{-4} = \text{const.}$  The resulting quality factor  $Q$  is 20. For high frequencies,  $|G(\omega)| \propto 1/(m\omega^2)$ , which corresponds to the transfer function of a free mass.

### 3.3 Thermal noise

Due to the finite temperature of the oscillator, the Brownian motion of atoms imposes a sensitivity limit for the displacement measurement. The motion caused by thermal excitation can be calculated with the Fluctuation-Dissipation theorem [70].

#### Fluctuation-Dissipation theorem

The Fluctuation-Dissipation Theorem (FDT) was formulated by Nyquist in 1928 [71] and was proven by Callen [72, 73]. It states that the spectral densities of a dissipative system in thermal equilibrium with its environment are given by [74]

$$|G_{\text{thermal}}^x(\omega)|^2 = -\frac{4k_B T}{\omega} \text{Im}[G(\omega)] \quad . \quad (3.22)$$

Here,  $k_B$  is the Boltzmann constant, and  $T$  is the temperature. It can be shown that  $\text{Im}[G(\omega)] = -k_{\text{arb.}}|G(\omega)|^2$ . In case of viscous damping  $k_{\text{arb.}} = \gamma\omega$ . Inserting this result into Eq. (3.22) and comparison with Eq. (3.10) yields the force spectral density

$$|G_{\text{thermal}}^F(\omega)|^2 = 4k_B T \gamma \quad . \quad (3.23)$$

### 3 The mechanical oscillator

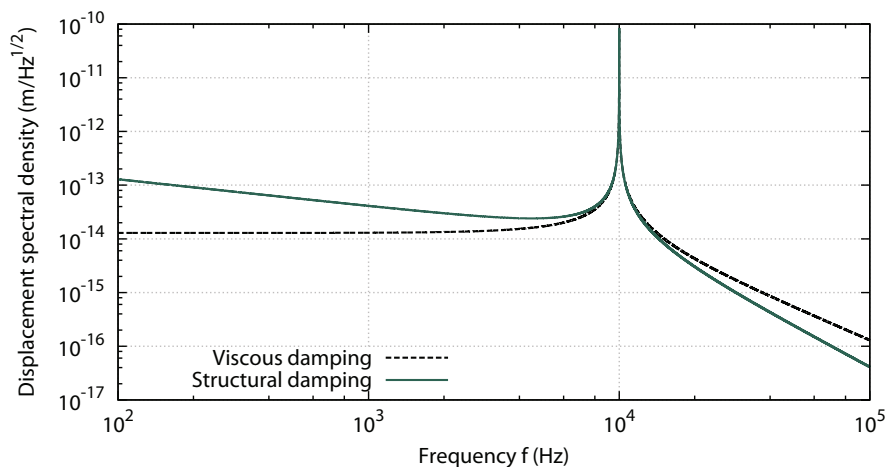


**Figure 3.2:** Comparison of viscous and structural damping mechanism and the corresponding displacement spectral density in  $\text{m}/\sqrt{\text{Hz}}$  for  $m = 100 \text{ ng}$ ,  $\omega_0/(2\pi) = 10 \text{ kHz}$ ,  $T = 300 \text{ K}$  and  $Q = 10^6$ .

The FDT theorem allows to calculate the thermal noise displacement spectral density, which, in case of viscous or structural damping is given by

$$|G_{\text{vis.}}^x(\omega)|^2 = 4mk_B T \frac{\omega_0}{Q_{\text{vis.}}} |G(\omega)|^2, \quad (3.24)$$

$$|G_{\text{struc.}}^x(\omega)|^2 = 4mk_B T \frac{\omega_0^2}{Q_{\text{str.}} \omega} |G(\omega)|^2. \quad (3.25)$$

The displacement spectral density in the case of structural and viscous damping is depicted in Fig. 3.2. Surprisingly, the choice of a constant (frequency independent) loss angle  $\phi$  results in a more complex shaped thermal noise spectral density (additionally scaled with a factor  $\omega^{-1/2}$ ), as can be seen from Eq. (3.25).



### 3.4 Silicon Nitride membrane

Throughout this thesis, a commercially available silicon nitride membrane, manufactured by *Norcada* [75], was used as a mechanical oscillator. Repulsive forces perpendicular to the membrane plane render it a harmonic oscillator at the same time.

The mechanical eigenmodes of such a membrane exhibit an extraordinarily high mechanical quality factor of about  $10^6$  at room temperature which can even increase to  $10^7$  at cryogenic temperatures of 300 mK [77]. The resonance frequencies  $f_{\text{res}}$  depend on the membrane's chemical composition (the ratio between silicon and nitrogen  $\text{Si}_x\text{N}_y$ ) [78, 79], thickness and size, but are found usually in a frequency range from 10 kHz – 1 MHz. Silicon nitride membranes have been used in linear, Fabry-Perot interferometers before [36, 37, 80], their first implementation in a Sagnac interferometer was reported in [76, 81].

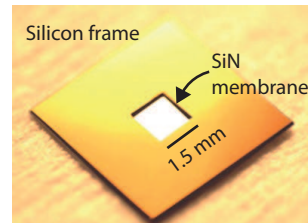


**Figure 3.3:** Photograph of a  $1.5 \times 1.5 \text{ mm}^2$  *Norcada* membrane [76]. The frame size is  $1 \text{ cm}^2$ .

#### 3.4.1 Optical properties

Typically, the thickness of the membrane is several tens of nm up to  $1 \mu\text{m}$ . Their power reflectivity for a given laser wavelength  $\lambda$  can be calculated considering the index of refraction of silicon nitride (at the particular wavelength) and the interference in the sub-wavelength thin membrane.

The relevant case is the amplitude reflectivity under normal incidence. Using Fresnel formulas, the amplitude reflectivity for the transition from medium one (vacuum  $n = 1$ ) to a medium of higher index of refraction results in an amplitude reflection and transmission coefficient

$$r = \frac{n_{\text{SiN}} - 1}{n_{\text{SiN}} + 1} \quad \text{and} \quad t = \frac{2n_{\text{SiN}}}{n_{\text{SiN}} + 1} \quad (3.26)$$

at each surface. The power reflectivity of the membrane is depicted in Fig. 3.4 for typical wavelengths used at the AEI. The corresponding formula is derived in Chapter 5 as Eq. (5.5). Here, the index of refraction of silicon nitride is assumed to be  $n_{\text{SiN}} = 2.22$ , as was determined in [81] and  $n_{\text{SiN}} = 2.2$ , as reported in [77]. The result is depicted in Fig. 3.4 for typical wavelengths used at the AEI. The maximum power

### 3 The mechanical oscillator

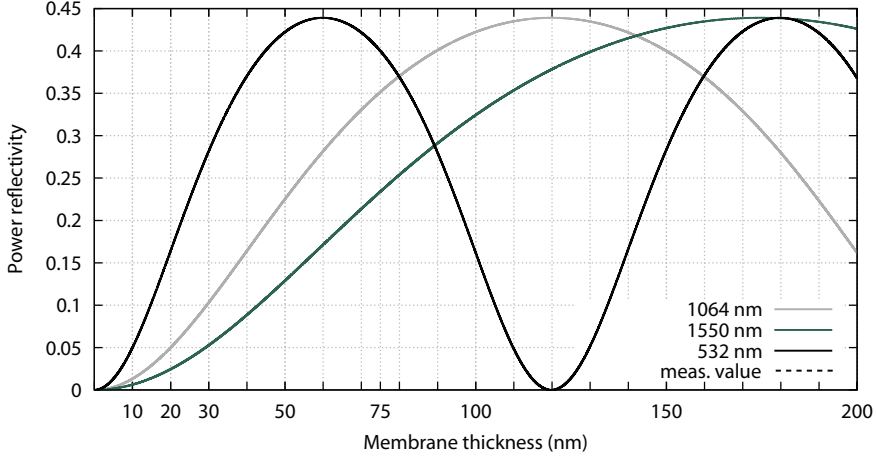


**Figure 3.4:** SiN membrane power reflectivity for different optical wavelengths. The power reflectivity is a periodic function of membrane thickness and can be determined according to Eq. (5.5). The membrane thickness can be determined by measuring its power reflectivity under normal incidence at a particular laser wavelength for a given index of refraction.

reflectivity is around 43 %, and is reached for a membrane thickness  $d$  that corresponds to an anti-resonance of the light field within the membrane. In turn, for a given thickness, the power reflectivity  $r_m^2$  depends on the laser wavelength.

#### 3.4.2 Modes of motion and effective mass

A SiN membrane is able to perform different deflection movements. Being fixed to the massive rectangular silicon frame which we assume to be in the  $xy$ - plane, possible eigenmotions  $u(x, y, t)$  can be calculated [76, 82] by solving the Helmholtz equation

$$\partial_t^2 u(x, y, t) = \frac{T}{\mu} (\partial_x^2 + \partial_y^2) u(x, y, t) \quad . \quad (3.27)$$

Here,  $T$  is the intrinsic tension of the membrane,  $L_x$  and  $L_y$  are the membrane geometrical dimensions and  $\mu$  is the mass per area, which is found by the density  $\rho$  and the membrane thickness  $d$ . The boundary condition  $u(x, 0, t) = u(0, y, t) = 0 \forall t$ , results in a set of solutions

$$u_{m,n}(x, y, t) = \sin\left(\frac{m\pi x}{L_x}\right) \sin\left(\frac{n\pi y}{L_y}\right) \cos(\omega_{m,n} t) \quad . \quad (3.28)$$

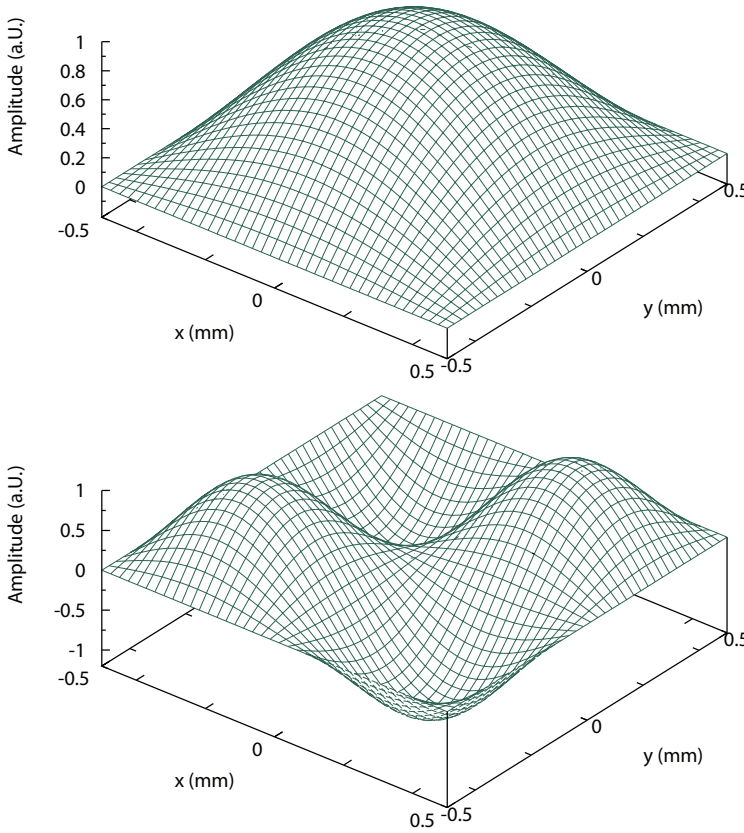


**Figure 3.5:** Graphical illustration of the membrane fundamental oscillation mode  $m = n = 1$  (upper picture) and  $m = n = 2$  (lower picture). The membrane size in this case is  $1 \times 1 \text{ mm}^2$ . In case of the (2,2) mechanical mode the centre of the membrane is not moving.

Thus, only a certain region of the membrane actually moves. The harmonic oscillator equation of motion

$$0 = \partial_t^2 z + \omega_0^2 z \quad , \quad (3.29)$$

where  $\omega_0^2 = k/(m_{\text{eff}})$ , is fulfilled for the correct effective mass  $m_{\text{eff}}$ . For the fundamental oscillation mode ( $m = n = 1$ )  $m_{\text{eff}}$  can be derived to be  $m_{\text{eff}} = m/4$  with  $m$  being the membrane physical mass [76, 81]. For the experimental membrane parameters,  $m_{\text{eff}}$  is about 100 ng for the fundamental oscillation mode.

### 3 The mechanical oscillator

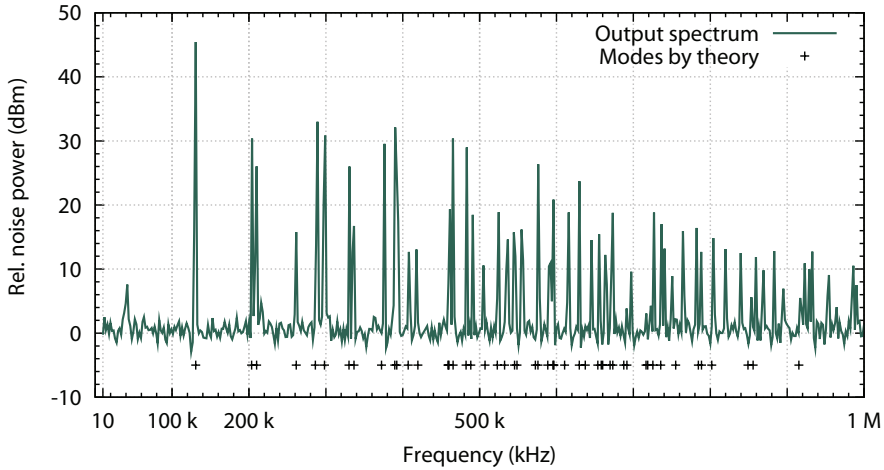


**Figure 3.6:** A typical interferometer output power spectrum. Various sharp resonances correspond to the thermally excited membrane oscillation modes. The fundamental oscillation mode is found at  $f_{11} = 133$  kHz. Other resonances agree with the calculated frequencies, calculated by Eq. (3.30) and plotted as black crosses.

#### 3.4.3 Resonance frequencies

Figure 3.6 shows a typical output power spectrum in transmission of the interferometer. It contains several sharp peaks at the membrane resonance frequencies. For each membrane mode  $m, n$ , the resonance frequency are given by [81]

$$\omega_{m,n} = \pi \sqrt{\frac{T}{\mu} \left( \frac{m^2}{L_x^2} + \frac{n^2}{L_y^2} \right)} . \quad (3.30)$$

The calculated frequencies for modes  $m, n \leq 5$  for the membrane under investigation are depicted as black crosses in Fig. 3.6, and agree nicely with the experimental results.

The height of the peaks originates from their effective mass, which is lowest for the fundamental mode, and the readout position on the membrane. Fig. 3.5 depicts the fundamental mode (1,1) for a square membrane. In case of the (2,2) mode, no signal would be expected for case where the beam is perfectly centred on the membrane. However, the corresponding peak is non-vanishing in the spectrum, which is due to a beam offset from the membrane centre.

### 3.4.4 Membrane mechanical quality factor

The mechanical quality factor of the fundamental mode of the membrane has been determined by ring-down measurements in a high-vacuum environment. Therefore, the membrane was excited by a piezo ceramic transducer with its resonance frequency. The decay of the oscillation amplitude is then observed after a sudden stop of the excitation.

The mechanical quality factor is defined in Eq. (3.17). Assuming viscous damping  $F_{\text{arb}} = \gamma \dot{x}(t)$  and no exciting force  $F_{\text{ext}} = 0$ , Eq. (3.1) can be rewritten

$$\left[ \frac{d^2}{dt^2} + \frac{\gamma}{m} \frac{d}{dt} + \omega_0^2 \right] x(t) = 0 \quad (3.31)$$

$$\Leftrightarrow \left[ \frac{d^2}{dt^2} + \frac{\omega_0^2}{Q_{\text{vis}}} \frac{d}{dt} + \omega_0^2 \right] x(t) = 0 \quad . \quad (3.32)$$

The solution for low energy dissipation (high mechanical quality factor  $Q_{\text{vis}}$ ) is then given by

$$x(t) = x_0 e^{-\omega_0^2 t / 2Q_{\text{vis}}} \cos(\omega t), \quad \omega^2 = \omega_0^2 \left( 1 - \frac{\omega_0^4}{4Q_{\text{vis}}^2} \right) \approx \omega_0^2. \quad (3.33)$$

Thus, from observing the exponential decay of the envelope of the amplitude, the mechanical quality factor can be derived.

$$\ln \left| \frac{x(t + \Delta t)}{x(t)} \right| = -\omega_0 \Delta t / (Q_{\text{vis}}) \quad . \quad (3.34)$$

A typical measurement outcome is depicted in Fig. 3.7. From the time constant  $\tau$  of this decay, the quality factor  $Q$  could be derived by a fitting an appropriate exponential decay. In this case, a mechanical quality factor of  $Q = 0.58 \cdot 10^6$  for the fundamental oscillation mode was inferred and is confirmed by repeating the measurement multiple times.

A comparison of the two silicon nitride membranes used in the experiments presented in this thesis is given in table 3.1.

### 3 The mechanical oscillator

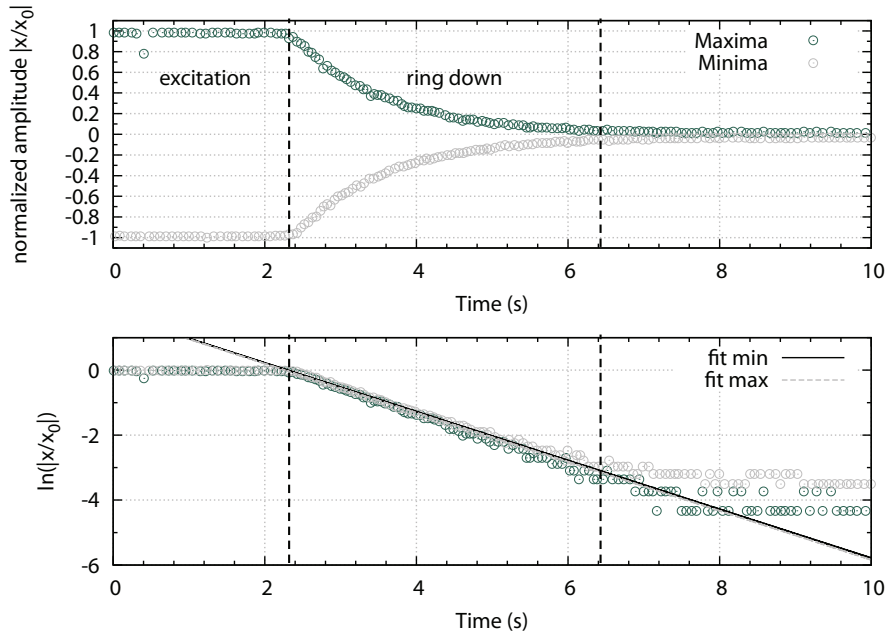


**Figure 3.7:** Ring-down measurement of the membrane mechanical quality factor for the fundamental mode of a SiN membrane at 133 kHz. Both, maxima and minima are plotted as function of time, and an exponential fit was made in order to derive the membrane’s mechanical quality factor.

**Table 3.1:** Relevant SiN membrane parameters for the membrane used in the 1064 nm and 1550 nm cryogenic experiment

		1064 nm	1550 nm
Resonance frequency (300 K)	$f_{\text{res}}$	133 kHz	155 kHz
Resonance frequency (8 K)	$f_{\text{res}}$	-	141.82 kHz
Mechanical quality factor (300 K)	$Q$	$0.58 \cdot 10^6$	$0.52 \cdot 10^6$
Mechanical quality factor (8 K)	$Q$	-	$6.8 \cdot 10^6$
Effective mass	$m_{\text{eff}}$	80 ng	130 ng
Size	$L_x$	1.5 mm	1.5 mm
Thickness	$d$	45 nm	75 nm
Power reflectivity	$r_m^2$	0.17	0.25

## 4

## Chapter 4

## Michelson-Sagnac interferometer

In this section, the Michelson-Sagnac interferometer is presented. The section provides information about the relevant quantum and classical noise contributions within the topology. Next, the experimental realisation of a Michelson-Sagnac interferometer is described. The section closes with a presentation of the achieved interferometric sensitivity.

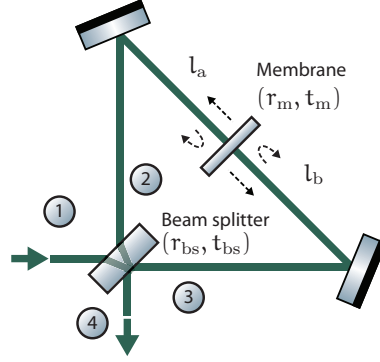
### 4.1 Interferometer topology

In this section, the Michelson-Sagnac interferometer topology [81, 83–86] is discussed. The basis is a Sagnac interferometer, formed by a beam splitter and two steering mirrors. The output power of the Sagnac interferometer depends on the beam splitter ratio and vanishes for a balanced beam splitter. The Michelson-Sagnac interferometer is established by placing a translucent mirror between the two steering mirrors. In the thesis present, this mirror was a SiN membrane, which was discussed in the previous chapter. It exhibits an amplitude reflectivity  $r_m$  and amplitude transmissivity  $t_m$ . The light reflected by the two sides of the membrane gives rise to two Michelson like optical mode. This mode is sensitive to membrane displacements, as the light accumulates a phase shift proportional to a membrane displacement. After circulation through the interferometer, all beams are overlapped on the beam splitter. A schematic of the interferometer is shown in Fig. 4.1.

When recombining, all field amplitudes add up with their respective phases, and the detected output power depends on the membrane position. The light field incident on the beam splitter with given amplitude reflection and transmission coefficients  $r_{ij}$  and  $t_{ij}$  is  $\alpha_{in}$ .

## 4 Michelson-Sagnac interferometer

**Figure 4.1:** Michelson-Sagnac interferometer topology. The incident beam is split by a beam splitter and folded by two steering mirrors. A translucent SiN membrane with amplitude reflectivity  $r_m$  and transmissivity  $t_m$  gives rise to a reflected and transmitted optical mode, indicated as black, dashed lines.



Here,  $i$  represents the input port and  $j$  the output port of the beam splitter respectively,  $i, j \in \{1, 2, 3, 4\}$  - compare Fig. (4.1), assuming  $r_{ij} = r_{ji}$  and  $t_{ij} = t_{ji}$  for reciprocity of light ways. To fulfil energy conservation, a phase flip of a total of  $\pi/2$  at the beam splitter is required [87]. There is no constrain on where to introduce the phase flip. For convenience we write

$$r_{ij} = r_{bs} e^{i\theta_{ij}} \quad , \quad (4.1)$$

$$t_{ij} = t_{bs} e^{i\theta_{ij}} \quad . \quad (4.2)$$

The phase relations for the beam splitter are chosen such that

$$\theta_{12} = -\theta_{34} \quad , \quad (4.3)$$

$$\theta_{13} = -\theta_{24} \pm \pi \quad . \quad (4.4)$$

A valid choice of phases is  $\theta_{12} = \theta_{34} = \theta_{24} = 0$  and  $\theta_{13} = \pi$ .

### Interferometer in transmission

The output port 4 of the beam splitter is the sum of four electric field amplitudes with their individually accumulated phases on their way to port 4.

$$\begin{aligned} \mathbf{a}_{\text{out}}^{\text{ifo}} = & \underbrace{\mathbf{a}_{\text{in}} t_m r_{bs}^2 e^{i\theta_{\text{SA1}}} + \mathbf{a}_{\text{in}} t_m t_{bs}^2 e^{i\theta_{\text{SA2}}}}_{\text{Sagnac}} + \\ & \underbrace{\mathbf{a}_{\text{in}} r_m r_{bs} t_{bs} e^{i\theta_{\text{MI1}}} + \mathbf{a}_{\text{in}} r_m r_{bs} t_{bs} e^{i\theta_{\text{MI2}}}}_{\text{Michelson}} . \end{aligned} \quad (4.5)$$

The phases can be written as



$$\theta_{SA1} = \theta_{12} + \theta_{34} + \theta_{tm} + k(l_a + l_b) \quad , \quad (4.6)$$

$$\theta_{SA2} = \theta_{13} + \theta_{24} + \theta_{tm} + k(l_a + l_b) \quad , \quad (4.7)$$

$$\theta_{MI1} = \theta_{12} + \theta_{24} + \theta_{rm} + 2k(l_a) \quad , \quad (4.8)$$

$$\theta_{MI2} = \theta_{13} + \theta_{34} + \theta_{rm} + 2k(l_b) \quad . \quad (4.9)$$

In this case  $l_a, l_b$  are the arm lengths of the interferometer (distance between beam splitter and membrane) and  $\theta_{rm}, \theta_{tm}$  are phase shifts for the light when reflected by or transmitted through the membrane.  $k = 2\pi/\lambda$  is the wave number,  $\lambda$  is the laser wavelength. Inserting the phases from Eq. (4.3) and (4.4) into (4.5) and using the identity [88]

$$e^{ix} + e^{iy} = e^{\frac{i}{2}(x+y)} \cdot 2 \cos\left(\frac{x-y}{2}\right) \quad , \quad (4.10)$$

we end up with the final expression for the interferometer output field.

$$\begin{aligned} \frac{a_{out}^{ifo}}{a_{in}} = t_{ifo} = & \underbrace{t_m e^{i\theta_{SA1}} (r_{bs}^2 - t_{bs}^2)}_{\text{Sagnac}} \\ & + \underbrace{r_{bs} t_{bs} r_m e^{\frac{i}{2}(\theta_{MI1} + \theta_{MI2})} 2 \cos\left(\frac{\theta_{MI1} - \theta_{MI2}}{2}\right)}_{\text{Michelson}} . \end{aligned} \quad (4.11)$$

Eq. (4.11) is the most general expression for the interferometer output field. The first part of the equation still represents the Sagnac-like interferometer and deserves some explanation. First of all it is independent of the membrane position. The phase  $\theta_{SA1}$  is only dependent on the sum of the interferometer arm lengths  $k(l_a + l_b)$ . Also, for a balanced beam splitter ( $r_{bs}^2 = t_{bs}^2 = 0.5$ ) it vanishes. For simplicity, a balanced beam splitter is assumed from now on and only the second term is investigated.  $\theta_{MI1} + \theta_{MI2}$  is constant (independent of the membrane position as well), rendering the phase factor irrelevant. The last factor is a function of the differential phases  $\theta_{MI1} - \theta_{MI2}$  and the respective term is actually sensitive to differential arm length caused by some membrane motion.

The modulus square of Eq. (4.11) is the normalised interferometer output power in transmission  $P_{out}^t$ , which can be monitored by some kind of photo detector

## 4 Michelson-Sagnac interferometer

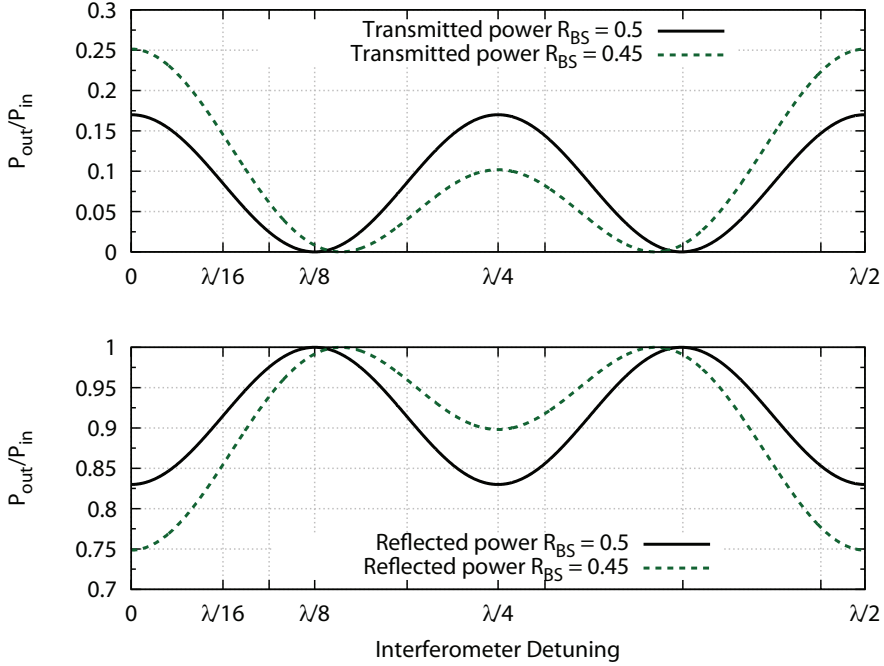


**Figure 4.2:** Normalised interferometer output power for a membrane with  $r_m^2 = 0.17$  for two different beam splitter ratios  $r_{bs}^2 = 0.5$  and  $r_{bs}^2 = 0.45$ , respectively. The bright-fringe detunings remain the same whereas to achieve a dark output port, the Michelson interferometer has to be detuned to compensate for the remaining Sagnac amplitude.

$$\frac{P_{out}^t}{P_{in}} = \left| \frac{\mathbf{a}_{out}^{ifo}}{\mathbf{a}_{in}} \right|^2 = r_m^2 \frac{1}{2} (1 + \cos(4k\Delta x)) \quad . \quad (4.12)$$

In this case, a detuning  $\Delta x = \frac{\pi}{4k} \cdot 2n$ ,  $n \in \mathbb{N}$  corresponds to maximal output power, whereas  $\Delta x = \frac{\pi}{4k} (2n + 1)$  produces a dark interferometer output. These very tunings will be referred to as *bright-fringe* and *dark-fringe* condition from now on. Either tuning is also possible for an unbalanced beam splitter as depicted in Fig (4.2), as long as the membrane amplitude reflectivity allows for compensation of the uncanceled Sagnac amplitudes [76].

### Interferometer in reflection

The electric field in the interferometer input port is again a sum of four electric amplitudes

$$\frac{\mathbf{a}_{\text{refl}}^{\text{ifo}}}{\mathbf{a}_{\text{in}}} = r_{\text{ifo}} = t_{\text{m}} r_{\text{bs}} t_{\text{bs}} e^{i\theta_{\text{SA1}}^{\text{r}}} + t_{\text{m}} r_{\text{bs}} t_{\text{bs}} e^{i\theta_{\text{SA2}}^{\text{e}}} + r_{\text{bs}}^2 r_{\text{m}} e^{i\theta_{\text{MI1}}^{\text{r}}} + t_{\text{bs}}^2 r_{\text{m}} e^{i\theta_{\text{MI2}}^{\text{r}}} \quad (4.13)$$

with their individual phases

$$\theta_{\text{SA1}}^{\text{r}} = \theta_{12} + \theta_{13} + \theta_{\text{tm}} + k(l_{\text{a}} + l_{\text{b}}) \quad , \quad (4.14)$$

$$\theta_{\text{SA2}}^{\text{r}} = \theta_{13} + \theta_{12} + \theta_{\text{tm}} + k(l_{\text{a}} + l_{\text{b}}) \quad , \quad (4.15)$$

$$\theta_{\text{MI1}}^{\text{r}} = \theta_{12} + \theta_{12} + \theta_{\text{rm}} + 2k(l_{\text{a}}) \quad , \quad (4.16)$$

$$\theta_{\text{MI2}}^{\text{r}} = \theta_{13} + \theta_{13} + \theta_{\text{rm}} + 2k(l_{\text{b}}) \quad . \quad (4.17)$$

Using the identity [88]

$$e^{ix} - e^{iy} = e^{\frac{i}{2}(x+y)} \cdot 2i \sin\left(\frac{x-y}{2}\right) \quad , \quad (4.18)$$

gives the total power reflectivity of the interferometer as

$$\frac{P_{\text{out}}^{\text{r}}}{P_{\text{in}}} = \left| \frac{\mathbf{a}_{\text{refl}}^{\text{ifo}}}{\mathbf{a}_{\text{in}}} \right|^2 = 1 - r_{\text{m}}^2 \frac{1}{2} (1 + \cos(4k\Delta x)) \quad . \quad (4.19)$$

### Nodes and anti-nodes

The optical field at each point within a Sagnac interferometer (without a membrane) is a superposition of two counter-propagating waves, with their individual phases  $\Theta_{\text{SA1}} = kl_{\text{a}}$  and  $\Theta_{\text{SA2}} = \pi + kl_{\text{b}}$ , resulting in a field amplitude

$$\mathbf{a} = r_{\text{bs}} e^{-ikl_{\text{a}}} - t_{\text{bs}} e^{-ikl_{\text{b}}} \quad . \quad (4.20)$$

For a balanced beam splitter,  $r_{\text{bs}} = t_{\text{bs}} = 1/\sqrt{2}$ , this sum vanishes if

$$k(l_{\text{a}} - l_{\text{b}}) = (2n + 1)\pi \Leftrightarrow \Delta x = \frac{\pi}{2k} (2n + 1), \quad n \in \mathbb{N} \quad . \quad (4.21)$$

When compared to Eq. (4.12), one finds that a dark-fringe corresponds to a membrane position in the node of the electric field of the standing wave within the Sagnac interferometer. Positioning the membrane in an anti-node  $\Delta x = \frac{\pi}{4k} (2n)$  of the standing wave also produces a dark-interferometer output port. The sub-wavelength thickness of the membrane thus allows to position the membrane exactly

## 4 Michelson-Sagnac interferometer

---

in a node, thereby minimising the optical absorption. In [84], it was demonstrated that the resulting optical absorption can be minimized to below 5.4 ppm for a membrane of thickness  $d = 60$  nm at a laser wavelength of 1064 nm if exploiting a node position.

### 4.2 Interferometric signals and noise

The interferometer output port can be monitored by a single photo detector. It generates an electric current proportional to the incident light power. If the membrane moves (oscillates), a change (oscillation) of the output power will be detected. The amplitude of the detected signal depends on the interferometer tuning, since the derivative  $\partial P_{\text{out}}/\partial x$  is depending on the tuning. The maximal signal is obtained if the interferometer is operated on mid-fringe, whereas no signal can be detected on dark- and bright fringe.

#### 4.2.1 The shot noise limit

The photons detected in the interferometer output are considered to be uncorrelated in time. The one-sided, linear spectral density of the optical shot noise [89] can then be written as [90] (compare Eq. 2.13)

$$G_{\text{shot}} = \sqrt{2\hbar\omega P_{\text{out}}} = \sqrt{\frac{4\pi\hbar c P_{\text{out}}}{\lambda}}. \quad (4.22)$$

The shot noise is proportional to the square root of the interferometer output power, whereas an interferometric signal is proportional to the optical power incident on the interferometer. Both result in a fluctuation of detected output power, rendering both indistinguishable. Optical shot noise results in an apparent length noise. Division of the shot noise by the signal for some tuning (arm length difference)  $\Delta x$  of the interferometer yields

$$\frac{G_{\text{shot}}}{|\partial P_{\text{out}}/\partial x|} = \sqrt{\frac{\hbar c \lambda}{8\pi r_m^2 P_{\text{in}}}} \frac{\sqrt{1 + \cos(4kx)}}{|\sin(4kx)|}. \quad (4.23)$$

The last equality was achieved by inserting Eq. (4.12) for the interferometer output power  $P_{\text{out}}$ . The minimal value of Eq. (4.23) is achieved if  $x = \pm \frac{\pi}{4k}$ . This is the dark-fringe condition,  $P_{\text{out}}(\frac{\pi}{4k}) = 0$ . The single-sided linear spectral density of the relative error caused by shot noise on dark-fringe is

$$G_{\text{shot}}^x = \sqrt{\frac{\hbar c \lambda}{16\pi r_m^2 P_{\text{in}}}} \quad (4.24)$$

For a given laser wavelength  $\lambda$  and a membrane with power reflectivity  $r_m^2$ , the shot noise imprecision of the position measurement in this setup can be lowered by increasing the incident laser power  $P_{\text{in}}$  only. Another possibility is the injection of a squeezed vacuum state into the interferometer output port as has been demonstrated in table-top interferometers [22, 91–93] and large-scale gravitational wave detectors [94, 95].

### 4.2.2 Quantum back-action noise

A second source of quantum noise is due to the position measurement itself as each photon reflection is associated with a force, acting on the membrane  $F_{\text{ph}} = 2\hbar k$  per photon. A mean optical power  $P$  corresponds to  $P/(\hbar\omega)$  photons per time unit, such that  $F = (2/c)P$ . The force spectral density then follows out of Eq. (2.13) and corresponds to a white, single-sided force spectral density of [86]

$$G_{\text{rpn}}^F = \sqrt{\frac{16\pi\hbar r_m^2 P_{\text{in}}}{c\lambda}} \quad (4.25)$$

According to Eq. (3.10), this force causes an oscillator displacement, with a spectral density given by

$$G_{\text{rpn}}^x = |G(\omega)| \sqrt{\frac{16\pi\hbar r_m^2 P_{\text{in}}}{c\lambda}} \quad (4.26)$$

This photon back-action shot noise is also referred to as radiation pressure shot noise. In 1980, Carlton Caves terminated an ongoing discussion on whether or not quantum shot noise would disturb the measurement, as it was unclear why a perfectly balanced beam splitter would not translate (quantum) laser fluctuations equally in the two interferometer arms. Caves was able to explain the origin with vacuum fluctuations, entering the interferometer through the second beam splitter port [16]. As such, they are anti-correlated in the two interferometer arms because of the beam splitter phase relations and hence cause a differential motion of the test mass, or oscillator in the case of the Michelson-Sagnac interferometer.

The first experimental observation of quantum back-action noise was published in [96]. An associated effect is ponderomotive squeezing of

## 4 Michelson-Sagnac interferometer

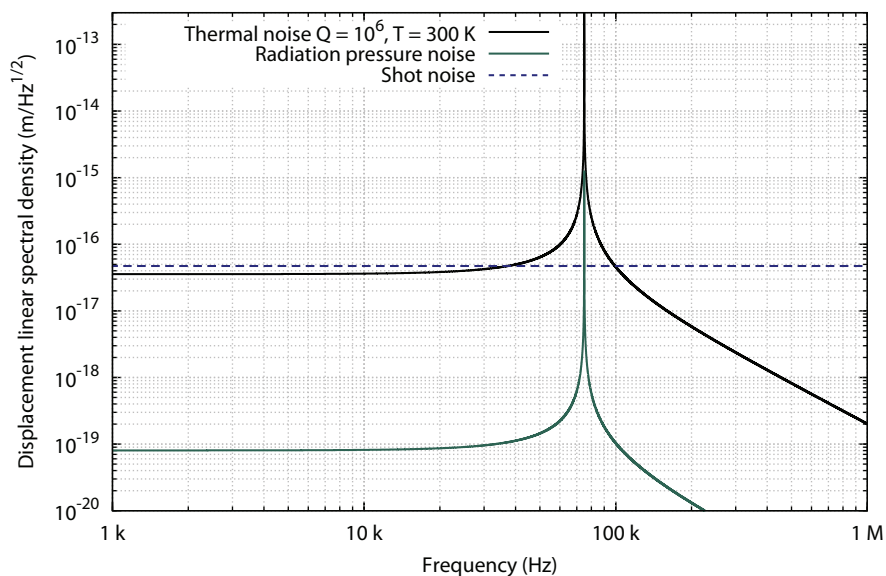


**Figure 4.3:** Radiation pressure, thermal noise and shot noise for an input power of  $P_{\text{in}} = 1$  W, and an oscillator with  $R_m = 0.3$ ,  $Q = 10^6$ ,  $T = 300$  K and mass  $m = 125$  ng, with a resonance frequency of  $f_{\text{res}} = 75$  kHz, considered for a laser wavelength  $\lambda = 1064$  nm.

the light field reflected of the membrane, which has been demonstrated in [97, 98].

For experimental parameters, Fig. 4.3 depicts the linear spectral densities of thermal and quantum noise, for an interferometric operation on dark-fringe and a laser input power of  $P_{\text{in}} = 1$  W. As can be seen, the radiation pressure noise is about 3 orders of magnitude smaller than the other contributions. For a direct observation, the shot noise level has to be decreased, by either applying 1 kW of optical input power at the beam splitter (which will only be possible by a power recycling mirror), or alternatively, the equivalent gain by signal-recycling. In either case, the thermal noise of the oscillator has to be reduced drastically, which makes it necessary to operate the experiment with cryogenic temperatures. The noise contributions are considered in [86], and depicted in Fig. 4.4

For a temperature  $T = 1$  K, the thermal noise is reduced by a factor of  $\sqrt{300}$ , (compare Eq. (3.25)). The mechanical quality factor is assumed to be increased by one order of magnitude at low temperatures, as it has been observed by [77] previously. In this case, the spectrum is dominated by radiation pressure noise at all frequencies.

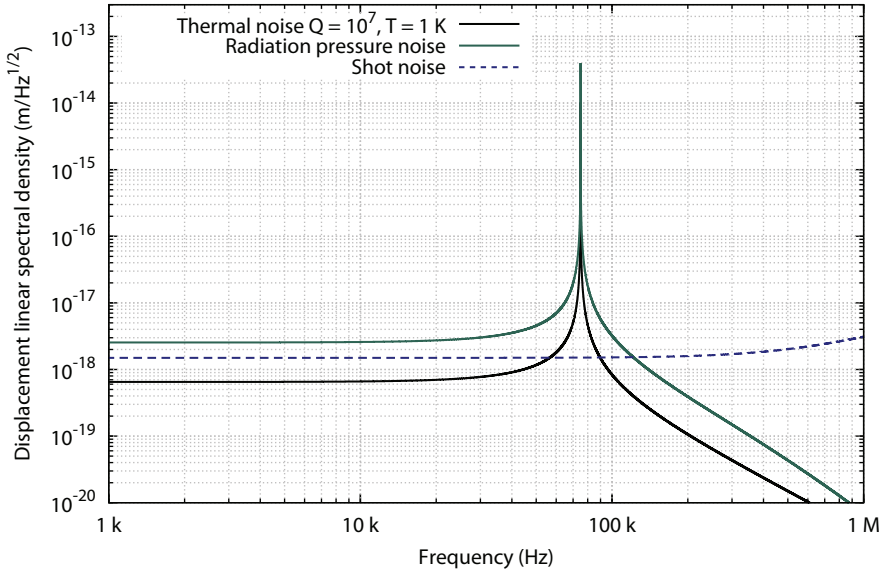


**Figure 4.4:** The experimental noise budget with an oscillator of temperature  $T = 1$  K and  $R_{sr} = 99.6\%$  power reflectivity signal-recycling mirror. The length of the recycling cavity is assumed to be 12 cm. In this case, the measurements would be limited by radiation pressure shot noise.

It is worth mentioning that both, radiation pressure noise and shot noise originate from the fact that photons are discrete and that they obey a Poisson statistics. Both, force as well as power spectral densities are frequency independent. The frequency dependence in the measurement of the displacement arises because of a frequency dependent mechanical response.

### 4.2.3 Standard quantum limit

Optical shot noise and back-action noise give rise to the standard quantum limit (SQL) for the interferometric readout precision. In case of the Michelson-Sagnac interferometer, for each frequency there exists an optimal laser power  $P_{sql}$ . This can be seen by Eq. (4.23) and Eq. (4.26) and regarding their sum, which is assumed to be uncorrelated.

$$\begin{aligned} G_{total}^x{}^2(P) &= G_{shot}^x{}^2(P) + G_{rpn}^x{}^2(P) \\ &= \frac{\hbar c \lambda}{16\pi r_m^2 P_{in}} + |G(\omega)|^2 \frac{16\pi \hbar r_m^2 P_{in}}{c \lambda} \end{aligned} \quad (4.27)$$

## 4 Michelson-Sagnac interferometer

---

The sum in Eq. 4.27 is minimized if  $\partial/\partial P G_{\text{total}}^2(P) = 0$ , which is the case if the input power  $P = P_{\text{sql}}$ , where

$$P_{\text{sql}} = \frac{c\lambda}{16\pi|G(\omega)|r_m^2} \quad . \quad (4.28)$$

Equation (4.28) shows that  $P_{\text{sql}}$  is a function of frequency. The minimal total noise is given by

$$G_{\text{tot,sql}}^x = \sqrt{2\hbar|G(\omega)|} \quad . \quad (4.29)$$

The maximal value of the SQL is reached at the mechanical resonance frequency,

$$G_{\text{tot,sql}}^x = \sqrt{\frac{2\hbar Q}{m\omega_m^2}} \quad . \quad (4.30)$$

It is a common misassumption [99, 100] that achieving a total noise below this peak value at arbitrary frequencies is of any importance for a displacement (or force) measurement or would beat the standard quantum limit. It is rather obvious from equation (4.29) that such a situation always occurs if the mechanical quality  $Q$  is high enough. The comparison between measurement precision at one frequency, and the standard-quantum limit at another frequency is invalid. A measurement can only claim to beat the SQL at some frequency if the observed total noise is smaller than the SQL at this very frequency [83].

The 'correct' way to beat the SQL is based on another idea of Caves. He suggested to replace the vacuum state entering the interferometer by a squeezed vacuum state of light. [20]. Squeezed states of light exhibit unequal variances in both quadratures, with a variance smaller than the variance of a vacuum state in one particular quadrature. Thereby, it is possible to reduce the noise in one quadrature at the expense of the other, orthogonal quadrature. The ideal squeezing quadrature depends on the frequency, as do radiation pressure and optical shot noise. Kimble proposed optical filter cavities [25], which induce a frequency dependent phase rotation, to accomplish a frequency dependent squeezing angle. It is thereby possible to beat the SQL on a broad frequency range.



### Comparison of individual noise contribution

It is useful to compare the individual displacement spectral densities of both, quantum and thermal displacement noise for a Michelson-Sagnac interferometer. Here, this comparison is given for two cases. First, the spectral densities at the mechanical resonance frequency ( $\omega = \omega_m$ ), which is assumed as  $\omega_m = 2\pi \cdot 75$  kHz yield

$$\begin{aligned} G_{\text{therm}}^x &= 3.55 \cdot 10^{-11} \frac{\text{m}}{\sqrt{\text{Hz}}} \left( \frac{125 \text{ ng}}{\text{m}} \frac{Q}{10^6} \frac{T}{300 \text{ K}} \right)^{1/2}, \\ G_{\text{shot}}^x &= 4.72 \cdot 10^{-17} \frac{\text{m}}{\sqrt{\text{Hz}}} \left( \frac{1 \text{ W}}{P_{\text{in}}} \frac{\lambda}{1064 \text{ nm}} \frac{0.3}{r_m^2} \right)^{1/2}, \\ G_{\text{rpn}}^x &= 2.01 \cdot 10^{-14} \frac{\text{m}}{\sqrt{\text{Hz}}} \left( \frac{Q}{10^6} \right) \left( \frac{P_{\text{in}}}{1 \text{ W}} \frac{r_m^2}{0.3} \frac{1064 \text{ nm}}{\lambda} \frac{125 \text{ ng}}{\text{m}} \right)^{1/2}. \end{aligned}$$

For frequencies  $f \ll f_m$  smaller than the mechanical resonance frequency, the thermal noise depends on the damping mechanism (structural or viscous). The displacement spectral densities are given by

$$\begin{aligned} G_{\text{therm}}^{x,\text{vi}}(f) &= 3.55 \cdot 10^{-17} \frac{\text{m}}{\sqrt{\text{Hz}}} \left( \frac{125 \text{ ng}}{\text{m}} \frac{T}{300 \text{ K}} \right)^{1/2}, \\ G_{\text{therm}}^{x,\text{st}}(f) &= 3.08 \cdot 10^{-17} \frac{\text{m}}{\sqrt{\text{Hz}}} \left( \frac{125 \text{ ng}}{\text{m}} \frac{T}{300 \text{ K}} \frac{10^6}{Q} \frac{1 \text{ kHz}}{f} \right)^{1/2}, \\ G_{\text{shot}}^x(f) &= 4.72 \cdot 10^{-17} \frac{\text{m}}{\sqrt{\text{Hz}}} \left( \frac{1 \text{ W}}{P_{\text{in}}} \frac{\lambda}{1064 \text{ nm}} \frac{0.3}{r_m^2} \right)^{1/2}, \\ G_{\text{rpn}}^x(f) &= 2.01 \cdot 10^{-20} \frac{\text{m}}{\sqrt{\text{Hz}}} \left( \frac{P_{\text{in}}}{1 \text{ W}} \frac{r_m^2}{0.3} \frac{1064 \text{ nm}}{\lambda} \frac{125 \text{ ng}}{\text{m}} \right)^{1/2}. \end{aligned}$$

As can be seen from the first set of equations, the observation of radiation pressure noise at given temperature is most likely for high mechanical quality factors  $Q$ , low oscillator mass  $m$ , high optical input power  $P_{\text{in}}$  and observation at the mechanical resonance frequency, as reported in [96].

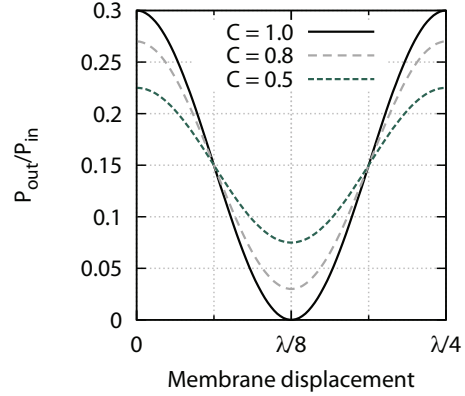


**Figure 4.5:** Ratio of Michelson-Sagnac interferometer output power  $P_{\text{out}}/P_{\text{in}}$  in case of a balanced beam splitter for three values of interferometric contrast  $C$ . Here, a membrane power reflectivity  $r_m^2 = 0.3$  was assumed.

### 4.3 Influence and suppression of laser noise

This section describes the effect classical laser amplitude and frequency noise. The considerations focus on technical laser amplitude and frequency noise. Their impact on the interferometric measurement of the membrane position is described with regards to a realistic experimental situation: a small, but non-vanishing arm length difference of the interferometer, and an imperfect interference contrast.

#### 4.3.1 Interferometer contrast

Although the signal to shot noise ratio is maximized mathematically on dark-fringe, measurements with a single photo diode will become insensitive at this point of operation, such that an infinitesimal offset from dark-fringe is required. Here, it is shown that this offset can not be arbitrarily small in the experiment. So far, Eq. (4.11) was taken as complete description of the interferometer output power, but silently assumed a perfect interferometer contrast  $C$ , which is defined as follows

$$C = \frac{P_{\text{max}} - P_{\text{min}}}{P_{\text{max}} + P_{\text{min}}} . \quad (4.31)$$

Here  $P_{\text{max}}$  and  $P_{\text{min}}$  are the maximal and minimal interferometer output power. In the perfect case, and for a balanced beam splitter,  $P_{\text{min}} = 0$  and  $P_{\text{max}} = r_m^2 P_{\text{in}}$ , such that it gives  $C = 1$  for  $P_{\text{min}} = 0$ . In reality,  $C$  is a measure of the interferometer quality, and usually  $C < 1$ . This is caused by a variety of reasons, such as differential losses in the interferometer arms, imperfect alignment or non-ideal mode matching.

### 4.3 Influence and suppression of laser noise

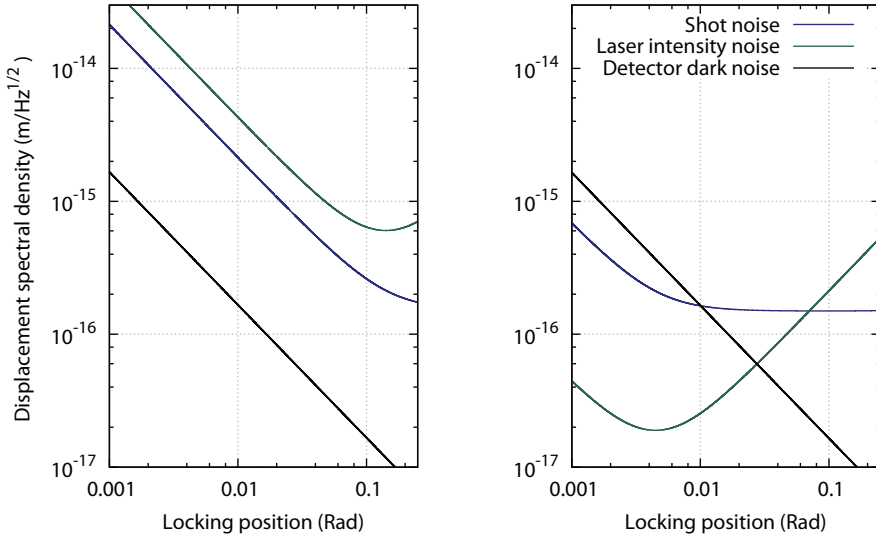


**Figure 4.6:** Shot noise, technical laser noise and detector dark noise as function of the interferometer tuning of dark-fringe. Left : interferometer contrast  $C = 99\%$  and right  $C = 99.999\%$ . Electronic dark noise is assumed equal in both measurements. In the experiment, it is reduced by higher electronic gain of the photo detector.

A contrast  $C < 1$  thus implies that the interferometer output power on dark-fringe is non-vanishing. The interferometer output power then writes (compare Eq. (4.12))

$$P_{\text{out}} = P_{\text{in}} \frac{r_m^2}{2} (1 + C \cos(4kx)) \quad . \quad (4.32)$$

On dark-fringe, its derivative for the membrane microscopic position is zero, however. The signal to noise ratio (and associated interferometer displacement sensitivity) then exhibits an maximal value, which is achieved for some interferometer dark-fringe offset. Figure 4.6 shows the displacement sensitivity of the same Michelson-Sagnac interferometer with two different interferometer contrast values. The membrane power reflectivity was assumed  $r_m^2 = 0.3$ , and an optical input power of  $P_{\text{in}} = 100$  mW. The plot also includes technical laser amplitude noise, which is described in Sec. 4.3.4. In both cases, the same electronic dark-noise is assumed, although this noise could be reduced by a higher electronic gain in the photo detector. In any case, the optimum interferometer working point depends on the interference contrast  $C$ , and a higher interference contrast allows for a more precise measurement, closer to the dark-fringe.

### 4.3.2 Interferometer arm length differences

Non-ideal destructive interference of the two Michelson modes at the beam splitter and hence,  $C < 1$  can be caused by a macroscopic interferometer arm length difference of the interferometer. This can be modelled by two Gaussian modes with same waist size but a lateral displacement  $\Delta z_R$  of the two waist positions. The overlap of such two optical modes is given by Eq. (4.33) and depicted in Fig. 4.7. For  $C < 1$ , the interferometer will transmit a fraction of the incident laser carrier and thus couple technical amplitude fluctuations into the read out:

$$\begin{aligned} C &= \frac{2\sqrt{z_{R1}}\sqrt{z_{R2}}}{\sqrt{(z_1 - z_2)^2 + (z_{R1} + z_{R2})^2}} \\ &= \frac{2z_R}{(\Delta z^2 + 4z_R^2)^{1/2}} = \frac{1}{\sqrt{1 + (\frac{\Delta z}{2z_R})^2}} \end{aligned} \quad (4.33)$$

Here  $z_R$  denotes the Rayleigh range  $z_R = \pi\omega_0^2/\lambda$ . A laser wavelength  $\lambda = 1064$  nm and a waist size of  $\omega_0 = 500$   $\mu\text{m}$  were chosen.

Despite suppression of the technical amplitude laser noise in the read out, the interference contrast becomes important when a high-reflective recycling mirror is to be installed in the interferometer output port, because the interference contrast should exceed the recycling mirror reflectivity in order to provide an under-coupled cavity condition.

The higher the desired contrast is, the smaller the arm-length difference has to be. In the experiment, a piezo stepped stage is placed underneath the membrane holder to allow the membrane to be positioned such that the arm-length difference is smaller than 1 mm. It is an unanswered question whether

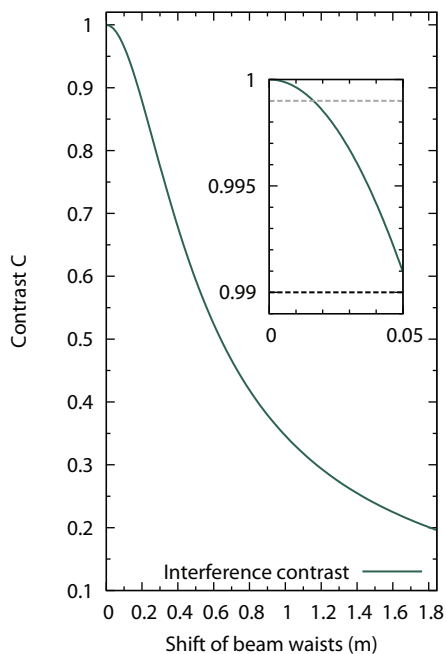


**Figure 4.7:** Achievable interferometer contrast  $C$  as function of arm length differences.

the best arm-length difference is 0, as this would eliminate the possibility to stabilize the interferometer to dark-fringe by the so-called *frontal* modulation scheme [101].

### 4.3.3 Laser frequency noise

The macroscopic arm length difference  $\Delta L$  is also subject to another type of length noise. If the laser exhibits frequency noise  $\delta\tilde{\nu}$  (which is the case for any laser), this leads to an apparent length noise [102], given by

$$\delta\tilde{s} = \frac{\delta\tilde{\nu}}{\nu} \Delta L \quad , \quad (4.34)$$

where  $\nu$  is the mean laser frequency. The typical technical laser frequency noise of an *Innolight* [103] Mephisto NPRO Laser was measured numerous times, for example in [102, 104, 105]. Both technical amplitude and frequency noise can be caused by fluctuations of the laser resonator crystal length or pump power. A fundamental source of noise results from quantum fluctuations, perturbing the phase of the carrier. This gives rise to the so called Shawlow-Townes limit [7]. It states that the frequency spectral density ( $\text{Hz}/\sqrt{\text{Hz}}$ ) is frequency independent and given by

$$s^{\text{ST}}(f) = \delta_\nu \sqrt{\frac{\hbar\pi c}{P\lambda}} \quad . \quad (4.35)$$

Where  $\delta_\nu$  is the laser resonator linewidth, which is specified [103] to  $\delta_\nu = 1$  kHz for the *Innolight* Mephisto NPRO laser. With  $\lambda = 1064$  nm and  $P = 1$  W, Eq. (4.35) yields

$$s^{\text{ST}}(f) = 3.05 \cdot 10^{-7} \text{Hz}/\sqrt{\text{Hz}} \quad .$$

Fortunately, this is not a limiting factor when using the *Innolight* laser, as this limit is only achieved for high frequencies. However, it can be important when using other laser sources with a significantly larger cavity linewidth of the laser resonator. Here, only the classical contribution of the laser frequency noise is relevant for the experiment. It can be approximately projected as [102, 106]

$$\delta\tilde{\nu}(f) = 10 \text{ kHz} \cdot \frac{1}{\sqrt{\text{Hz}}} \cdot \frac{1 \text{ Hz}}{f} \quad . \quad (4.36)$$

If the interferometer arm length inequality assumed to be  $\Delta L = 1$  mm and  $\delta\tilde{\nu}(100 \text{ kHz}) = 1 \text{ Hz}/\sqrt{\text{Hz}}$ , this leads to an apparent length noise

## 4 Michelson-Sagnac interferometer

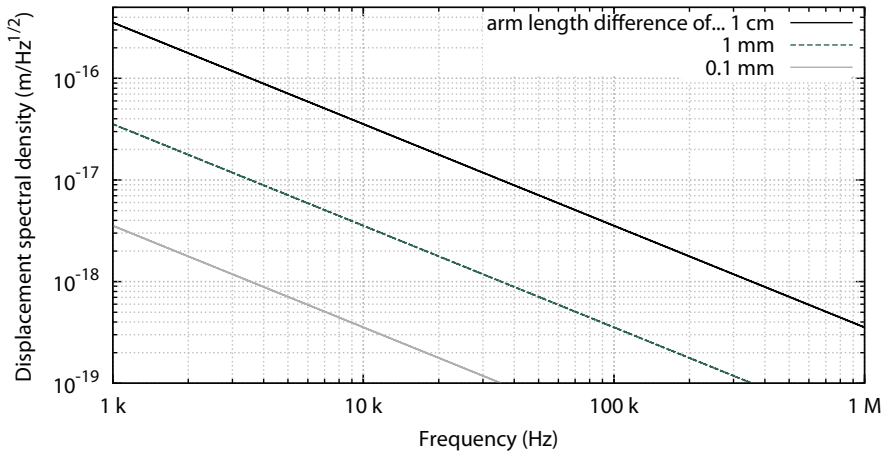


**Figure 4.8:** Laser frequency noise projection into apparent length noise for the *Mephisto* NPRO laser for three absolute arm length differences of the Michelson interferometer. Note that the  $1/f$  projection is an approximation, which is less accurate for frequencies above 100 kHz.

of  $\delta\tilde{s} = 3.546 \cdot 10^{-18} \text{ m}/\sqrt{\text{Hz}}$ . Thus, the arm length difference has to be kept smaller than 1 mm or the laser has to have an active laser frequency stabilisation to suppress the frequency noise at 100 kHz. Frequency noise becomes important again as soon as the experiment uses a signal recycling mirror (see Sec. 5).

### 4.3.4 Laser intensity noise

Another important source of noise is technical fluctuation of the laser intensity. Lasers are often times characterised by their relative intensity noise (RIN), which is power fluctuations divided by average detected power. The RIN typically depends on the Fourier frequency, as the sources for the noise are frequency dependent, but does not depend on the average detected power  $P$ .

The influence of laser intensity noise is two-fold. First, technical fluctuations of the laser intensity cause a 'classical' force, acting on the oscillator, just as in case of quantum shot noise. It causes a displacement spectral density of

$$|S_x(\omega)| = \frac{2}{c} |S_I(\omega)| r_m^2 \Delta_{bs} |G(\omega)| \quad , \quad (4.37)$$

with  $|S_I(\omega)| = P \cdot \text{RIN}$  being the spectral density of the laser fluctuations. In contrast to the vacuum fluctuations, the laser fluctuations are common in both interferometer arms, such that a suppression factor  $\Delta_{bs} = |t_{bs}^2 - r_{bs}^2|$ , representing the beam splitter unbalancing is introduced. To achieve a situation, in which the excitation is dominated by quantum noise, the power spectral densities of photon shot noise and technical laser noise are compared, their ratio should exceed unity. This is equivalent to

$$\frac{G_{\text{shot}}}{|S_I(\omega)|} > 1 \Leftrightarrow \sqrt{\frac{4\pi\hbar c}{\lambda}} > \Delta_{bs} \cdot \text{RIN} \cdot \sqrt{P} \quad . \quad (4.38)$$

Equation (4.38) is best understood when calculating its left hand side. For  $\lambda = 1064 \text{ nm}$ , it rewrites

$$6 \cdot 10^{-10} \sqrt{\frac{W}{\text{Hz}}} > \Delta_{bs} \cdot \text{RIN} \cdot \sqrt{P}$$

Typical RIN values for high quality, commercial laser sources are  $2 \cdot 10^{-7} / \sqrt{\text{Hz}}$  for frequencies below 1 MHz. If the beam splitter is lossless and  $r_{bs}^2 = 0.505 \Rightarrow \Delta_{bs} = 10^{-2}$ , Eq. (4.38) will only be fulfilled if  $P < 100 \text{ mW}$ . In order to achieve the same ratio at higher laser powers  $P$ , the product of  $\Delta_{bs} \cdot \text{RIN}$  has to be reduced.

The second influence of laser intensity fluctuations is concerning the read out. In case of DC read out and dark-fringe offset, a mean power will be measured by the photo detector. Thus, fluctuations of the interferometer output power directly translate into apparent displacement noise. Whether or not these fluctuations are negligible

## 4 Michelson-Sagnac interferometer

---

or dominant in the output spectrum depends on the laser quality and the amount of detected light in the interferometer output. The relative shot noise is

$$\frac{G_{\text{shot}}}{P} = \sqrt{\frac{4\pi\hbar c}{\lambda P}} . \quad (4.39)$$

If an optical power of  $P_{\text{out}} = 1 \text{ mW}$  is to be detected, the technical laser noise at a RIN level of  $10^{-7}$  is

$$|S_I(\omega)| = 10^{-10} \text{ W}/\sqrt{\text{Hz}} .$$

The shot noise level at this power is (compare Eq. 2.12)

$$G_{\text{shot}} = 1.93 \cdot 10^{-11} \text{ W}/\sqrt{\text{Hz}} .$$

If no other noise sources are present, the measured spectrum will thus not be dominated by shot noise at low frequencies but technical laser noise. Hence, performing precision measurements at these frequencies thus requires a stabilised laser. Laser stabilisation can either be done in active or passive schemes, as outlined in the following.

### Passive stabilisation

Passive stabilisation schemes exploit the amplitude transfer function of an optical cavity (see section 5.1) , which can be modelled as the equivalent to an optical low pass filter. The laser is incident to an impedance matched cavity, which is kept resonant. Amplitude fluctuations are transmitted only within the cavity linewidth (see section 5.1). Passive stabilisation requires the cavity optical linewidth to be much smaller than the frequency at which the noise is to be suppressed, which turns out to be challenging in table-top experiments when noise at frequencies around 100 kHz is to be suppressed. At low frequencies, passive stabilisation schemes are inferior to active stabilisations.

### Active stabilisation

Active stabilisation schemes consist of an electronic feedback loop and some power actuating device. The advantage of active stabilisation is that gain and resulting noise suppression is variable. The limitations for an active stabilisation are given by the speed of the electronics and the actuator in use. Also, at 10 MHz, each meter of electric connection already causes a phase loss of about 18 deg [107], which is why unity-gain frequencies above 1 MHz get more and more difficult



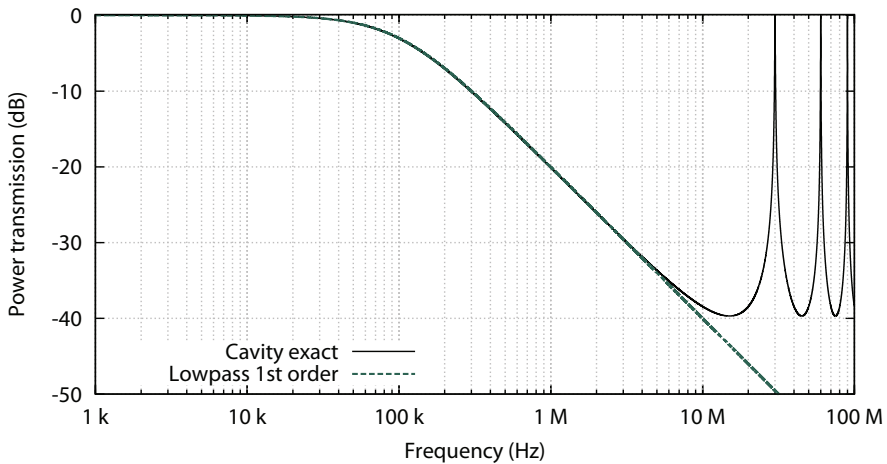


**Figure 4.9:** Transmitted power through an impedance matched optical cavity with an optical linewidth of 100 kHz. The cavity length is 10 m, which results in a free spectral range of 15 MHz. The finesse is 150. The green dashed line shows the approximation by a first order lowpass filter. A suppression of  $-3$  dB is achieved at 100 kHz. Additional suppression at this frequency can just be achieved by a more narrow optical linewidth, which means higher finesse or cavity length.

to achieve. At high frequencies, active stabilisation is thus inferior to passive stabilisations.

One possibility to actively stabilise the laser intensity is by using an auxiliary interferometer, operating close to constructive interference in the interferometer output port. A variable fraction of light is transmitted towards the other interferometer output port. A piezo driven mirror can be used to actuate the relative phase. The unity-gain frequency of this stabilisation will be limited to some kHz because of mechanical resonances of the piezo actuator.

For a sufficient noise suppression at 100 kHz, a fast amplitude stabilisation was required. The scheme used is depicted in Fig. 4.11. It uses a  $\lambda/2$  wave plate in front of an electro-optic amplitude modulator (EOAM), which in combination with a polarising beam splitter, served as a power actuator. A small fraction of the laser light is detected in transmission of this arrangement, and is compared to an ultra-stable current reference. The difference between both the signal and the reference is used as an error signal, which after electronic processing is then fed back to the EOAM. This scheme has already been used in [106].

## 4 Michelson-Sagnac interferometer

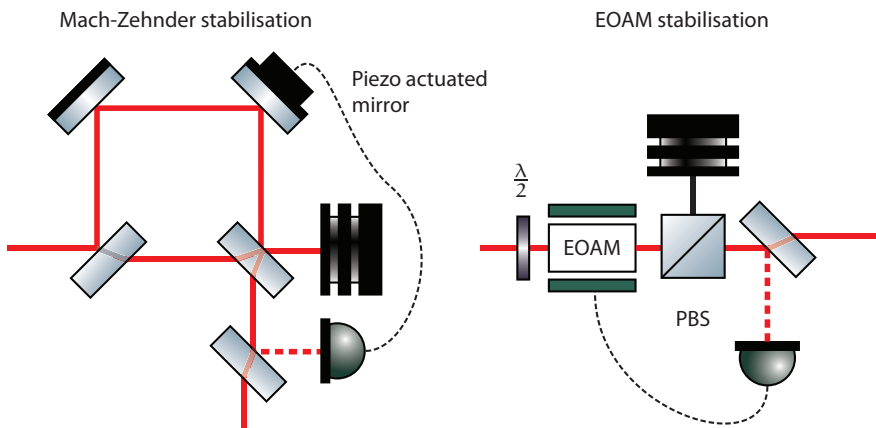


**Figure 4.10:** Left: power stabilisation via a Mach-Zehnder interferometer. Right: high-speed setup with an EOAM. In both cases, one port of the beam splitter (PBS) is used to dump a part of the power, and a small pick-up in the output port is required.

### 4.3.5 Laser light preparation

In the experiment, an *Innolight* Mephisto non-planar ring oscillator, operated at a laser wavelength of  $\lambda = 1064$  nm with an optical output power of 2 W was used. This type of laser source was characterized in different works before [106, 108], and was found to exhibit a low RIN level of about  $2 \cdot 10^{-7} \sqrt{\text{Hz}}$  at frequencies  $f < 1$  MHz. The laser relaxation oscillation at 1 MHz was suppressed by an integrated *noise-eater* function.

The laser light preparation is shown in Fig. 4.11. To eliminate higher order optical modes, and hence, inject only a TEM<sub>00</sub> mode into the interferometer, the laser light was spatially filtered by means of a mode cleaner cavity [109]. The cavity was stabilised on the laser frequency by a Pound-Drever-Hall scheme [110]: a phase modulation of 12.14 MHz was imprinted on the laser beam by an electro-optic modulator (EOM). The light in reflection of the mode cleaner cavity was detected with a photo detector, resonant at 12.14 MHz, and demodulated with the modulation frequency. The result error-signal was low pass filtered and used for actuation of the cavity length by means of a piezo actuated end-mirror. A Faraday-isolator was used to prevent a direct reflection of the interferometer (not shown in Fig 4.11) through the mode cleaner and to the laser. In case of perfect alignment, this beam would be transmitted through the mode cleaner in reverse di-

### 4.3 Influence and suppression of laser noise

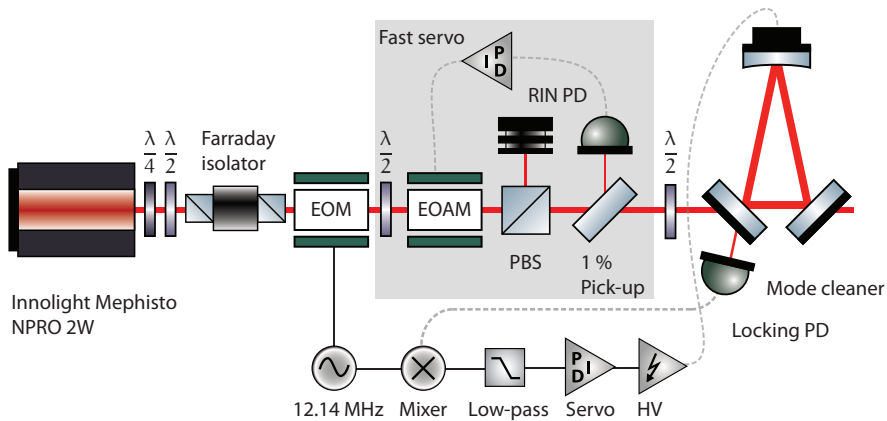


**Figure 4.11:** Schematic of the laser light preparation. Lenses and steering mirrors are not shown for the sake of clarity. After transmission through the mode cleaner, the light was available for injection into the interferometer.

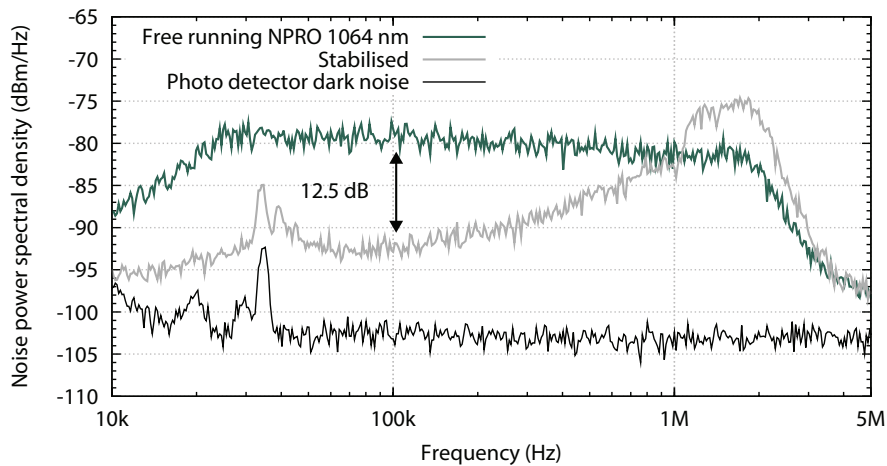


**Figure 4.12:** Exemplary performance of the laser intensity stabilisation. The NPRO technical (amplitude) laser noise is suppressed by 12.5 dB at 100 kHz. The unity-gain frequency is around 1 MHz. Below  $f = 16$  kHz, less noise is detected due to an electronic high-pass filter in the photo detector.

rection. The beam power was stabilised by the active stabilisation scheme described in the previous section and shown on the right side of Fig. 4.10. The performance of the laser intensity stabilisation is depicted in Fig. 4.12. An active noise suppression of 12.5 dB was achieved at frequencies  $f \leq 100$  kHz.

### 4.4 Realisation of the Michelson-Sagnac interferometer

The first version of the experiment was set up in [76, 81] and was used in the beginning of this thesis. Some disadvantages could be identified and were taken into account during the re-design the interferometer. In this section a short summary of identified and solved problems is given and the improved interferometer design is presented.

#### Initial setup and related problems

The Michelson-Sagnac interferometer was build up on a 60 cm diameter, 2 cm thick baseplate made of stainless steel. The baseplate itself was rigidly fixed to the vacuum tank by three posts of stainless steel, sized 30 cm with a 3 cm radius. The main problems identified with this setup were

- Loss of interferometer alignment in vacuum. The rigid connection exposed the interferometer to deformation and bending of the vacuum tank during evacuating the system. The misalignment could only be compensated partially by remote control of central optics.
- The rigid connection also allowed undesired introduction of acoustic coupling. All pumps had to be shut down and a quiet laboratory was mandatory to obtain useful output spectra.
- Disadvantageous mechanical resonances of the interferometer baseplate. The output spectrum contained beat signals around the membrane resonance frequency, separated by 400 kHz and 1 kHz as depicted in Fig. 4.13. These frequencies coincided with mechanical resonances of the baseplate and the posts underneath.

## 4.4 Realisation of the Michelson-Sagnac interferometer

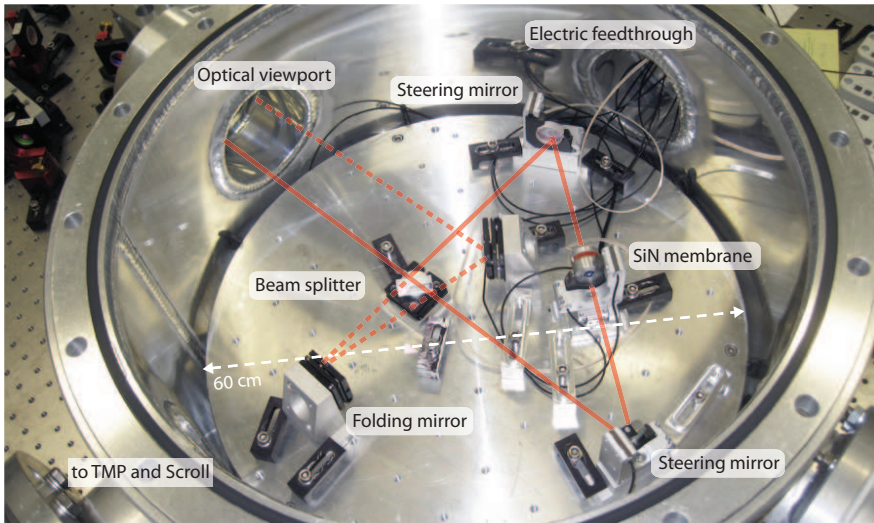


**Figure 4.13:** Initial interferometer inside the vacuum tank. The incident laser beam is depicted as red line, the interferometer output beam is depicted as red, dashed line.

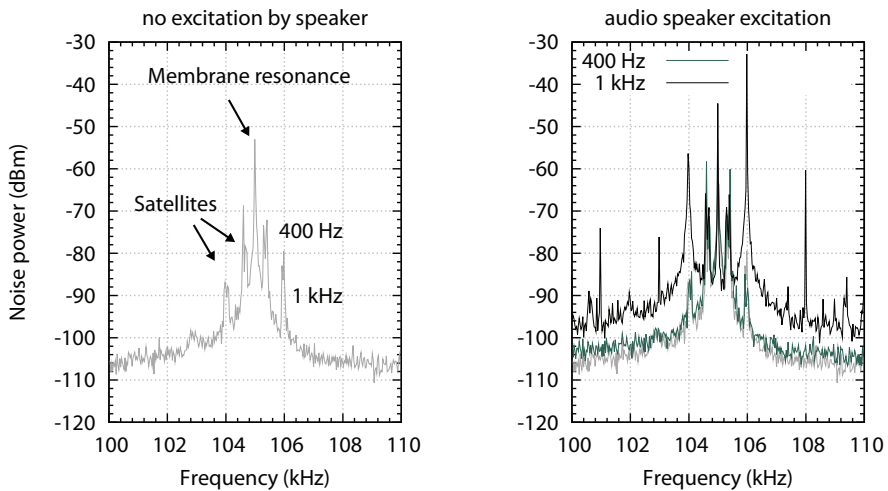


**Figure 4.14:** Left: Typical output power spectrum prior to interferometer isolation. The membrane fundamental mechanical resonance is accompanied by a set of two symmetric peaks with a beat frequency of 400 Hz and 1 kHz. Right: external excitation by an audio speaker with closed and evacuated vacuum chamber.

## 4 Michelson-Sagnac interferometer

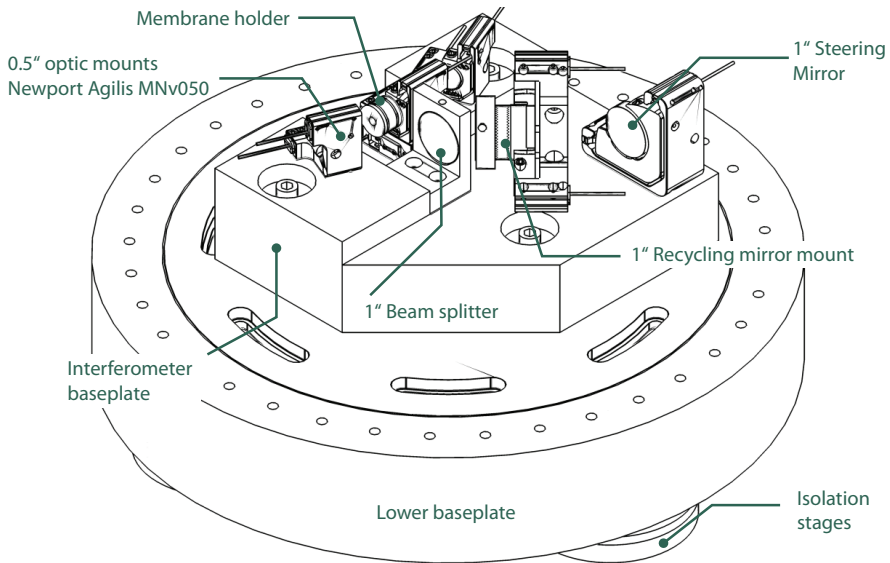


**Figure 4.15:** CAD Design for the Michelson-Sagnac interferometer. It consists of three double-stage isolation footers. On top of these, a heavy plate ensures sufficient weight to push in the viton material. The baseplate itself is then mounted on a 6 cm thick baseplate made out of stainless steel.

### 4.4.1 Interferometer design

The new interferometer design had to fulfil several requirements. First, the interferometer should have a reduced size. An interferometer arm length of less than 10 cm was aimed for. A compact design was expected to exhibit a higher tolerance against small misalignments of the central optics due to reduced leverage. Furthermore, in case of signal-recycling (compare chapter 5) a smaller interferometer results in a larger free spectral range, and thereby bigger optical linewidth with same recycling gain. The interferometer baseplate was required to be as firm as possible. Moreover, it should not be rigidly connected to the vacuum tank. Remote control for the central optics (except beam splitter) was required to maximize the interferometer contrast under vacuum conditions.

During a supervised masters thesis [111], the interferometer was re-designed according to these requirements. A schematic of the revised interferometer is depicted in Fig. 4.15

### 4.4.2 Vibration isolation

The new interferometer was built on a four-level vertical isolation system, consisting of two individual base plates. The isolation in this case was not achieved by suspending the construction with wire pendulums, but by connecting separate stages by compressed, ductile fluororubber *Viton*. Each connection thus acted as spring-mass damper, with resonance frequency  $\omega_{\text{res}}^2 = D/m$ , where  $m$  is the suspended mass, and  $D$  the oscillator spring constant  $D = EA/L$ . Here,  $E$  is the materials Young's modulus, which was determined to  $E \approx 5.8 \text{ N/mm}^2$  [111].  $A$  and  $L$  are the compressed *Viton* surface area and thickness, respectively. The system enhances resonant excitations, but suppresses excitations at frequencies  $\omega_{\text{exc}} > \sqrt{2}\omega_{\text{res}}$  (compare Fig. 3.1). A more detailed description about the isolation can be found in [111]. The interferometer base plate consisted of a  $12 \times 17 \times 3 \text{ cm}^3$  sized block of aluminium and was placed on top of a second base plate. Their combined mass was  $m = 12.4 \text{ kg}$ . Both were connected via compressed *Viton* rings. The lower baseplate was stacked on top of three damping footers (third isolation stage), which themselves were placed on thin *Viton* discs (lowest, fourth isolation stage).

The connection between the three damping footers and lower base plate was given by *Viton* cylinders of 7 mm diameter, and a height of 5 mm. These cylinders were compressed by the heavy mass of the above base plates. The resulting eigenfrequency was  $\omega_0/(2\pi) \approx 100 \text{ Hz}$ . Such that an isolating effect is expected at for frequencies  $f > 140 \text{ Hz}$  for this particular isolation stage.

For sufficient pressure on the *Viton* between the two base plates and in the footers, additional force was applied by auxiliary screws. To avoid a rigid connection by the screws, their connection to the individual stage was buffered with *Viton* rings (in case of the base plates) and viton cylinders in the footers, respectively.

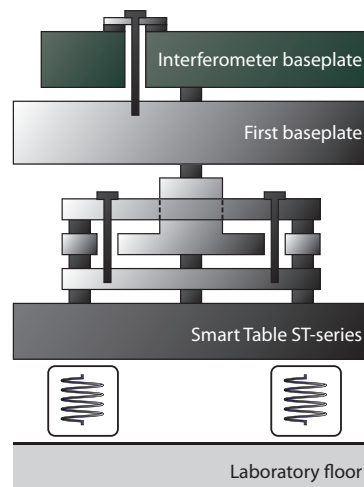


**Figure 4.16:** A schematic of the passive isolation against acoustics and seimics. The isolation has been developed during a masters thesis [111]

## 4 Michelson-Sagnac interferometer

---

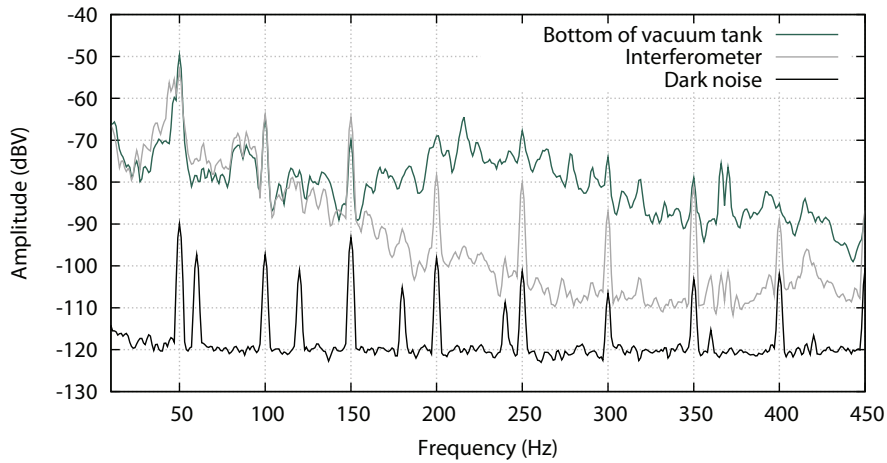


**Figure 4.17:** Seismometer measurement on top of the interferometer baseplate. The measurement shows that above 140 Hz the detected signal is significantly reduced.

To measure the performance of the isolation, seismometer measurements were carried out on the optical table and compared to measurements on top of the interferometer baseplate. The device used was a *Model L-4 Seismometer* by *Mark Products* with a measurement range of  $< 400$  Hz. The result for the isolation in  $z$  (vertical) direction is depicted in Fig. 4.17. The measured signal is reduced for frequencies above 140 Hz by more than 30 dB, the electronic dark noise of the measurement is depicted as black trace. For low frequencies, no suppression was expected.



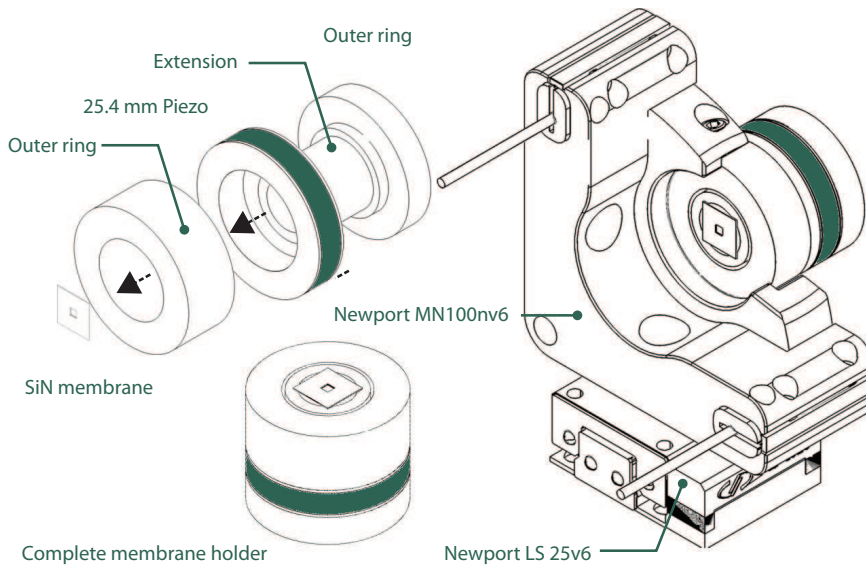


**Figure 4.18:** Schematic of the membrane holder. The holder consists of one inner and one outer ring, which are glued to both sides of a 25.4 mm ring piezo. The membrane is glued to the inner ring. The outer ring was fixed into a remote controllable positioner later. The assembled membrane holder is depicted on the right side of the figure.

### 4.4.3 Membrane holding

To actuate the microscopic position of the membrane along the beam path, the membrane was glued to a ring piezo previous to this work [81]. It turned out that a direct, rigid connection between membrane and piezo led to stress induced modification of the membrane resonance frequency when a high-voltage was applied to the piezo, because a piezo is shortened in the plane perpendicular to the direction of its extension. Thus, the membrane was holdered, separating the piezo actuator and the membrane spatially, as suggested in [81]. The membrane holder is depicted in Fig. 4.18. It consisted of two drilled inner and outer cylinders, which were glued on two different sides of a 25.4 mm ring piezo. The membrane was glued to a hollow extension of the inner cylinder, which was driven through both the piezo and the outer cylinder.

The outer cylinder was fixed within a remote controllable *Newport* [112] positioner, such that the piezo moved only the inner cylinder when extending and the membrane thereby.

## 4 Michelson-Sagnac interferometer

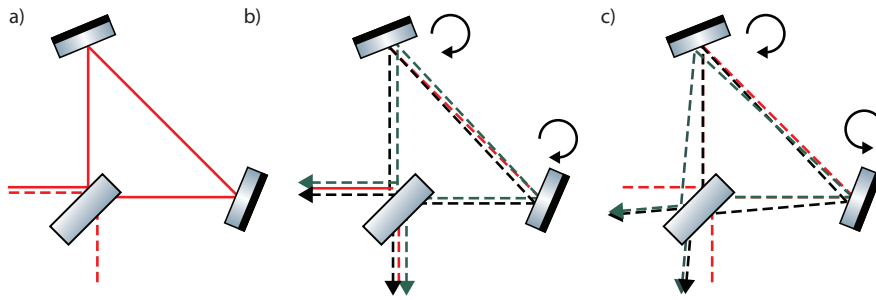


**Figure 4.19:** Exemplary situations during the Sagnac interferometer alignment. a) Ideal situation: dark output, incident and reflected beam are folded. b) If both steering mirrors are rotated in the same direction, this will result in two parallel beams inside and outside the interferometer. c) The steering mirrors are rotated by the same angle as in b), but with different orientations. This can result in a dark output, but incident and reflected beam are pointing in different directions.

### 4.4.4 Interferometer alignment

This section addresses the Michelson-Sagnac interferometer alignment procedure, as it is crucial for a potential cavity arrangement. The setup requires two iterative alignment steps: first, the internal alignment of the Sagnac interferometer is completed (Step 1). Second, the external (lateral) mode matching can be done.

**Step 1: Sagnac alignment** The laser light is spatially filtered by a mode cleaner cavity and is incident on a balanced beam splitter under  $45^\circ$ . After confirming that the beam splitter does not alter the vertical beam direction, the steering mirrors are installed, giving rise to two counter propagating beams and the Sagnac interferometer topology. A CCD camera in the interferometer output can be used to identify misalignment of these mirrors. Fig. 4.19 depicts exemplary situations during the initial setup of the Sagnac interferometer. It illustrates how both steering mirrors are used to overlap both beams. Step 1 is completed if destructive interference in the output port is established, and both, incident and reflected beam are overlapping at every point along their path.

**Step 2: Lateral mode matching** Step 1 guarantees that internal degrees of freedom are set correctly. In the second step, the lateral beam waist must coincide with the later membrane position. This can be checked by verifying that the interferometer folds

## 4.4 Realisation of the Michelson-Sagnac interferometer

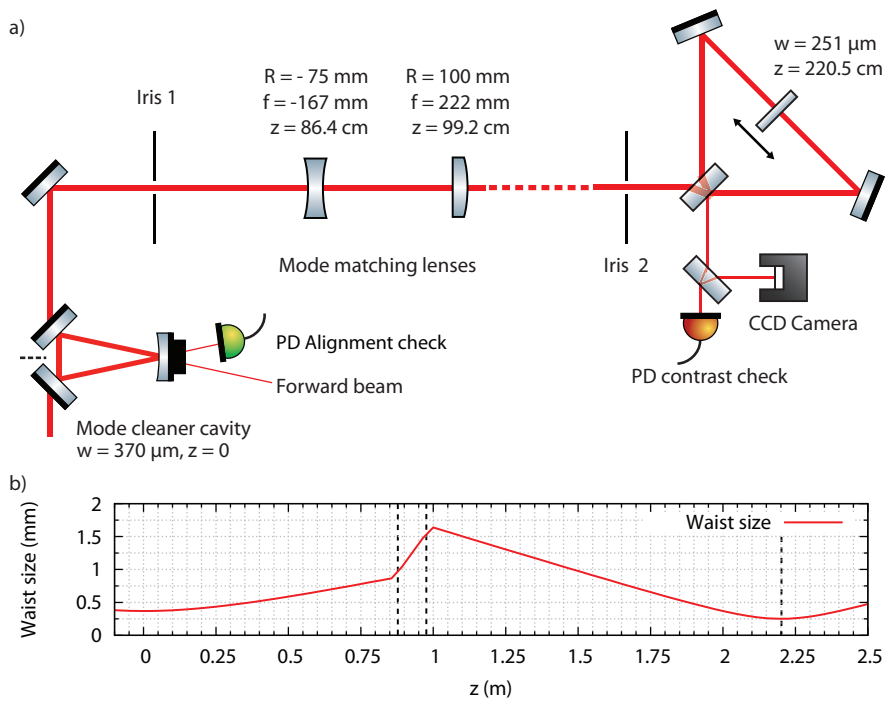


**Figure 4.20:** a) Alignment setup for the Michelson-Sagnac interferometer. Two iris apertures were used for coarse steering of the Sagnac steering mirrors. A mode cleaner cavity served as alignment reference for all beam parameters such as waist position, waist size and beam displacement. b) Waist size as function of distance  $z$  from the initial waist of the mode cleaner cavity  $\omega = 370 \mu\text{m}$ . Lens positions are indicated as dashed, black lines.

the incident beam, such that incident and reflected beam share the same waist position and size. Since the interferometer contrast (degree of destructive interference) is just a coarse indicator. An auxiliary check is provided by the initial mode cleaner cavity: if the reflected beam is already matched to the incident beam (as described in Step 1), a fraction of the reflected light will enter the mode cleaner cavity (which is kept resonant at all time). It can be maximised by shifting the mode matching lenses along the path of the beam. It will be maximal, when the beam is perfectly folded back. The initial positions of the required lenses can approximately be calculated with the software *JamMT* [113].

Once the internal degrees of alignment are fixed, the membrane has to be hit by the beam when being placed inside the interferometer. Since

## 4 Michelson-Sagnac interferometer

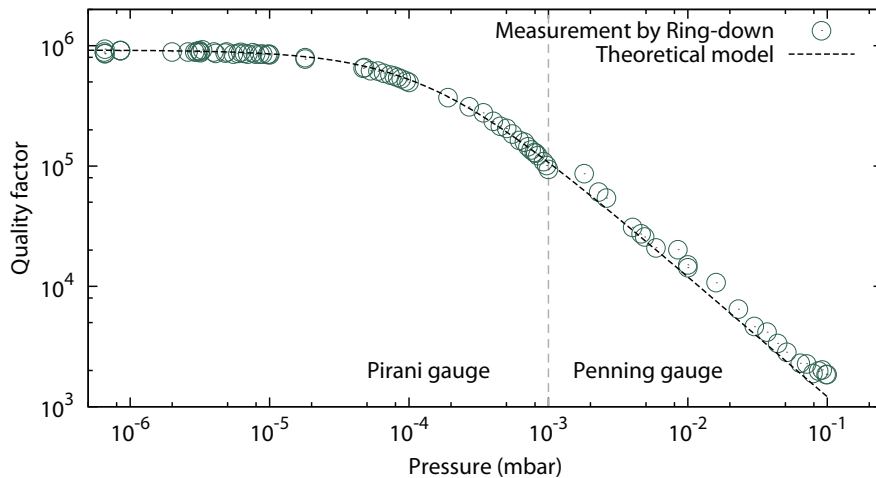


**Figure 4.21:** Measurement of the mechanical quality factor  $Q$  of a membranes fundamental oscillation mode for different vacuum qualities, as shown in [76]. Only for pressures  $P \leq 4 \cdot 10^{-6}$  mbar the  $Q$ -factor is not limited by residual gas damping.

no membrane positioning in the plane perpendicular to the beam is possible, the incident beam has to be translated by an external set of steering mirrors. This is possible since the Sagnac interferometer is indifferent to pure displacement of the incident beam (as long as no beam clipping occurs). The additional degrees of freedom of the membrane (pitch, yaw) can cause misalignment of the Michelson mode with respect to the Sagnac mode, such that a fine alignment of the membrane is required. The effect of a misalignment of the membrane is depicted on the right side of Fig. 6.14.

### 4.4.5 Vacuum requirements

The mechanical quality factor  $Q$  of the high-stress silicon nitride membrane oscillation modes is around  $10^6$ , but can be dramatically reduced if the oscillation is damped. Major damping is caused by interaction with gas molecules. To not limit the  $Q$ -factor, a vacuum environment for the system is necessary. Fig. 4.21 illustrates the dependence of mechanical quality factor and environmental pressure used in the experiment. An analytical relation between residual gas pressure and mechanical quality factor of the oscillator is given in [114, 115].

$$Q = \left(\frac{\pi}{2}\right)^{\frac{3}{2}} \rho H f_0 \sqrt{\frac{RT}{M_{\text{mol}} p}} \quad , \quad (4.40)$$

where  $\rho$  is the specific mass of the membrane,  $H$  denotes the membrane thickness,  $f_0$  is the resonance frequency,  $R$  is the universal gas constant,  $T$  is the absolute temperature,  $M_{\text{mol}}$  is the molar weight of the damping gas (in this case nitrogen) and finally,  $p$  is the gas pressure.

The pressure in the vacuum tank had to be below  $4 \cdot 10^{-6}$  mbar to not limit the mechanical quality factor fundamental resonance. In the experiment, this was achieved by evacuating the vacuum chamber by a two-stage pump system, set up during a master thesis [81]. An oil-free scroll pump pre-evacuated the system to  $2 \cdot 10^{-2}$  mbar. A *Varian* TPH520M turbo molecular pump was used in the second stage. While running, this pump provided a pressure of  $3 \cdot 10^{-7}$  mbar. After several hours of pumping (when residual hydrogen was boiled off the surfaces), the pressure was stabilised at this value by a *Varian* ion-getter pump 'VacIon plus 20'. To take data, a valve between the vacuum chamber and the TMP was closed and both mechanical pumps were be switched off. The pressure inside the vacuum system did not exceed  $1.4 \cdot 10^{-6}$  mbar, a value well below the requirements and could be maintained at  $0.7 \cdot 10^{-7}$  mbar after longer pumping periods.

### 4.4.6 Remote alignment

Evacuating the interferometer chamber caused a significantly reduced interferometer contrast in the initial version of the experiment. The misalignment was found to occur within the interferometer. Hence, without remote control over the alignment of the interferometer's optical components, it was not possible to be corrected the misalignment without a disassembly of the system (and thereby opening the tank again). Hence, all mirrors and the membrane holder were mounted into vacuum compatible, remote controllable positioners *Newport Agilis AG-MN50NV6* [112] to allow for realignment with the vacuum chamber closed. The positioners are piezo steppers, with no high-voltage input. Thus, they were not introducing additional position noise due to a noisy output of a high-voltage amplifier. Figure 4.23 depicts the assembled interferometer. An additional linear stage *Agilis AG-LS25V6* was installed underneath the membrane holder. The beam path is shown as red line, the interferometer output direction is

## 4 Michelson-Sagnac interferometer

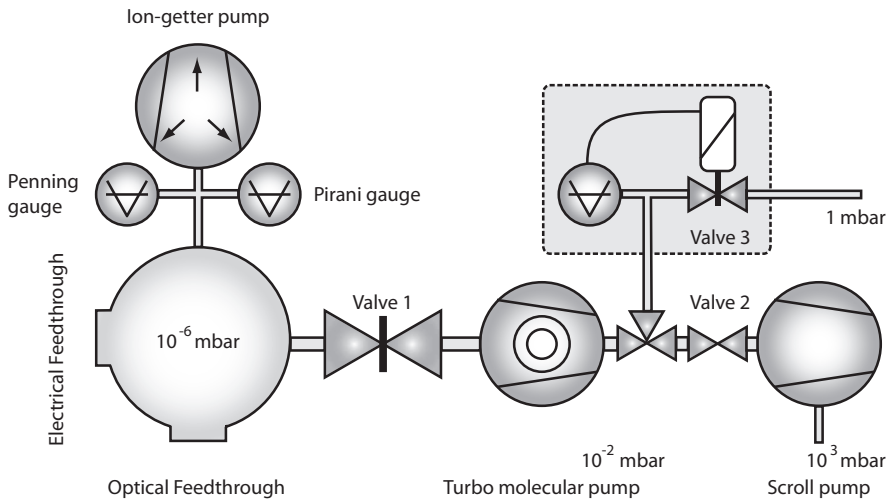


**Figure 4.22:** Vacuum setup, [81]. A turbo-molecular pump (TMP) provides a vacuum with  $P_{\text{vac}} < 10^{-6}$  mbar. The high-pressure side of the TMP is pumped via a scroll pump. For measurements, the valves 1 and 2 were closed, and all pumps except for the ion-getter pump were switched off.

shown as red, dashed line.

Full remote access allowed to restore the high initial interference contrast of  $C = 99.7\%$  in the evacuated vacuum tank. Thereby, the technical laser noise in the readout could be suppressed significantly. A measured fringe of the interferometer is presented in Fig. 4.24.

### 4.5 Interferometer calibration

This section addresses the calibration of the interferometer. The output is analysed in form of a power spectrum, which has to be converted to an equivalent displacement spectrum. Different calibration methods can be used to achieve this.

#### 4.5.1 Calibration via the interferometer fringe

In case of DC readout with one single photo detector in transmission of the interferometer, the measured output power spectra can be calibrated via the interferometer fringe. Equation (4.11) relates the interferometer output power (and output power derivative) to the differential microscopic membrane position. To calibrate a spectrum, a saw tooth voltage  $U(t)$  is applied to the membrane piezo high-voltage

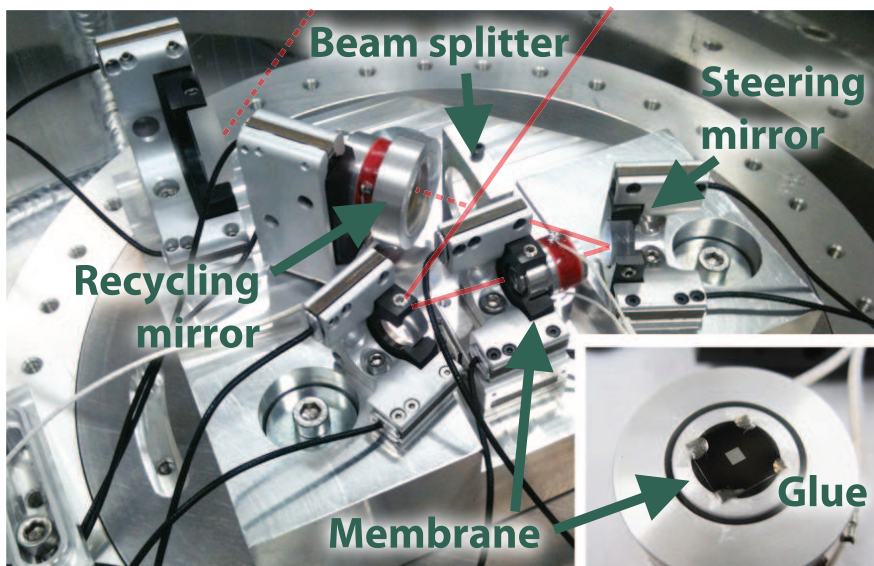


**Figure 4.23:** A photograph of the redesigned Michelson-Sagnac interferometer. Essential components are labeled. The membrane is mounted into a *Newport Agilis AG-M50NV6* mount, which in turn is attached on top of a linear piezo stepper stage *Agilis AG-LS25V6*. The inset shows a closer view to a  $0.5 \times 0.5 \text{ cm}^2$  membrane, which is glued with a small drop of *VacSeal* in each corner.

amplifier. The membrane position and thereby interferometer tuning is 'scanned' periodically in time. Due to the non-linearity of the piezo, the actual membrane displacement can be inferred from the applied voltage by fitting the analytical expression (4.11) with a polynomial expression for the displacement  $x(\mathcal{U}(t))$  to the measured fringe. Here one makes use of the fact that maximum output power occurs for equidistant membrane positions and are independent of the beam splitter ratio.

The rescaled theoretical curve is derived with respect to the membrane position, yielding a ratio of  $\text{V}/\text{nm}$  displacement for each interferometer tuning. Vice versa, the displacement per detected voltage in  $\text{nm}/\text{V}$  is known for each membrane position (which is denoted for each measurement).

#### 4.5.2 Obtaining the membrane displacement spectrum

To obtain the linear displacement spectral density of the membrane, the AC output of the photo detector is fed into a spectrum analyzer. Calibration has to account for the electronic transfer function of the

## 4 Michelson-Sagnac interferometer

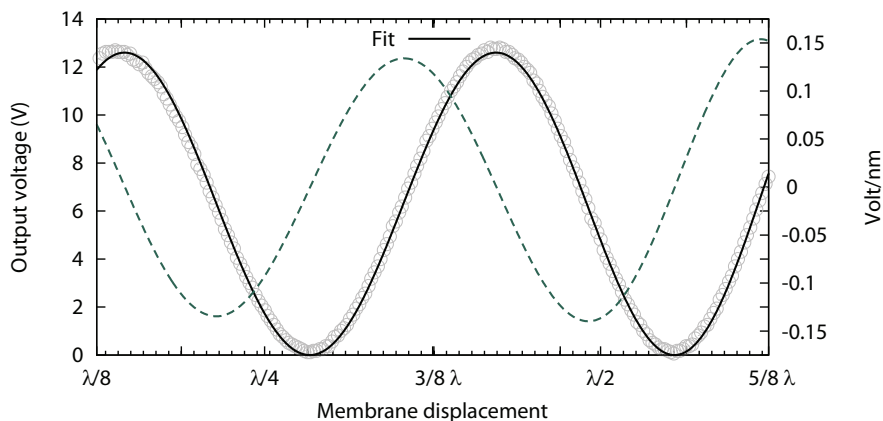


**Figure 4.24:** Interferometer output signal detected with a single photo diode (grey dots). The theoretical output fringe (black solid line) was rescaled to account for piezo non-linearities. The dashed green line depicts the derivative of the rescaled theoretical output fringe, relating the membrane displacement to change of detected output voltage for each membrane position

detector. In case of the spectra presented here, the AC path featured two first-order high pass filters with corner frequencies  $f_{0,i}$  and a proportional electronic gain, such that the ratio  $G$  between DC and AC output voltage for each frequency  $f$  was given by

$$G(f) = \frac{U_{AC}}{U_{DC}} = \text{Gain} \cdot \frac{\frac{f}{f_{0,1}}}{\sqrt{1 + (\frac{f}{f_{0,1}})^2}} \frac{\frac{f}{f_{0,2}}}{\sqrt{1 + (\frac{f}{f_{0,2}})^2}}, \quad (4.41)$$

where  $\text{Gain} = 23.4$ ,  $f_{0,1} = 16.67$  kHz,  $f_{0,2} = 1.52$  kHz which results in  $G = 23.04$  at  $f = 100$  kHz. The spectrum analyser was set to measure dBm. In this case, the input power level is compared to 1 mW with an input impedance of  $R = 50 \Omega$  of the spectrum analyser.

$$\begin{aligned} \frac{L_p}{\text{dBm}} &= 10 \log \left( \frac{P}{1 \text{ mW}} \right), \quad P = \frac{U^2}{R} \\ \Leftrightarrow U &= (R \cdot 1 \text{ mW})^{1/2} \cdot 10^{L_p / 20 \text{ dBm}} \end{aligned} \quad (4.42)$$

Here,  $L_p$  is the noise level in dBm/Hz. For another measurement resolution bandwidth (RBW),  $L_p$  is to be rescaled  $L_p = L_p - 10 \log \text{RBW}$ .



### 4.5.3 Calibration using a marker peak

To ease the calibration procedure and to provide a calibration method with no need to scan the interferometer fringe, a calibrated via a defined displacement marker peak was introduced. Therefore, a defined excitation of the oscillator was generated by applying a sinusoidal frequency of  $f = 128$  kHz to the membrane piezo actuator. Frequency, amplitude, high voltage amplifier and piezo were untouched during all following measurements. The displacement of the marker peak was determined from displacement spectra which were calibrated with the fringe calibration method. The peak displacement was calibrated for multiple dark- and mid-fringes of the interferometer, and was found to be stable at  $0.9 \cdot 10^{-12}$  m, with no perceivable variation of displacement caused by a piezo voltage offset.

## 4.6 Achieved displacement sensitivity

The interferometer output was analysed with a single photo detector as well as with a balanced homodyne detection.

### 4.6.1 Readout with a single photo detector

As explained in the previous chapter, the ratio of technical laser noise to optical shot noise depends on the detected optical power (compare Eq. (4.39)). Thus, the displacement measurement will be shot noise limited for low optical input powers, but with reduced sensitivity. The first goal of the this thesis was to achieve a shot noise limited read out for high optical input powers, as the prior setup was limited by technical laser noise for input powers  $P_{\text{in}} > 50 \mu\text{W}$ , with a displacement sensitivity limited to  $3 \cdot 10^{-15} \text{m}/\sqrt{\text{Hz}}$ .

Figure 4.25 shows a calibrated interferometer output spectrum with refined interferometer contrast  $C \approx 99.7\%$  and laser amplitude stabilisation. The sensitivity is limited by technical laser noise and optical shot noise (dashed line). The achieved displacement sensitivity around the fundamental mechanical resonance frequency was  $3.6 \cdot 10^{-16} \text{m}/\sqrt{\text{Hz}}$  for an optical input power of  $P_{\text{in}} = 100 \text{mW}$ . The calculated shot noise level is plotted as grey, dashed line, and is dominant off resonance, but laser and electronic dark-noise are not negligible. A calibrated marker at  $f = 128$  kHz was introduced by applying a modulation to the membrane piezo actuator. Moreover, the obtained

## 4 Michelson-Sagnac interferometer

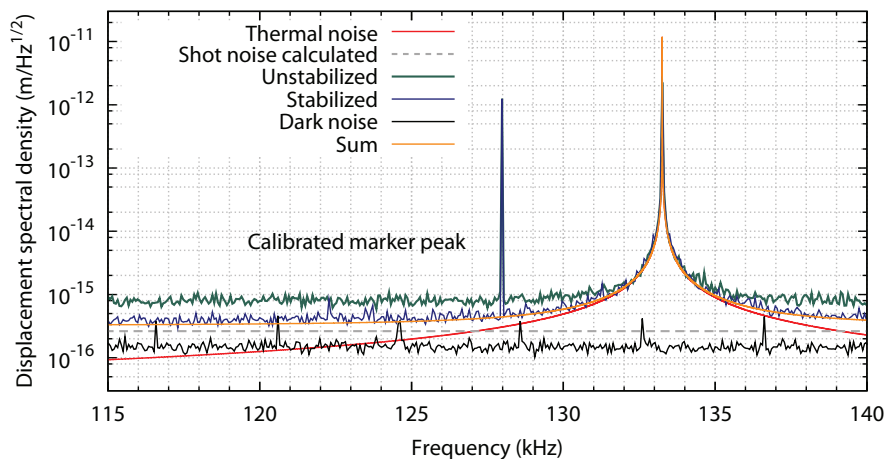


**Figure 4.25:** Membrane displacement spectrum around the fundamental mode. Off resonance, the spectrum is limited by laser intensity noise. Shot noise as well as detector dark noise are below. At the very resonance, the spectrum is dominated by the thermal noise (dashed red line) which here was calculated for  $Q = 5.8 \cdot 10^6$  and a temperature of  $T = 300$  K. Off resonance the highest displacement sensitivity is  $3.6 \cdot 10^{-16} \text{ m}/\sqrt{\text{Hz}}$ . This measurement was taken before the final displacement of the marker was fixed, such that the marker peak here corresponds to  $1.25 \cdot 10^{-12} \text{ m}/\sqrt{\text{Hz}}$ .

spectra did not contain satellite peaks. This was attributed to the performance of the vibration isolation described in Sec. 4.4.2.

Despite its simplicity, the DC readout has three drawbacks. First, it only allows for measuring the amplitude quadrature of the output field. Second, when obtaining the output power spectrum, it is not clear whether or not the spectrum is limited by shot noise. This can be checked by measuring the output spectrum at high frequencies  $f > 10$  MHz and comparing the relative power noise levels. This measurement relies on a flat (or precisely known) transfer function of the photo detector, however. The shot noise equivalent displacement noise can also be calculated, according to Eq. (4.24), but this method requires knowledge about the optical loss during detection.

Third, the measurements have to be taken off dark-fringe to provide some local oscillator power. Due to the finite contrast  $C$  (compare Fig. 4.6) the offset from interferometer dark-fringe must exceed a certain value. Thereby technical laser amplitude noise couples into the measurement. Moreover, this reduces the interferometer amplitude reflectivity  $r_{\text{ifo}}$ , which is wanted to be as high as possible for the

## 4.6 Achieved displacement sensitivity

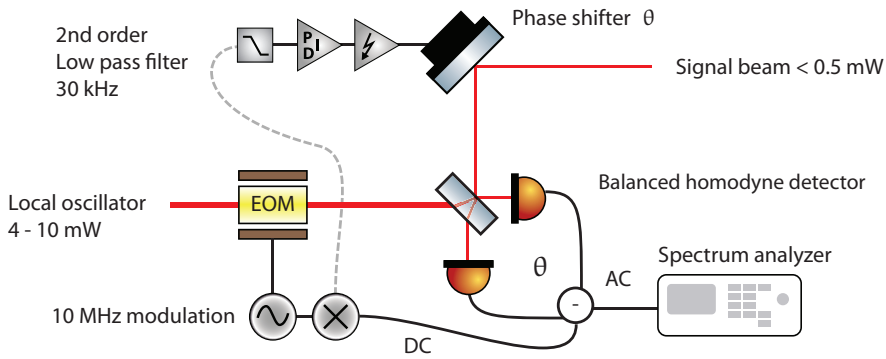


**Figure 4.26:** Locking scheme for the relative phase  $\theta$  (close) to the amplitude quadrature. The interferometer output field (signal beam) and a stronger local oscillator are overlapped on a balanced beam splitter. A phase modulation of 10 MHz was imprinted on the local oscillator beam. The AC filtered, differential output of the homodyne detector was fed into a spectrum analyser, whereas the direct subtraction of both photo currents was demodulated with the modulation signal, providing an error signal for a relative phase of  $\theta = \pi/2$ .

adaption of recycling techniques, see Chap. 5.

### 4.6.2 Balanced homodyne readout

To resolve the above mentioned drawbacks of a DC readout, a balanced homodyne detector was set up and used in the following measurements. The relative phase between local oscillator and signal beam was adjustable by a piezo actuated mirror. A relative phase difference of  $\theta = \pi$  refers to a measurement in the phase quadrature, whereas  $\theta = \pi/2$  corresponds to a measurement in the orthogonal, amplitude quadrature. To observe a particular quadrature of the output field, the relative phase  $\theta$  between the local oscillator and the signal had to be stabilized. For the phase quadrature, the required error signal is directly provided by the DC output of the homodyne detector, as this quadrature is measured at the DC zero transient.

The locking scheme for measuring the amplitude quadrature is depicted in Fig. 4.26. To lock to the amplitude quadrature, the local oscillator was phase modulated with 10 MHz, and the subtracted signal of both homodyne photo detectors was demodulated with the modulation frequency. This is achieved by mixing the signal with an electronic 'copy' of the modulation signal. The resulting signal was low pass filtered and provided an appropriate error signal. This error signal was used to actively stabilise the relative phase  $\theta$  by the

## 4 Michelson-Sagnac interferometer

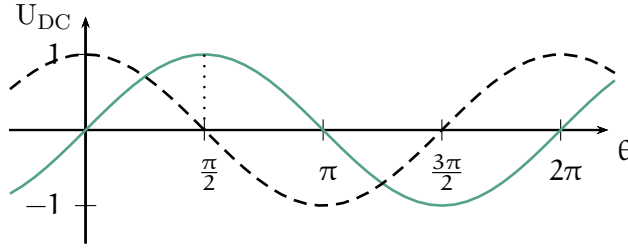


**Figure 4.27:** Homodyne detector DC signal (green) and demodulated error signal (black dashed line) in arbitrary units. The amplitude quadrature refers to a relative phase of  $\theta = \pi/2$ , whereas the phase quadrature is measured at  $\theta = 0 \pmod{\pi}$ .

piezo actuated mirror. The modulation/ demodulation technique is described in section 5.2.1. A calculated error signal is shown in Fig. 4.27. To avoid beam pointing and associated interference reduction because of lever, the actuated mirror was positioned close to the homodyne beam splitter.

The overlap of both optical fields on the homodyne beam splitter exhibits an interference contrast  $C_{\text{homo}}$ , just as in case of the Michelson-Sagnac interferometer. Measuring the maximum and minimum power in each of the beam splitter output ports  $P_{\text{max}}, P_{\text{min}}$ , yields the same expression for  $C$  as given in Eq. (4.31). For equal optical input powers, the contrast can be limited by mode mismatch of the two beams. For the detection efficiency, a non-ideal interference contrast has the same effect as optical loss in the path [67]

$$\text{Power Loss} = C_{\text{homo}}^2 \quad . \quad (4.43)$$

In the experiment, the mode matching achieved a value of 90 %, causing 19 % optical loss. In the absence of squeezing, the loss was found tolerable. Together with a homodyne detector efficiency of about 80 % for the photo diodes in use, an overall read out loss of 35 % was assumed. The loss results in an increased relative shot noise level. Without the loss associated with the detection, the displacement sensitivity would have been better by a factor of  $1/\sqrt{0.65} \approx 1.24$ .

The homodyne detection requires a small coherent amplitude of the signal beam (compare Eq. (2.42)). Scanning the interferometer is thus not possible, as was done in case of DC readout and fringe calibration. The output spectra were thus calibrated by the calibrated marker peak. The resulting output spectra are depicted in Fig. 4.28. All measurements were limited by optical shot noise off

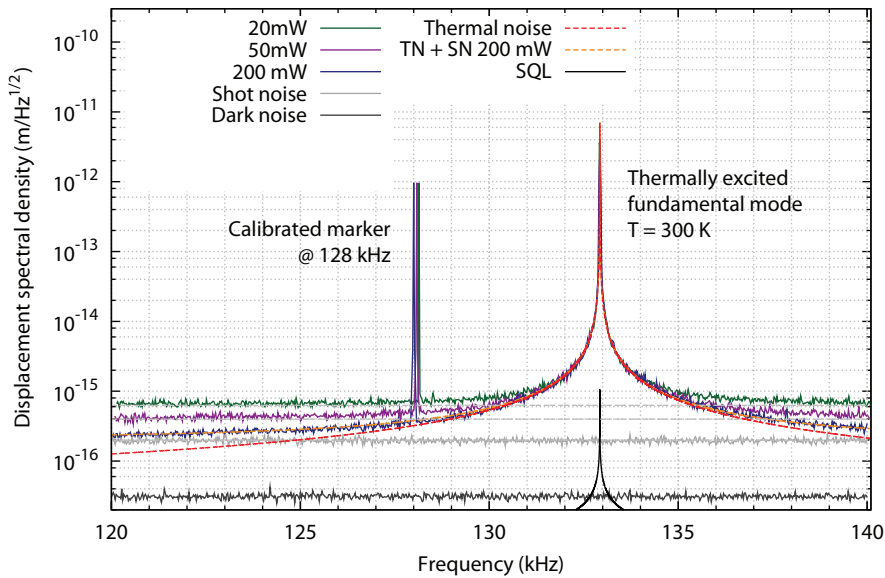


**Figure 4.28:** Calibrated interferometer output spectrum with balanced homodyne detection. A marker at  $f = 128$  kHz of well-known displacement was used to calibrate the spectra for different optical input powers (green, purple and blue traces). The shot noise level for each measurement is plotted in grey (dashed) lines. Each measurement is shot noise limited off thermal resonance. Electronic dark noise is plotted in dark grey. Due to a slight dependence of mechanical resonance frequency to optical input power, the traces were slightly shifted in frequency (about 100 Hz).

resonance. The thermal noise matched the theoretical calculations on resonance for the membrane specifications. A shot noise limited displacement sensitivity of  $1.9 \cdot 10^{-16} \text{ m}/\sqrt{\text{Hz}}$  for an optical input power for  $P_{\text{in}} = 200 \text{ mW}$  was achieved.

Measurements over a broad frequency span demonstrated a shot noise limited displacement measurement for frequencies  $f > 60$  kHz, as can be seen in Fig. 4.29. The measurements were normalized to optical shot noise power level, which was measured by blocking the signal path with a beam dump. To verify the limitation by shot noise, the local oscillator power was attenuated consecutively by a factor of two and four, respectively. The shot noise power level was observed to drop by 3 dB, as expected when halving the local oscillator power.

By a variation of the homodyne readout angle  $\theta$ , it is possible to investigate arbitrary quadratures of the optical field. Thereby it was shown [85] that the oscillator thermal noise is present only in the amplitude quadrature of the interferometer output field. A triangular

## 4 Michelson-Sagnac interferometer

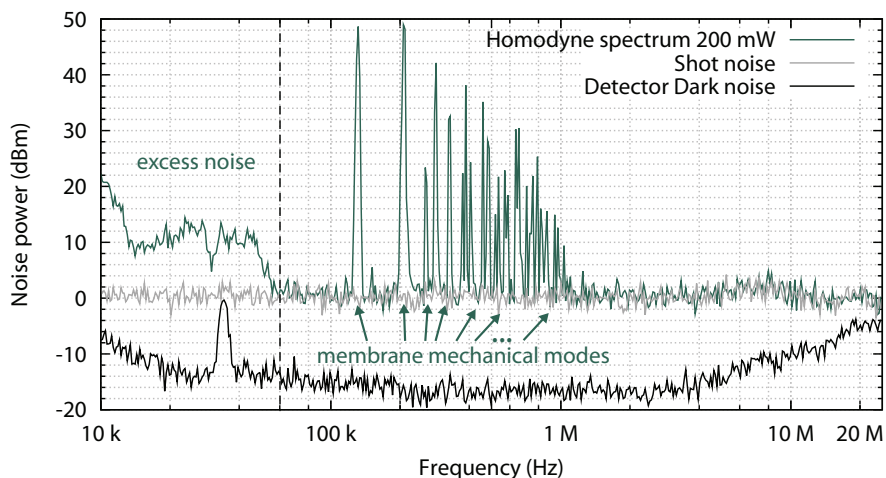


**Figure 4.29:** Balanced homodyne output power spectrum, normalised to the mean optical shot noise level. The spectra are shot noise limited with  $P_{\text{in}} = 200$  mW for frequencies  $f > 60$  kHz. The electronic dark noise clearance is about 15 dB in the relevant frequency range.

voltage was applied to the piezo on the phase shifter mirror and the a spectrum analyser was set to measure with a minimum frequency span at the mechanical resonance frequency. The result is shown in Fig. 4.30. At  $t = 2.08$  s, the detected noise power (shown as green trace) is maximum. This corresponds to a measurement in amplitude quadrature. At  $t \approx 1$  s and  $t \approx 1.5$  s, the measured noise power drops to the shot noise level, which was measured by blocking the interferometer output port, and is shown as grey trace. This corresponds to a measurement in phase quadrature. The electronic dark noise of the measurement is shown as black trace.

The ability to investigate arbitrary quadratures is necessary to perform opto-mechanical entanglement analysis [116] or to detect non-classical properties of the interferometer output light, such as ponderomotive squeezing [117].

### 4.7 Chapter summary

In this chapter, the Michelson-Sagnac interferometer topology was presented, and a detailed explanation about interferometer input and output optical fields was provided. The achievable interferometer sensitivity was investigated under consideration of quantum and classi-

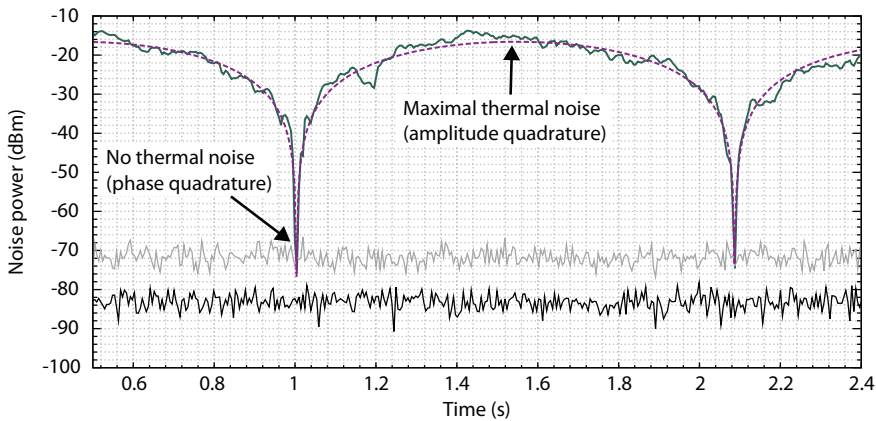


**Figure 4.30:** Measured noise power at the fundamental mechanical resonance frequency of the SiN membrane (green trace). The homodyne read out phase  $\theta$  is periodically modulated by a triangular voltage applied to the phase shifter piezo and thus, is shown as a function of time. In phase quadrature, the measured noise power drops down to the independently measured shot noise level (grey trace). This happened at  $t = 1$  s and  $t = 2.08$  s. In amplitude quadrature ( $t \approx 1.5$  s), the maximum noise power is detected. This corresponds to a measurement in amplitude quadrature. The magenta line shows the theoretical model for vacuum noise in phase quadrature and large, thermal noise in the orthogonal quadrature. Electronic dark noise is shown as black trace. The RBW for this measurement was 10 kHz.

cal noise sources, namely laser intensity and frequency noise as these can not be neglected. An interference contrast of  $C = 99.7\%$  of the Michelson-Sagnac interferometer in high vacuum ( $p = 1.0 \cdot 10^{-6}$  mbar) was achieved, reducing the influence of technical laser noise in the readout. To achieve this high contrast when combining both, Sagnac and Michelson interferometer in the vacuum tank requires a fine alignment, for which a standard procedure could be developed. Technical laser noise was further decreased by means of a realised high-speed laser intensity stabilisation. Next, a balanced homodyne detection scheme was set up, and the interferometer was operated on dark-fringe. For this purpose, a marker peak calibration method was introduced. The balanced homodyne detection suppressed the impact of higher order transversal modes in the read out and provided a shot noise limited displacement sensitivity of  $1.9 \cdot 10^{-16}$  m/ $\sqrt{\text{Hz}}$  for frequencies above 60 kHz. The balanced homodyne detection scheme is necessary to perform a tomographic reconstruction of the interferometer output state of light. A further reduction of the low frequency noise is expected when shielding the detection from stray light, additional

## 4 Michelson-Sagnac interferometer

---

improvement can be expected with reduced optical path lengths, as beam pointing on the detector and the interferometer beam splitter can thus be reduced, due to a reduced lever. The fact that the obtained spectra were limited by thermal and optical shot noise only implies that the interferometer sensitivity can also be increased by injecting a squeezed vacuum state in the interferometer output port.



# 5

## Chapter 5

# Signal-recycled Michelson-Sagnac interferometer

This chapter first provides the basic concept of an optical cavity. Next, the extension of the interferometer by an additional mirror in the Michelson-Sagnac interferometer output port is discussed, with regards to possible benefits such as signal recycling gain. The impact of loss in the cavity is briefly addressed, as a recycling mirror enhances the signal in the output port only under certain circumstances. The chapter also issues the opto-mechanical interactions which are enabled by the recycling mirror and presents a model for the resulting, complex optical spring. In contrast to a linear cavity, the shape of the optical spring is more complex, due to direct modifications of the cavity finesse by the micro-oscillator position. This mechanism is referred to as dissipative coupling [52, 53].

## 5.1 Optical cavity

The simplest case of a linear optical cavity consists of two mirrors. If the cavity is brought to resonance, the input optical field can be resonantly enhanced, as will be shown in the next paragraph. As a result, the arrangement allows for a complete transmission of optical power incident on the initial mirror and to also resonantly enhance signal side bands generated inside the cavity (signal-recycling). Here, a short description of the optical cavity and requirements for the latter situation are given. The following calculations make use of the amplitude  $a_{\text{in}}$  incident on mirror one with amplitude reflectivity and transmissivity of  $r_1, t_1$ . The second mirror is separated by an optical

## 5 Signal-recycled Michelson-Sagnac interferometer

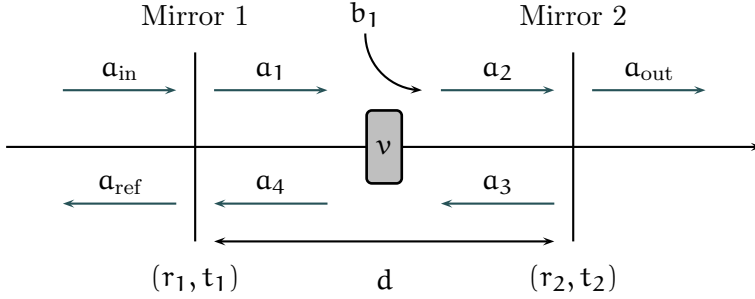


**Figure 5.1:** Schematic illustration of a two mirror cavity [118]. The optical axis is depicted as the black arrow, optical fields are depicted as green arrows. Light is assumed to be incident from the left side only. The mirrors exhibit amplitude reflection and transmission coefficients  $r_1, t_1$  and  $r_2, t_2$  respectively.  $v \leq 1$  corresponds to loss within the cavity

distance  $d$  with respect to the first mirror, and exhibits amplitude reflectivity and transmissivity  $r_2, t_2$ . In a lossless scenario, the coefficients fulfill  $r_i^2 + t_i^2 = 1$  due to energy conservation.

The fields inside the cavity can be calculated following [118, 119]. A phase flip of  $\pi/2$  is assumed for every transmission. Loss inside the cavity can be modelled with an additional factor ( $v \leq 1$ ). The resulting set of equations is

$$\begin{aligned} a_1 &= it_1 a_{\text{in}} + r_1 a_4 \quad , \\ a_2 &= v e^{-ikd} (a_1 + b_1) \quad , \\ a_3 &= r_2 a_2 \quad , \\ a_4 &= v a_3 e^{-ikd} \quad , \\ a_{\text{ref}} &= r_1 a_{\text{in}} + it_1 a_4 \quad , \end{aligned} \tag{5.1}$$

$$a_{\text{out}} = it_2 a_2 \quad . \tag{5.2}$$

Here,  $k$  is the optical wave vector  $k = 2\pi/\lambda$  with  $\lambda$  being the optical wavelength. An input signal  $b_1$  can be used to compute the cavity transfer function [119], for signals generated inside the cavity. It will be set to zero here  $b_1 = 0$ . Then, by solving the above set of equations for  $a_4$  and  $a_2$  results in

$$a_4 = a_{\text{in}} \frac{iv^2 r_2 t_1 e^{-ik2d}}{1 - v^2 r_1 r_2 e^{-ik2d}} \quad , \quad a_2 = a_{\text{in}} \frac{iv t_1 e^{-ikd}}{1 - v^2 r_1 r_2 e^{-ik2d}} \quad . \tag{5.3}$$

Inserting these results back into Eq. (5.1),(5.2) and assuming a lossless case ( $\nu = 1$ ) yields

$$\mathbf{a}_{\text{ref}} = \mathbf{a}_{\text{in}} \left( \frac{r_1 - r_2(r_1^2 + t_1^2)e^{-ik2d}}{1 - r_1 r_2 e^{-ik2d}} \right) , \quad (5.4)$$

$$\mathbf{a}_{\text{out}} = \mathbf{a}_{\text{in}} \left( \frac{-t_1 t_2 e^{-ikd}}{1 - r_1 r_2 e^{-ik2d}} \right) . \quad (5.5)$$

The reflected and transmitted field fulfil  $|\mathbf{a}_{\text{out}}|^2 + |\mathbf{a}_{\text{refl}}|^2 = 1 \forall d$ . The cavity resonance condition is

$$e^{-ik2d} = 1 . \quad (5.6)$$

If Eq. 5.6 is fulfilled, and for equal reflectivities  $r_1 = r_2$ , the cavity is called *impedance* matched. The equations (5.5) then yield

$$\mathbf{a}_{\text{ref}} = 0, \mathbf{a}_{\text{out}} = \mathbf{a}_{\text{in}} . \quad (5.7)$$

The cavity exhibits multiple resonant lengths  $d_r$ ,

$$e^{-ik2d_r} = 1 \Leftrightarrow kd_r = N\pi , \quad (5.8)$$

with  $N$  being an integer. It is often times useful to separate the cavity length  $d$  into a macroscopic length  $L$  and a microscopic length  $d_r$ . With  $k = 2\pi f/c$  and the definition  $\text{FSR} = c/(2d)$ . Eq. (5.8) can be rewritten as

$$N\pi = \frac{\pi f_r}{\text{FSR}} , \quad (5.9)$$

such that consecutive resonances are separated by the free-spectral range (FSR),  $\Delta f_r = \text{FSR}$ . The FSR only depends on the cavity's optical length  $d$ , not on the reflectivities  $r_i$  of the mirrors.

The second characteristic quantity of an optical cavity is its finesse  $\mathcal{F}$ , which is defined in terms of the full-width at half-maximum (FWHM) power transmission of the cavity.

$$\text{FWHM} = \frac{2\text{FSR}}{\pi} \arcsin \left( \frac{1 - r_1 r_2}{2\sqrt{r_1 r_2}} \right) . \quad (5.10)$$

With this definition, the cavity finesse  $\mathcal{F}$  is defined as

$$\mathcal{F} = \frac{\text{FSR}}{\text{FWHM}} . \quad (5.11)$$

## 5 Signal-recycled Michelson-Sagnac interferometer

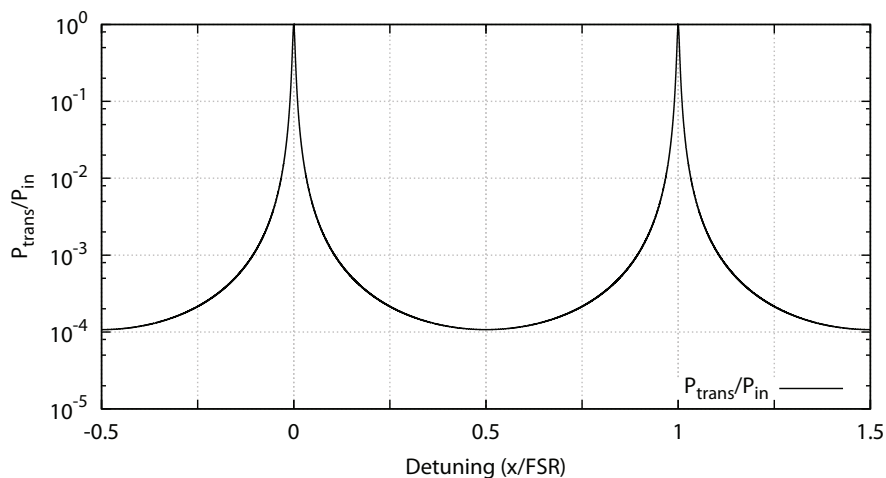


**Figure 5.2:** Cavity resonance peaks for an impedance-matched cavity  $r_1 = r_2$ . On cavity resonance, all incident power is transmitted through the cavity. The distance between two resonances is given by the cavity free spectral range (FSR).

### Cavity offset from a resonance

For small frequencies ( $f \ll \text{FSR}$ ), the cavity acts as an optical low-pass filter [54] with corner frequency  $f_c$ . This can be seen from the Taylor expansion of the exponential function in denominator of equation (5.5)

$$\frac{1}{1 - r_1 r_2 e^{-ik2d}} \approx \frac{1/(1 - r_1 r_2)}{1 + if/f_c}, \quad f_c = \frac{\text{FWHM}}{2}. \quad (5.12)$$

Inserting Eq. (5.10) into Eq. (5.12) yields

$$f_c = \frac{c}{2\pi d} \arcsin\left(\frac{1 - r_1 r_2}{\sqrt{r_1 r_2}}\right) \approx \frac{1 - r_2}{2\pi d}, \quad (5.13)$$

with the last approximation being valid for small arguments  $x$ , when  $\arcsin(x) \approx x$ . This is however ensured by the fact that  $r_1, r_2 \approx 1$ . A comparison of the exact cavity solution and the low-pass approximation is depicted in Fig. 4.9. The DC enhancement ( $f \rightarrow 0$ ) is thus given by  $1/(1 - r_1 r_2)$ .

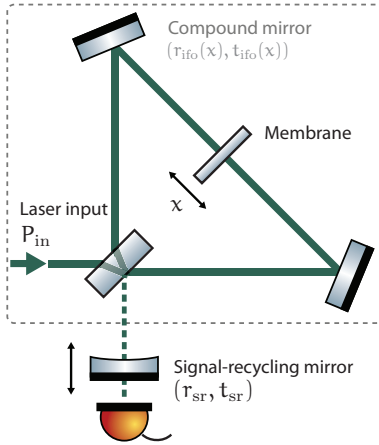


**Figure 5.3:** The effective cavity consists of a high-reflective signal-recycling mirror and the Michelson-Sagnac interferometer. The latter acts as compound mirror of variable amplitude reflectivity  $r_{\text{ifo}}(x)$ , which depends on microscopic position  $x$  of the membrane.

### 5.1.1 Effective cavity output power

The general output amplitude of the Michelson-Sagnac interferometer is given in Eq. (4.11), whereas the general expression for the interferometer amplitude reflection is given by Eq. (4.13). For simplicity, a balanced beam splitter is assumed,  $r_{\text{BS}}^2 = t_{\text{BS}}^2 = 0.5$  and the same choice of beam splitter phases as in Sec. 4.1 is used. Then, a membrane position  $x = 0$  equals a bright-fringe and the interferometer amplitude reflection and transmission coefficients can be written as

$$\frac{a_{\text{out}}^{\text{ifo}}}{a_{\text{in}}} = t_{\text{ifo}} = r_m \cos(2kx) \quad , \quad (5.14)$$

$$\frac{a_{\text{refl}}^{\text{ifo}}}{a_{\text{in}}} = r_{\text{ifo}} = t_m + r_m i \sin(2kx) \quad . \quad (5.15)$$

The Michelson-Sagnac interferometer can be considered as an effective mirror, whose amplitude reflection coefficient depend on the membrane's microscopic position. Inserting the above expressions into Eq. (5.5) for  $t_1$  and  $r_1$  allows to calculate the cavity output field (and power) as function of both membrane and recycling mirror position. A *Finesse* simulation [120] of the relative cavity output power has been performed for a balanced beam splitter and a recycling mirror reflectivity of  $r_2^2 = R_{\text{SR}} = 95\%$ . The result is depicted in Fig. 5.4.

If only one parameter is modified, this corresponds to an intersection parallel to one of the axis of Fig. 5.4. When scanning the membrane position for a fixed tuning of the recycling mirror, the outcome is depicted in Fig. 5.5. A scan of the signal-recycling mirror instead

## 5 Signal-recycled Michelson-Sagnac interferometer

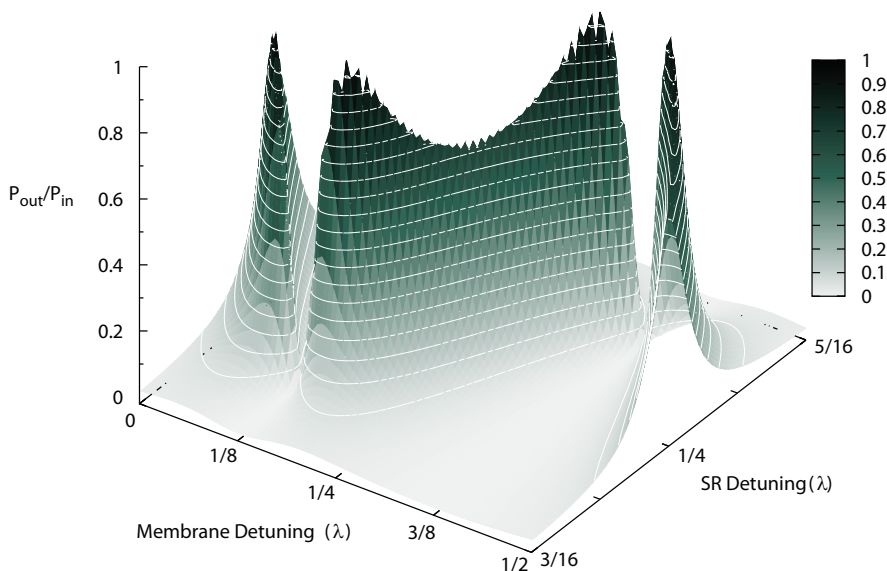


**Figure 5.4:** Normalised optical output power as function of membrane and recycling mirror detuning. White lines depicts levels of constant height. Interferometer and recycling mirror tuning are correlated, such that the tuning of the recycling mirror has to be adjusted for each membrane position. Here,  $r_m^2 = 0.17$  was assumed. For a pure Michelson interferometer ( $r_m^2 = 1$ ), both tunings are independent, and all interferometer dark-fringes line up at the same tuning of the SRM. Spikes on top are caused by the finite resolution of the simulation.

produces a cavity resonance profile as described in Fig. 5.2.

A maximal of ratio of  $P_{\text{out}}/P_{\text{in}} = 0.9$  was transmittable through the cavity. The difference to a complete transmission of input power was due to optical loss, which caused an impedance mismatch of the cavity.

### 5.1.2 Signal-Recycling

The additional mirror in the interferometer output port can be used to increase the interferometer sensitivity [54, 121–125], as signals that are generated inside the cavity (interferometric signals) are resonantly enhanced. The amplitude gain can be calculated from the ratio  $a_0/b_1$  (compare Fig. 5.1). Solving the set of equations yields

$$\frac{a_0}{b_1} = \frac{t_2 e^{ikd}}{1 - r_1 r_2 e^{2ikd}} \quad . \quad (5.16)$$

In the case of the signal-recycled Michelson-Sagnac interferometer,  $r_1 = r_{\text{ifo}}$  and  $r_2 = r_{\text{sr}}$  are the interferometer and signal recycling

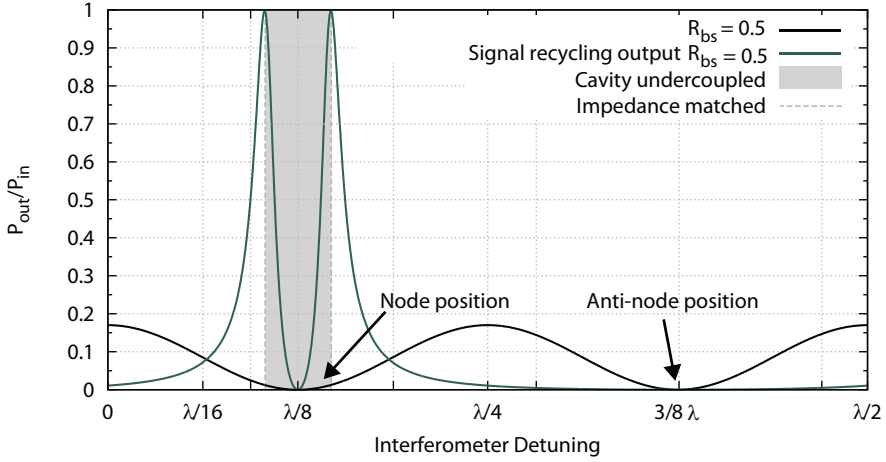


**Figure 5.5:** Green: Normalised transmitted power through the effective cavity. The Michelson-Sagnac interferometer is assumed to have a perfect contrast, a beam splitter ratio of 50/50 and a membrane power reflectivity of  $r_m^2 = 17\%$ . If the detuning of the interferometer is chosen such that the interferometer reflectivity  $r_{\text{ifo}}$  matches the signal recycling reflectivity  $r_{\text{sr}}$  the cavity becomes impedance matched and all incident light is transmitted. The interferometer output power is shown as black curve. The gray area depicts a situation in which the  $r_{\text{ifo}} > r_{\text{sr}}$ , such that the cavity is undercoupled.

mirror amplitude reflectivities, respectively. On the cavity resonance, Eq. (5.16) simplifies to

$$\frac{a_0}{b_1} = \frac{-t_{\text{sr}}}{1 - r_{\text{ifo}}r_{\text{sr}}}, \quad (5.17)$$

which is maximized for  $r_{\text{ifo}} = 1$ . This is the interferometer dark-fringe condition. Tuning the interferometer such that  $r_{\text{ifo}} > r_{\text{sr}}$  results in an undercoupled cavity (as seen from the input port). The power gain  $G_{\text{sr}}$  is given by

$$G_{\text{sr}} = \left| \frac{a_0}{b_1} \right|^2 = \frac{t_{\text{sr}}^2}{(1 - r_{\text{sr}})^2} = \frac{(1 - r_{\text{sr}})(1 + r_{\text{sr}})}{(1 - r_{\text{sr}})(1 - r_{\text{sr}})} = \frac{1 + r_{\text{sr}}}{1 - r_{\text{sr}}}. \quad (5.18)$$

Vacuum fluctuations are amplified with  $\sqrt{G_{\text{sr}}}$  (amplitude gain) for  $f < f_c$ . The expression for the relative shot noise level (Eq. (4.23)) is thus modified [86] to

$$G_{\text{shot}}^x = \sqrt{\frac{\hbar c \lambda}{16\pi r_m^2 G_{\text{sr}} P_{\text{in}}}} \sqrt{1 + \left(\frac{f}{f_c}\right)^2}, \quad (5.19)$$

## 5 Signal-recycled Michelson-Sagnac interferometer

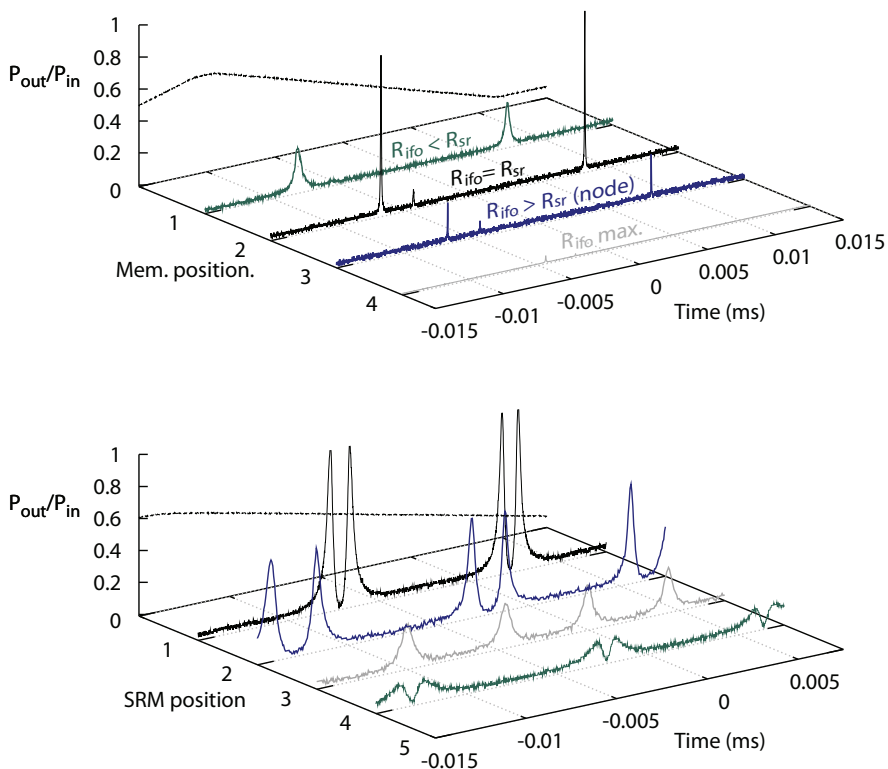


**Figure 5.6:** Scans of the signal recycling mirror position for different membrane positions (upper plot). The dashed line (membrane position 0) shows the applied piezo voltage in each plot. Bottom plot: Scans of the microscopic membrane position for different (fixed) signal recycling mirror positions. The recycling mirror reflectivity was  $r_{sr}^2 = 99\%$ .

whereas the quantum back-action noise (Eq. (4.26)) with recycling mirror is

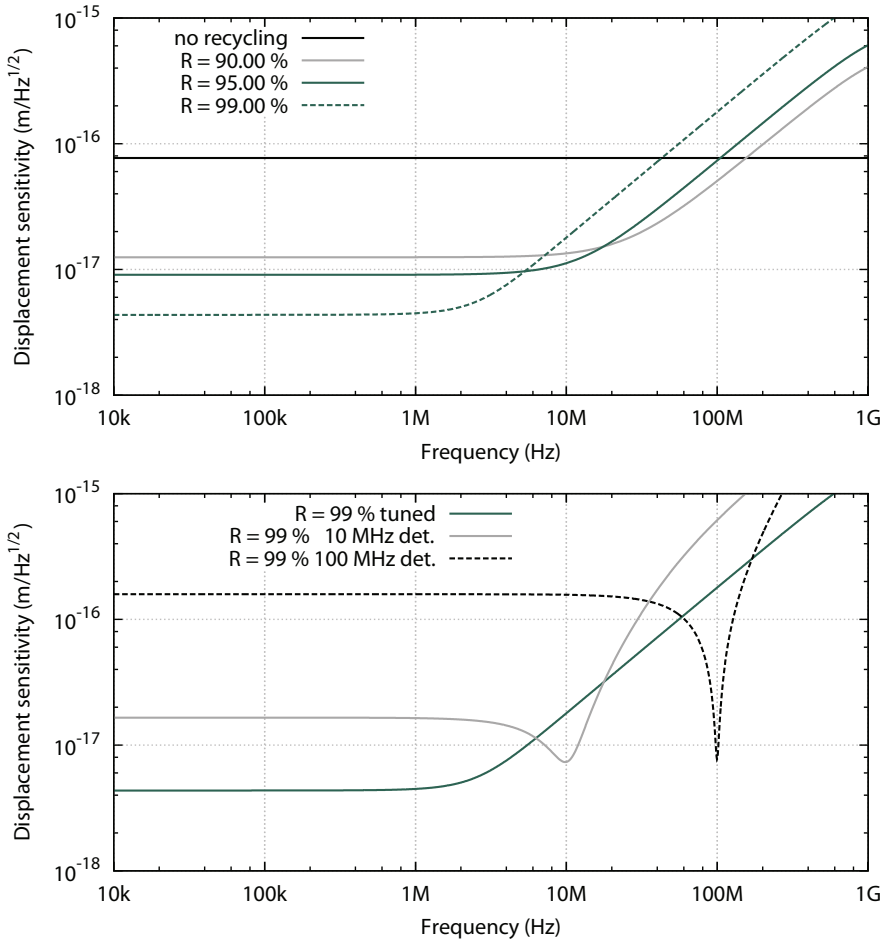
$$G_{\text{rpn}}^x = |G(\omega)| \sqrt{\frac{16\pi\hbar r_m^2 G_{\text{sr}} P_{\text{in}}}{c\lambda}} \frac{1}{\sqrt{1 + (f/f_c)^2}}. \quad (5.20)$$

Fig. 5.7 illustrates the interferometer sensitivity gain achieved by signal-recycling for various recycling mirror power reflectivities  $r_{sr}^2$  and allows for a comparison without signal-recycling.

The calculation assumes  $r_m^2 = 0.17$ ,  $d = L_{\text{sr}} + L_{\text{ifo}} = 2(1.2 \text{ cm} + 7.5 \text{ cm}) = 17.4 \text{ cm}$  and an optical input power of  $P_{\text{in}} = 1 \text{ W}$  with no loss in the cavity and a laser wavelength  $\lambda = 1064 \text{ nm}$ .

The above considerations result in a constant optical gain-bandwidth





**Figure 5.7:** Displacement sensitivity enhancement due to a signal-recycling mirror. First, shown as a function of signal-recycling mirror power reflectivity  $R_{sr}$  and second, as a function of the cavity detuning. As comparison, the interferometer sensitivity without recycling mirror is shown (this corresponds to  $R_{sr} = 0$ ). Here, an optical input power of 1 W was assumed, and a membrane power reflectivity of  $r_E^2 = 0.17$ .

product

$$G_{sr} \cdot f_c = \frac{c(1 + r_{sr})}{2\pi L} \approx \frac{c}{\pi L} \quad . \quad (5.21)$$

Hence, higher optical gain comes at the expense of a narrower cavity linewidth. Thus, to maintain a sufficient optical linewidth (bigger than the mechanical resonance frequency  $f_{res} \approx 100$  kHz) for high optical gain, the cavity has to be short. For a signal recycling gain

## 5 Signal-recycled Michelson-Sagnac interferometer

---

$\sqrt{G_{\text{sr}}} = 30$  and a linewidth of 200 kHz, the cavity length (including the interferometer arm length) has to be smaller than 10 cm [76]. This length was already considered when designing the experiment. The interferometer arm length was chosen to about 7.5 cm, and the distance between beam splitter and signal-recycling mirror is 1.2 cm.

### 5.1.3 Design considerations for the effective cavity

When designing the effective cavity of length  $L$ , the cavity stability criterion has to be fulfilled

$$|g_1 g_2 - 1| < 1 \quad . \quad (5.22)$$

Here,  $g_i = 1 - L/R_i$  with  $R_i$  being the radius of curvature of mirror  $i$  and  $L$  is the optical length. As the membrane is flat, ( $R_m = \infty$ ), Eq. (5.22) results in  $0 < L < R_{\text{sr}}$ . A more severe restriction follows from the fact that the laser beam has a gaussian intensity profile. Here, the beam waist  $w(z)$  is defined as the radial distance from the beam axis center, at which the beam intensity has dropped to a fraction of  $1/e^2$  of its maximum value. Its relation as a function of the distance to the waist position is given by

$$w(z) = w_0 \sqrt{1 + \left(\frac{z}{z_0}\right)^2} \quad , \quad (5.23)$$

where  $z_0 = \pi\omega_0^2/\lambda$  is the Rayleigh range,  $w_0$  is the minimum beam size ( $z = 0$ ), and  $\lambda$  is the optical wavelength.

The wavefront curvature of the beam is a function of propagated distance from waist position along the beam path

$$R(z) = z \left(1 + \left(\frac{z_0}{z}\right)^2\right) \quad . \quad (5.24)$$

The radii of curvature of the wave front and of the mirror surfaces have to match. For the plane membrane this corresponds to a waist position at the membrane position, such that the radius of curvature  $R(z)$  of the recycling mirror is determined by Eq. (5.24). For the waist size on the membrane another restriction is given by the membrane finite size. The waist size has to be small compared to the size of the membrane, otherwise beam clipping occurs, resulting in optical loss within the cavity. Assuming the membrane as circular aperture (radius  $a = L_x/2$ ), the loss for a spot diameter  $\omega = 2\omega_0$  can be approximated to [126]

$$\text{Loss} = \left( \frac{2}{\pi\omega^2} \right) \int_0^a 2\pi t e^{-2t^2/\omega^2} dt = e^{-2a^2/\omega^2} \quad . \quad (5.25)$$

For  $a > 5/2 \omega$ , the loss caused by beam clipping thus becomes smaller than 40 ppm. This is a conservative calculation, however. In reality, the loss is even smaller, because the membrane area is a square, not a disc.

### 5.1.4 The impact of optical losses

Another issue is already mentioned by [76]: even if the cavity linewidth was not limiting (if an arbitrarily small arm length was possible), the signal-recycling gain would depend on the optical loss within the cavity. In reality, the usage of a signal recycling mirror can increase the interferometer sensitivity - or not.

Thus far, the interferometer alignment and all optics were assumed ideal and there seems no reason not to increase  $r_{\text{sr}}$  for a maximal enhancement factor and thereby arbitrary low relative shot noise level, as long as the relevant frequencies are still within the cavity linewidth. In reality, however, a variety of reasons limit the maximally usable signal recycling mirror reflectivity, such as non-ideal interferometric contrast and optical loss within the interferometer. The impact of the first is partially compensated by the so-called 'mode-healing' effect [54]. The optical loss cannot be compensated by this effect, however, and needs to be considered. This is of particular importance for high reflective recycling mirrors, whose power transmissivity  $T_{\text{sr}}$  is comparable to the intrinsic optical loss of the interferometer.

An estimate of acceptable loss within the cavity can be derived from the cavity transfer function. Loss in the cavity is modelled by its amplitude de-amplification  $\nu$  within the cavity (compare Fig. 5.1). Solving the general set of equations, the transfer function (for cavity resonance and interferometer on dark-fringe) can be written as

$$\frac{a_0}{b_1} = \frac{-i\nu t_{\text{sr}}}{1 - \nu^2 r_{\text{sr}}} \quad . \quad (5.26)$$

If  $|a_0/b_1| = 1$ , the signal-recycling gain is unity. Solving Eq. (5.26) for this criterion results in the maximum acceptable loss  $1 - \nu^2$  within the cavity of

$$\left| \frac{a_0}{b_1} \right| \stackrel{!}{=} 1 \Rightarrow 1 - \nu^2 \approx t_{\text{sr}}^2/4 \quad . \quad (5.27)$$

## 5 Signal-recycled Michelson-Sagnac interferometer

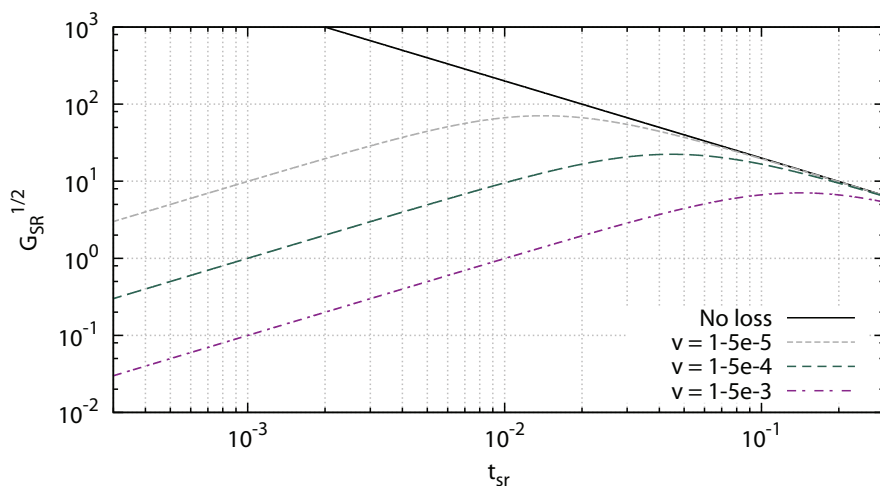


**Figure 5.8:** Signal-recycling gain as function of the signal-recycling mirror amplitude transmissivity  $t_{\text{sr}}$  for different loss parameters  $\nu$  in the cavity. For zero loss ( $\nu = 1$ ), the signal-recycling gain can reach arbitrarily high values. In all other cases, it is limited and a maximum recycling gain exists.

For a signal-recycling mirror with  $r_{\text{sr}}^2 = 0.99$ ,  $t_{\text{sr}}^2 = 0.01$ , recycling is only beneficial for a loss significantly smaller than 0.25%. For the model discussed above, it is also possible to calculate an optimum value  $t_{\text{opt}}$  for the signal-recycling mirror transmissivity. Deriving Eq. (5.26) yields

$$\frac{\partial}{\partial t} \left( \frac{-i\nu t_{\text{sr}}}{1 - \nu^2 r_{\text{sr}}} \right) \stackrel{!}{=} 0 \Leftrightarrow t_{\text{opt}} = \sqrt{1 - \nu^4} \quad . \quad (5.28)$$

The resulting signal-recycling gain is depicted in Fig. 5.8. The optimum signal-recycling gain is a function of loss, and is achieved for the optimum amplitude transmissivity  $t_{\text{opt}} = \sqrt{1 - \nu^4}$ , such that  $t_{\text{sr}} = 0.1$  corresponds to a power reflectivity of  $R_{\text{sr}} = 99\%$ . The maximum signal-recycling gain is given by

$$G_{\text{sr,max}}^{1/2} = \frac{\nu}{\sqrt{1 - \nu^4}} \quad . \quad (5.29)$$

### 5.1.5 Loss in the cavity

As discussed in the previous section, the losses in the interferometer (and effective cavity) can cause a reduced displacement sensitivity. Here, a brief estimation for the loss within the Michelson-Sagnac interferometer will be presented. Each component of the interferometer is assumed to be imperfect by means of their optical properties. However, their individual contribution to the overall losses differs significantly.

**SiN membrane** The loss of the membrane is caused by the finite absorption during transmission through the membrane. Due to the sub-wavelength thickness of the membrane, it is possible to position the membrane in the node of the standing wave in the Sagnac interferometer. In [84], we have shown that for an index of refraction of silicon nitride ( $n_{\text{SiN}} = 2.2 + i \cdot 1.5 \cdot 10^{-4}$ ) at a laser wavelength of  $\lambda = 1064 \text{ nm}$  [37], the membrane optical loss can be smaller than 57 ppm.

**Steering mirrors** The loss caused by the steering mirrors depends on the quality of their HR coating. High quality, ion beam sputtered multilayer coatings can achieve  $R_{\text{HR}} = 99.999\%$  which corresponds to a round trip loss of  $2 \cdot 10 \text{ ppm}$ .

**Beam splitter** The interferometer beam splitter is a dual source of loss. First, the laser power has to be transmitted through the substrate, causing loss by absorption. High quality fused silica materials, such as *Suprasil 3001*<sup>®</sup> [127] provide optical absorption of 0.3 ppm/cm. A typical beam splitter thickness is a quarter of an inch, such that each transmission under  $45^\circ$  causes a 0.3 ppm loss. The second source of loss is the anti-reflective coating on the back side of the beam splitter. Manufacturer specifications for high quality AR coatings are  $R_{\text{AR}} \leq 0.01\%$  [128], but a more conservative estimation is  $R_{\text{AR}} \approx 0.01 - 0.05\% = 100 - 500 \text{ ppm}$ , causing a loss of  $2 \cdot (100 - 500 \text{ ppm})$ .

The overall optical loss is thus dominated by the beam splitter. The different loss contributions are depicted in Fig. 5.9. A conservative scenario assumes  $R_{\text{AR}} = 0.05\%$ , a more optimistic estimate is  $R_{\text{AR}} = 0.01\%$ . Either way, the beam splitter contribution to the overall optical loss is dominant and the optical loss exceeds 200 ppm.

## 5 Signal-recycled Michelson-Sagnac interferometer

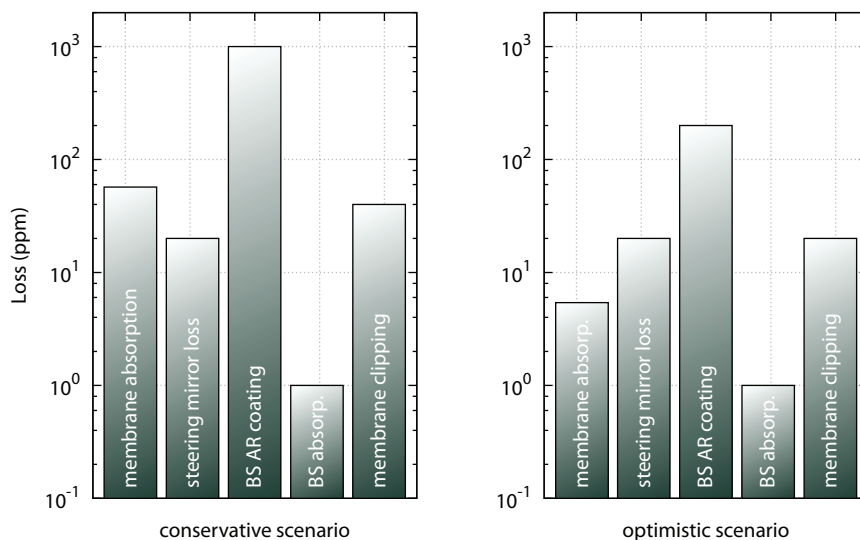


**Figure 5.9:** Loss channels in the effective cavity. The beam splitter anti-reflective coating is the largest source of loss. Left: conservative estimate of optical loss, beam splitter  $R_{AR} = 0.05\%$ . Right: more optimistic scenario, beam splitter  $R_{AR} = 0.01\%$  and thinner membrane, with slightly reduced spotsize on the membrane.

### 5.2 Realisation of the recycled interferometer

When installing a high-reflective signal-recycling mirror into the interferometer output port, this mirror must match the optical mode defined by the interferometer optical mode, which is not guaranteed a priori. The mirror radius of curvature has to match the curvature of the optical wavefront, and the interferometer mode might be translated in the horizontal or vertical direction with respect to the central axis of the recycling mirror. This problem is similar to the situation in which the membrane might not be hit by the Sagnac mode, because the Sagnac interferometer is invariant to pure beam translations, with one additional complication: when the cavity is not resonant, no light is transmitted. The amount of light transmitted on cavity resonance furthermore depends on the interferometer tuning, which is unstable while working in the vacuum tank. During the installation, the signal-recycling mirror position was continuously scanned, until optical modes were visible in transmission of the cavity. Fine positioning was then accomplished by the remote controllable mounts. A scan of the signal-recycling cavity length is depicted in Fig. 5.11. The two

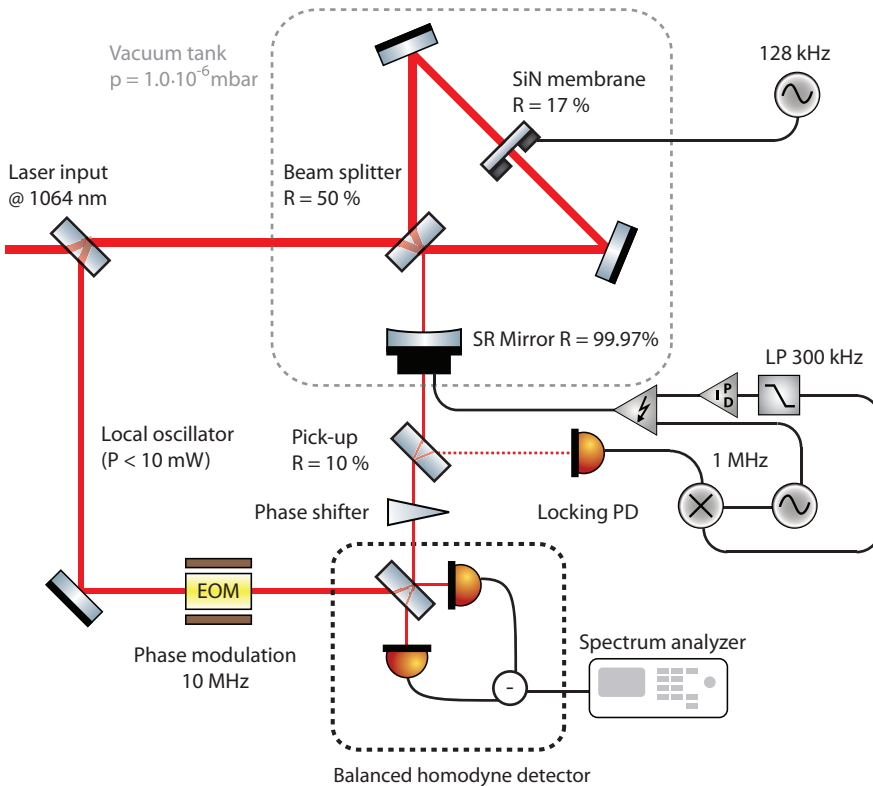


**Figure 5.10:** Setup of the signal-recycled Michelson-Sagnac interferometer. The interferometer output mode is transmitted through a 10% beam splitter. The beam split off is used to lock the recycling cavity. The main part of the output is transmitted to a phase shifter and finally overlapped with a stronger light field (the local oscillator) on a second, balanced homodyne beam splitter. Both light fields have the same optical frequency. The two beam splitter output ports are detected by two photo detectors. The difference of their signal is fed to a spectrum analyzer and provides the power spectral density of the output field.

resonances correspond to a TEM<sub>00</sub> mode and a smaller resonance of the TEM<sub>10</sub> mode, which could not be eliminated and was attributed to a small misalignment within the interferometer.

### 5.2.1 Cavity length stabilisation scheme

To keep the cavity resonant for the laser light, an appropriate error signal is required. In the experiment, this error signal was provided by a modulation / demodulation technique. It requires a defined phase modulation on one of the beams. In the experiment, this phase mod-

## 5 Signal-recycled Michelson-Sagnac interferometer

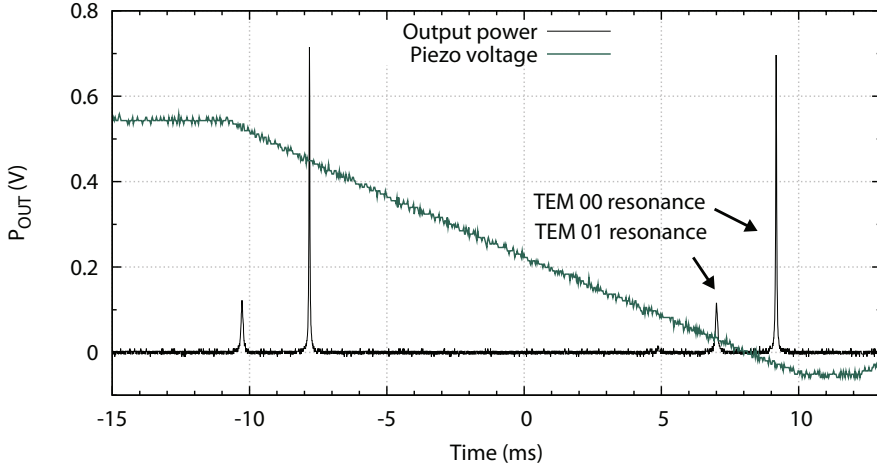


**Figure 5.11:** To scan the cavity, a ramp voltage has been applied to the SRM piezo, thus periodically changing the cavity length. The interferometer tuning was chosen as to maximise the power in the TEM00 mode (corresponds to  $\approx 3.0\%$  fraction of input power). The smaller peak is a resonance of TEM10 mode.

ulation was imprinted on the light field exiting the recycling cavity by applying a sinusoidal frequency to the signal-recycling mirror piezo actuator.

The cavity output power  $P_{\text{trans}}(x)$  (for a fixed interferometer tuning) is a typical cavity resonance profile (Airy peak) and was to be maximized. Therefore, the microscopic position  $x$  of the recycling mirror was modulated with a known frequency  $\omega_{\text{mod}}$ , such that  $x(t) = x_0 + a \cos(\omega_{\text{mod}}t)$ . Taylor expansion of  $P_{\text{out}}(x)$  at  $x_0$  now yields

$$P_{\text{trans}}(x) = P_{\text{trans}}(x_0) + P'_{\text{trans}}(x_0)(a \cos(\omega_{\text{mod}}t)) + \frac{1}{2}P''_{\text{trans}}(x_0)(a \cos(\omega_{\text{mod}}t))^2 + \dots \quad (5.30)$$

A demodulation at frequency  $\omega_{\text{demod}} = \omega_{\text{mod}}$  (multiplication with  $\cos(\omega_{\text{mod}}t)$ ) thus provides a DC signal proportional to the derivative  $P'_{\text{trans}}(x_0)$  around  $x_0$ . A fraction of the output power was split off the interferometer output mode and detected by a photo detector. The AC-filtered output was mixed electronically with a copy of the modulation signal. The mixer output was low-pass filtered ( $f_c = 300$  kHz) and fed back to a control loop for the SR mirror position. In the experiment, the modulation frequency  $f_{\text{mod}} = \omega_{\text{mod}}/(2\pi) \approx$



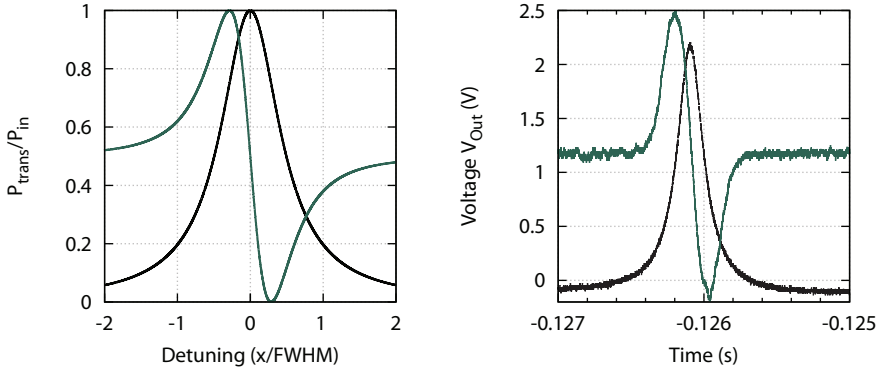


**Figure 5.12:** Cavity output power and derivative. Left: theoretical cavity resonance profile. The fractional output power is depicted as black trace, its first order derivative is plotted in green. On the right side, a scan above the cavity resonance is depicted. Black is the detected voltage on a photo detector in transmission of the cavity, green is the error signal (both traces have been rescaled).

1 MHz was chosen. This relatively high frequency exhibits several benefits. First, a high control-loop bandwidth after low-pass filtering the signal and second, higher order harmonics of the modulation are well outside the frequency range of interest (which is typically around the mechanical resonances). The responses of both, the high-voltage amplifier and the piezo ceramic transducer are typically zero at such high frequencies, but it was still possible to generate an excitation of the piezo by exploiting a very narrow mechanical piezo resonance. This scheme was found to provide acceptable error signals as depicted in Fig. 5.12 for the interferometer operated close to dark-fringe. The signal to noise ratio of this error signal becomes arbitrarily small when the interferometer is tuned to dark-fringe, however.

Because no further constraints on the function  $P_{\text{trans}}$  were given other than it actually exhibits some extreme value, this locking scheme can also be applied to lock the relative phase between the local oscillator and signal beam. In principle, it can also be used to lock the interferometer close to dark-fringe. The situation is complicated by the fact that the error signal for the interferometer lock depends on the signal-recycling gain. For a random position of the signal-recycling mirror, the gain  $G$  for the interferometer control loop varies between a maximum and minimum value  $g_{\text{max}}$  and  $g_{\text{min}}$  with

$$G = \frac{g_{\text{max}}}{g_{\text{min}}} = \left( \frac{1 + r_{\text{sr}}}{1 - r_{\text{sr}}} \right)^2, \quad r_{\text{sr}} = \sqrt{0.95} \Rightarrow G \approx 6000 \quad . \quad (5.31)$$

## 5 Signal-recycled Michelson-Sagnac interferometer

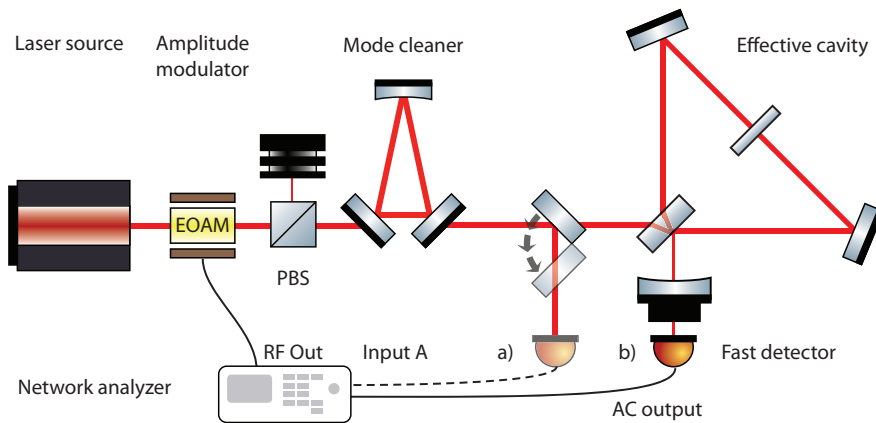


**Figure 5.13:** Schematic of the setup for measuring the effective cavity linewidth. An EOAM modulates the input beam power, which is transmitted through the mode cleaner. This acts as an optical lowpass. The transfer function was measured a) directly in transmission of the mode cleaner and b) for additional transmission through the effective cavity.

For a derivation, the reader is referred to the thesis of G. Heinzel [119]. Eq. (5.31) explains why the signal-recycling mirror has to be close to resonance before the interferometer can be locked. The gain for the signal-recycling mirror on the other hand depends on the interferometer tuning. Thus, to lock both, interferometer and cavity, the membrane position already has to be correct before an appropriate error signal for its lock can exist. The coupling of individual error signals is of fundamental importance for any complex interferometric setup and for gravitational wave detectors in particular [54].

### 5.2.2 Effective cavity optical linewidth

To measure the optical linewidth of the effective cavity, its frequency response function was probed. Therefore, the laser light amplitude was modulated by an electro-optic amplitude modulator in front of the mode cleaner cavity, and the transfer function of the recycling cavity was measured with a network analyser. This method has been described in [129]. In the experiment, the setup used is depicted in Fig. 5.13.

A reference output signal was applied to the EOAM in front of the first mode cleaner cavity. The AC filtered output of a single photo detector in transmission of the mode cleaner was used to obtain the transfer function of the subsystem : EOAM, mode cleaner and photo detector.

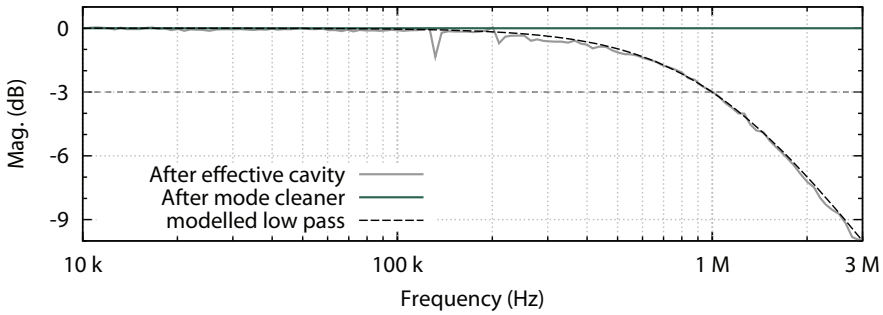


**Figure 5.14:** Normalised transfer function of the modulator, mode cleaner and photodetector (green trace). An additional low pass behavior is observed in transmission to the effective cavity (grey trace), due to the finite linewidth. The modelled low pass is shown as black, dashed line. The corner frequency ( $-3$  dBm) level is reached for frequencies of about 1 MHz.

A measurement in transmission of the effective cavity, shows an additional low pass behaviour in the overall transfer function, attributed to the finite cavity linewidth. The interferometer was operated close to the dark-fringe in this measurement, such as to achieve the minimal possible linewidth. The linewidth (HWHM) was determined as the  $-3$  dB level. The result is depicted in Fig. 5.14. A cavity linewidth of 1 MHz could be inferred from the measurement.

### 5.2.3 Displacement sensitivity

The shot noise equivalent displacement spectral density for the signal-recycled interferometer was calculated numerically with a *Finesse* simulation script of the interferometer [118], see Appendix 8.1. The interferometer is set to dark-fringe and is assumed to exhibit a perfect interference contrast. Furthermore, a signal-recycling mirror of  $r_{\text{sr}}^2 = 99.97\%$  power reflectance was assumed and the interferometer arm length was set to 7.5 cm. The distance between signal-recycling mirror and beam splitter was 1.2 cm, and the membrane power reflectivity  $r_{\text{m}}^2 = 17\%$ . An equivalent optical input power of 200 mW was assumed, and a mode matching of 80%. Thus, simulation and experimental parameters match.

The simulation allows to incorporate loss into the cavity. The correct amount of loss was determined by measuring the maximal transmittable fraction of the optical input power. This fraction measured to be 3% (compare Fig. 5.15) for the TEM00 mode, which yields an optical loss of about 1% in the interferometer. Compared to the lossless

## 5 Signal-recycled Michelson-Sagnac interferometer

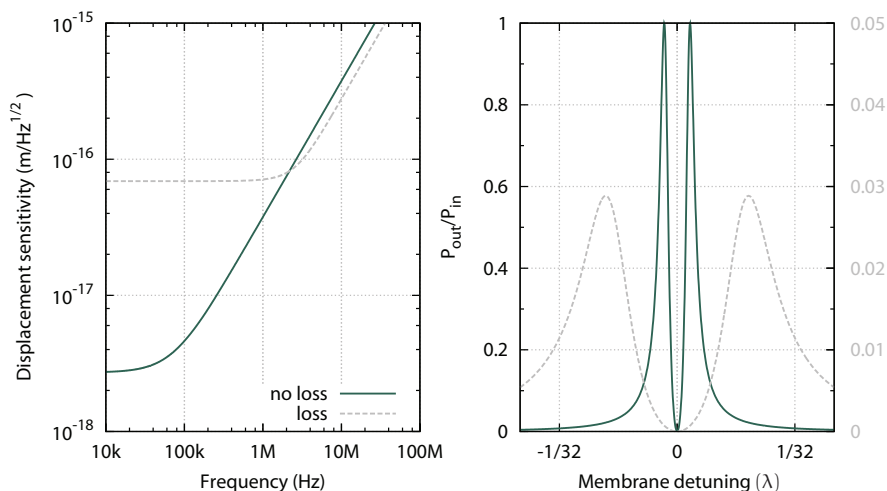


**Figure 5.15:** Left: Simulated displacement equivalent shot noise level of the signal-recycled Michelson-Sagnac interferometer on dark-fringe with  $r_{\text{sr}}^2 = 99.97\%$ . Here, the tuned case is considered for no loss (grey) and loss within the cavity (green). Right: Transmittable fraction of optical input power for no loss (green) and loss (grey). In case of 1% optical loss, a maximal fraction of 0.03 of optical input power is transmittable through the effective cavity.

case, the displacement sensitivity is significantly reduced. A comparison of the shot noise equivalent displacement in both cases is depicted in Fig. 5.15. The recycling gain is approximately unity, such that no increase in displacement sensitivity was expected.

It is necessary to keep in mind which assumptions were made to simulate the sensitivity and to critically analyse to which degree they are justified. Especially the condition for dark-fringe operation of the interferometer is not fulfilled in reality, as this eliminates the error signal of both the cavity and the homodyne phase lock. The interferometer is tuned slightly off dark-fringe, causing an increased amplitude transmissivity towards the laser port and will thereby increase the relative shot noise level even further, as will optical loss in the detection path. The above considerations may be summarized as follows: In case of signal-recycling, and to achieve an enhanced displacement sensitivity, it is mandatory to operate the recycling cavity undercoupled. Side bands generated inside the cavity will then leave towards the detection port. For given optical loss, the signal-recycling gain exhibits a maximum value for one particular reflectivity of this mirror.

A further increase will result in the same resonant enhancement of signals, but a smaller fraction is transmitted to the detection side.

Hence, the signal-recycling gain is reduced again. Yet, there are good reasons to install very high-reflective end-mirrors. This will be issued in the next Section.

### 5.3 Opto-mechanical interaction

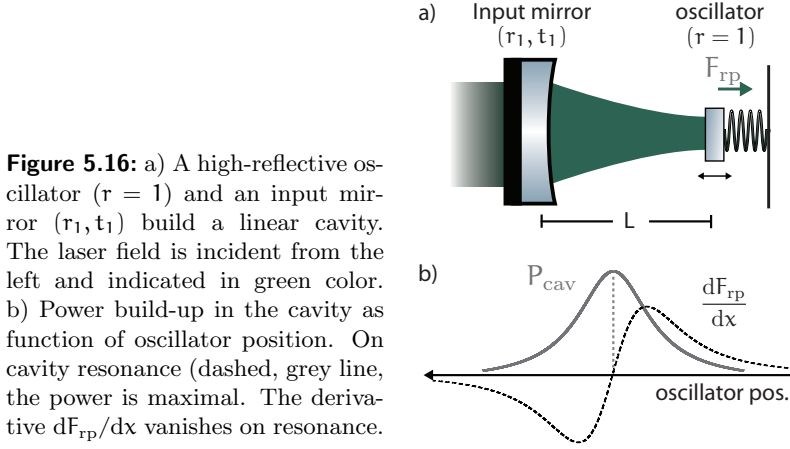
This section describes the opto-mechanical interactions within a signal-recycled Michelson-Sagnac interferometer. To understand some of the interaction effects, such as the optical spring, parametric instabilities and optical cooling, it is intuitive to imagine the system as an effective Fabry-Perot cavity, which also exhibits these features. In this case, one of the two cavity mirrors is replaced by the effective, Michelson-Sagnac interferometer, which acts as an effective mirror when operated close to dark-fringe. The reflectivity of this effective mirror then depends on the microscopic membrane position.

It has to be kept in mind that a linear cavity is different from a two-path Michelson-type interferometer by nature. A linear cavity contains a single optical mode, a Michelson (or Michelson-Sagnac) interferometer overlaps two optical modes on a central beam splitter. In a linear cavity, the microscopic position of the oscillator modifies the cavity length (and associated resonance frequency and FSR), and thereby the cavity resonance frequency. In case of the recycled Michelson-Sagnac interferometer, the membrane position does not modify the length of the effective cavity, but modifies the complex reflectivity of the effective mirror in Eq. (5.10). It thereby modifies both the resonance frequency and the linewidth of the cavity. It is due to this dependence that the full interaction exhibits additional features, such as conditional instabilities and cooling on signal-recycling cavity resonance.

#### Fabry-Perot cavity

A linear, Fabry-Perot cavity is a frequently used topology throughout the field of opto-mechanics [28, 29, 36, 49, 130]. The cavity consists of two mirrors (compare Fig. 5.16), with one mirror serving as harmonic oscillator while the second mirror is assumed fix. The oscillating mirror is assumed to exhibit unity amplitude reflectance  $r_2 = 1$  and the input mirror amplitude reflectivity  $r_1 < 1$  and transmissivity  $t_{\text{in}}$  with  $t_1^2 = (1 - r_1^2)$ , in case of zero loss within the cavity. For convenience, the following section considers angular frequencies  $\omega = 2\pi f$ . If the

## 5 Signal-recycled Michelson-Sagnac interferometer



macroscopic cavity length is  $L$ , then the cavity is resonant for frequencies

$$\omega_n = \pi \frac{nc}{L}, \quad n \in \mathbb{N}, \quad (5.32)$$

such that  $\text{FSR} = \pi c/L$ . The cavity linewidth (HWHM)  $\gamma_{\text{cav}}$  then is (compare Eq. (5.10))

$$\begin{aligned} \gamma_{\text{cav}} &= \frac{1}{2} \text{FWHM} = \frac{\text{FSR}}{\pi} \arcsin\left(\frac{1 - r_1 r_2}{2\sqrt{r_1 r_2}}\right) \\ &= \frac{c}{L} \arcsin\left(\frac{1 - r_1}{2\sqrt{r_1}}\right) \approx \frac{c}{L} \left(\frac{1 - r_1}{2\sqrt{r_1}}\right) \\ &\approx \frac{c}{2L} (1 - r_1) \approx c \frac{|t_1|^2}{4L}. \end{aligned} \quad (5.33)$$

Here, three approximations were made. First,  $\arcsin(x) \approx x$ , which is valid for  $x \ll 1$ . Second,  $\sqrt{r_1} \approx 1$ , and finally

$$|t_1|^2 = (1 - r_1^2) = (1 + r_1)(1 - r_1) \approx 2(1 - r_1). \quad (5.34)$$

All of these approximations are valid for  $r_1 \approx 1$ . On resonance, the power build-up in the cavity is maximal, as can be seen from  $|a_2|^2$  in Eq. 5.3. In this situation, a constant optical force  $F_{rp}$  is caused by the power within the cavity, which has to be stabilised by some kind of feedback. The oscillator now experiences a position dependent optical force. The sign of the force depends on the detuning: Suppose an initial cavity length  $L_0$ , which is larger than the cavity resonance

length  $L$ . When the oscillator moves towards (away from) the input mirror, more (less) power is build-up within the cavity, causing a larger (smaller) repulsive optical force. If the initial length  $L_0 < L$ , the optical force is not repulsive but attractive. The position dependent optical force can be considered as an optical spring [131] in linear approximation. However, because of the finite cavity decay rate, the cavity can not react to a change of length instantaneous, such that there exists a frequency dependent time delay between the change of length the optical force. The oscillators equation of motion is modified by an additional optical force  $F_{rp}(\omega) = -\kappa(\omega)x(\omega)$ . It can be shown that the total (complex) optical spring is given by [132]

$$\kappa(\omega) = \frac{4\omega_c P_{cav}}{cL} \frac{\delta}{(\gamma_{cav} - i\omega)^2 + \delta^2} . \quad (5.35)$$

Here,  $P_{cav}$  is the laser power inside the cavity. The optical spring constant  $K$  and optical damping  $\Gamma$  result out of the real- and imaginary part of  $\kappa(\omega)$ , with

$$K = \Re[\kappa(\omega)] = \frac{4\omega_c P_{cav}}{cL} \frac{\delta(\delta^2 + \gamma_{cav}^2 - \omega^2)}{|\delta^2 + (\gamma_{cav} - i\omega)^2|^2} , \quad (5.36)$$

$$\Gamma = -\frac{1}{2\omega} \Im[\kappa(\omega)] = -\frac{4\omega_c P_{cav}}{cL} \frac{2\delta\gamma_{cav}}{|\delta^2 + (\gamma_{cav} - i\omega)^2|^2} . \quad (5.37)$$

The above expressions modify both the mechanical damping and the mechanical resonance frequency. The oscillator effective damping is then given by

$$\gamma_{eff} = \gamma + \gamma_{OM}, \quad \gamma_{OM} = \Gamma . \quad (5.38)$$

The modified spring constant also results in an effective mechanical resonance frequency  $\omega_{eff}^2$

$$\omega_{eff}^2 = \omega_0^2 + \omega_{OM}^2, \quad \omega_0^2 = k/m, \quad \omega_{OM}^2 = K/m . \quad (5.39)$$

It can be seen from Eq. (5.37) that the strength of the optical spring depends on the available input power  $P_{in}$  and the cavity enhancement factor. Thus, a high cavity finesse (and small, associated linewidth  $\gamma_{cav}$ ) is beneficial.

### 5.3.1 Parametric instability

An interesting consequence follows out of Eq. (5.38). Due to the ability to generate negative optical damping  $\gamma_{OM} < 0$ , it is possible to

## 5 Signal-recycled Michelson-Sagnac interferometer

---

generate an anti-damped oscillator  $\gamma_{\text{eff}} < 0$ , with an effective quality factor  $Q_{\text{eff}} = m\omega_{\text{eff}}^2/\gamma_{\text{eff}} < 0$ . In this case, the faintest excitation at this frequency gets amplified exponentially, as can be seen from Eq. (3.33). Note that in the case of a linear cavity, this is possible only for one sign of the cavity detuning, namely where the optical spring acts anti-damping and restoring. In fact, this behaviour can be observed in the signal-recycled Michelson-Sagnac interferometer as well. When a signal-recycling mirror with a power reflectivity of  $R_{\text{SR}} = 99.0\%$  was installed and the interferometer input power was increased above 1 mW, a parametric instability was observed for one particular detuning of the cavity. To demonstrate the effect, the cavity length was scanned by applying a saw-tooth high voltage to the signal-recycling mirror piezo actuator, which thereby modified the length of the effective cavity. The membrane position was chosen near to the interferometer dark-fringe for these measurements. The cavity output power time series is depicted in Fig. 5.17. A parametric instability is observed only for one particular sign of cavity detuning  $\delta$ . The frequency of oscillations were found very close to the fundamental resonance frequency of the oscillator, such that within the measurement precision, no noticeable change of frequency was observed. This is explainable by the fact that  $K$  and  $\Gamma$  can still be small to produce the instability: In case of a high-frequency, high-Q mechanical oscillator, the mechanical damping  $\gamma$  is small and it only requires slight optical anti-damping to overcompensate it. Thus, the (absolute) modification to the mechanical resonance frequency will also be small.

Parametric instabilities are the mechanical analog to the process of optical lasing. They are a well known feature of optical springs, and have been observed in other opto-mechanical setups [44, 133–136].

### 5.3.2 Optical cooling

For the opposite detuning of the cavity, the optical spring causes optical damping  $\Gamma$ , which suppresses oscillator position fluctuations. The thermal excitation spectrum of the oscillator is unchanged by optical forces [44], such that to maintain the form of Eq. (3.23) (and neglecting technical laser noise), an effective temperature  $T_{\text{eff}}$  is introduced, which is given by

$$T_{\text{eff}} = T \frac{\gamma}{\gamma_{\text{eff}}} \quad (5.40)$$

The bottom plot in Fig. 5.17 depicts the measured cavity resonance



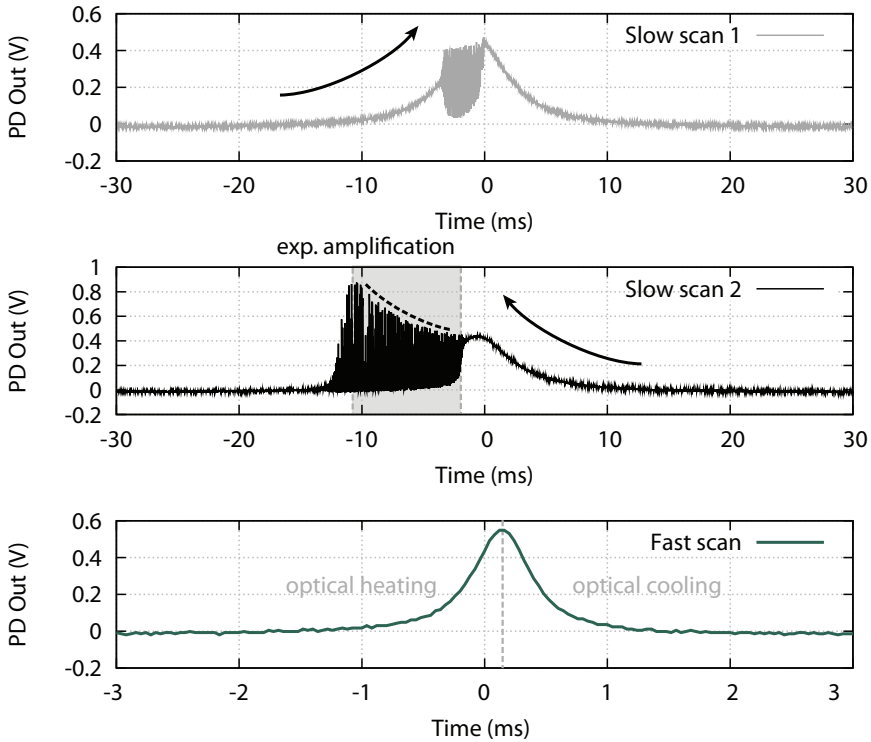


**Figure 5.17:** Scans of the signal-recycling cavity length. The measurement was performed with a  $R_{\text{SR}} = 99.0\%$  mirror. If the scan velocity is slow, one detuning of the cavity excited oscillations with precisely the membrane fundamental resonance frequency. The amplitude of this oscillation is exponentially increasing. If the scan velocity is high, the oscillations can not build up, and are not observed (bottom plot).

profile and the two regions of optical damping and anti-damping. According to Eq. (5.40), this corresponds to optical cooling and heating. Optical cooling is not identical to physical cooling. In the latter case, the sample temperature  $T$  is reduced, while in the first case, the oscillator is coupled to an additional temperature reservoir, the optical field, which is effectively at zero temperature. Therefore the net effect is to reduce the effective temperature of the oscillator. This comes the cost of an equal decrease in the quality factor. Also, there is an implicit frequency dependence in  $\Gamma$ ,  $\Gamma = \Gamma(\omega)$ , such that the damping is frequency dependent. Some mechanical modes might be cooled optical, while others might not be.

### Dispersive and dissipative coupling

In a linear cavity, the oscillator position modifies the cavity length  $L$ . Thereby, the cavity resonance frequency  $\omega_c$  is modified, resulting in an altered resonance condition for the optical field within the cavity (dispersive coupling). The cavity linewidth  $\gamma$  is also affected by the oscillator position, as can be seen from Eq. (5.33). The oscillator thereby causes a modified cavity decay rate, such that this mechanism is referred to as dissipative coupling. Their individual strength is given by

$$g_\omega = \left( \frac{\partial \omega_c}{\partial x} \right), \quad g_\kappa = \left( \frac{\partial \gamma_{cav}}{\partial x} \right) . \quad (5.41)$$

Their ratio is

$$g_\omega/g_\kappa = \omega_c/\gamma_{cav} = \mathcal{F} ,$$

with  $\mathcal{F}$  being the cavity finesse. Since typical cavity finesse values fulfil  $\mathcal{F} \gg 1$ , the coupling is highly dispersive. Dispersive coupling is the leading order interaction in linear cavities.

In the effective cavity of the signal-recycled Michelson-Sagnac interferometer, the microscopic position of the membrane modifies the compound Michelson-Sagnac mirror reflectivity  $r_{ifo}$ , whereas the total optical length of the cavity remains constant (one arm extends while the other is shortened). Thus, a direct modification of the cavity finesse  $\mathcal{F}$  is possible (compare Eq. (5.10)).

Dissipative coupling and its implications have been theoretically studied in [52, 137]. In case of this coupling mechanism, the unsymmetrised back-action force spectral density features a Fano line shape (instead of a Lorentzian resonance profile). This is a direct result of the interference of a resonant and a non resonant process. As a consequence, the coupling allows for strong optical cooling in the unresolved side band regime. This is impossible in linear cavity opto-mechanical setups.

An experimental demonstration of dissipative coupling is given in [138]. In [53] it was shown that the signal-recycled Michelson-Sagnac interferometer can allow for a strong and purely dissipative opto-mechanical coupling, under the assumption of a perfect mirror in the interferometer output port. In the previous chapter, the consequence of such a choice of signal-recycling mirror to achievable displacement sensitivity was discussed.

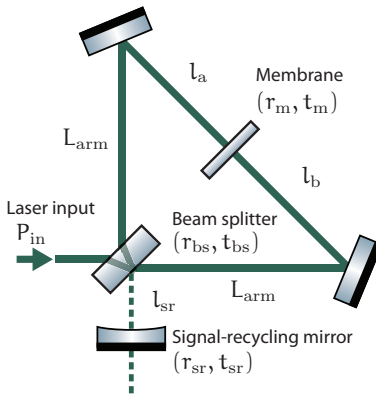


**Figure 5.18:** Schematic of the signal-recycled Michelson-Sagnac interferometer. The effective length  $L$  of the recycling cavity is  $L = l_{sr} + L_{arm} + l$ .

### Scaling law

The scaling law [139] states that the Fabry-Perot scenario also applies to an interferometer with highly reflective recycling mirror, in case of operation on dark fringe. However, dark-fringe operation represents a particular choice of interferometer tuning only: A dark-fringe offset not only results in a modified compound mirror reflectivity, but also in anomalous back-action effects, which are not covered in the expression for the optical spring deduced linear cavity picture. Since DC readout (off-dark fringe operation) is the method of choice for all large scale GW detectors at the moment, a more accurate description of the interaction is provided by the theoretical analysis in [140], which can also be applied to the signal-recycled Michelson-Sagnac interferometer.

#### 5.3.3 Optical spring in the Michelson-Sagnac interferometer

The general equation for the complex optical spring in a Michelson-Sagnac interferometer can be derived by calculating the fields impinging on the membrane using a transfer matrix approach [141] for the input and output optical fields. In the Michelson-Sagnac case, the calculation is quite cumbersome and beyond the scope of this work. Instead, the expression for a small interferometer offset from dark-fringe is given by [140]

## 5 Signal-recycled Michelson-Sagnac interferometer

---

$$\kappa(\omega) = \frac{4\omega_0 r_m^2 P_{\text{in}}}{cL} \frac{1}{\gamma_{\text{tot}}^2 + \Delta^2} \cdot \left\{ \frac{\delta_{\text{sr}}[\gamma_{\text{tot}}^2 + \Delta^2 - 4(\gamma_{\text{tot}}\gamma_m + \Delta\delta_m)]}{\Delta^2 + (\gamma_{\text{tot}} - i\omega)^2} + \frac{2i(\gamma_{\text{sr}}\delta_m + \gamma_m\delta_{\text{sr}})\omega + \delta_m\omega^2}{\Delta^2 + (\gamma_{\text{tot}} - i\omega)^2} \right\} . \quad (5.42)$$

Here, the notation is as follows. The total length of the signal-recycling cavity is  $L$ , which is composed of

$$L = l_{\text{sr}} + L_{\text{arm}} + l \quad , \quad (5.43)$$

where  $L_{\text{arm}}$  is the distance between beam splitter and steering mirrors,  $l_{\text{sr}}$  depicts the distance between signal-recycling mirror and beam splitter.  $l$  is exactly half the distance between the steering mirrors, which corresponds to a dark-fringe here (this can be achieved by an appropriate choice of beam splitter phases). Then, the arm lengths due to membrane displacement  $\delta l/2 = \epsilon$  from dark-fringe are  $l_a = l - \delta l/2$  and  $l_b = l + \delta l/2$ , such that  $l_b - l_a = \delta l$  and  $l_b + l_a = 2l$ . The total cavity linewidth  $\gamma$  is a composition of two terms now [140], given by

$$\gamma_{\text{tot}} = \gamma_{\text{sr}} + \gamma_m \quad , \quad (5.44)$$

where  $\gamma_{\text{sr}}$  and  $\gamma_m$  are the contribution from both the finite recycling mirror and interferometer transmissivity, respectively, and are written as

$$\gamma_{\text{sr}} = \frac{ct_{\text{sr}}^2}{4L} \quad , \quad \gamma_m = \frac{ct_{\text{ifo}}^2}{4L} = \frac{cr_m^2(k_0\epsilon)^2}{4L} \quad . \quad (5.45)$$

Here, the expression for  $\gamma_m$  is derived from Eq. (4.12) for the interferometer close to dark-fringe and with  $2x = \epsilon$ . Equation (5.44) provides an intuitive understanding of why the perfect mirror results in the strongest dissipative coupling: For  $t_{\text{sr}}^2 = 0$ , the contribution  $\gamma_{\text{sr}} = 0$ , and  $\gamma_{\text{tot}}$  is given by the  $\gamma_m$  only. The cavity will be over-coupled for any membrane position. The total cavity detuning  $\Delta$  is defined by

$$\Delta = \delta_{\text{sr}} + \delta_m \quad , \quad \delta_{\text{sr}} = \omega_0 - \omega_c \quad , \quad \delta_m = cr_m t_m \frac{(k_0\epsilon)^2}{4L} \quad , \quad (5.46)$$

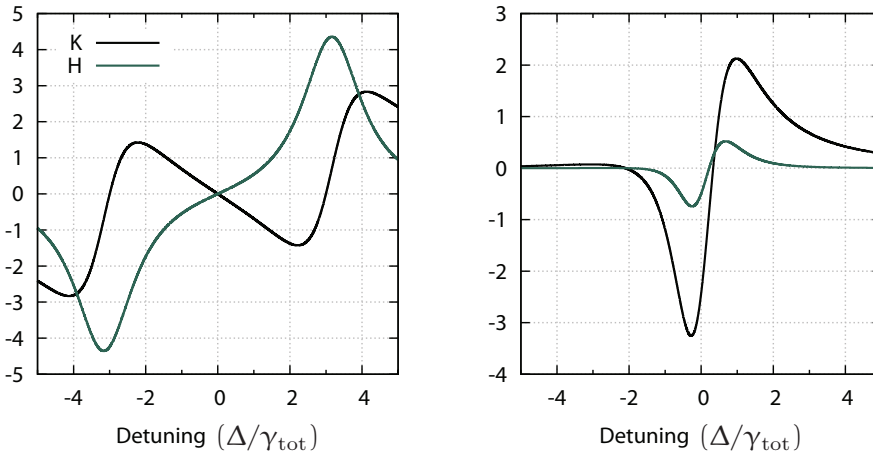


**Figure 5.19:** Real (K, black line) - and imaginary part (H, green line) of the optical spring  $\kappa(\omega)$  in the Michelson-Sagnac interferometer, calculated for  $\omega = \omega_m$ . In the left figure, the membrane position is chosen to coincide with a dark-fringe position,  $\gamma_m = 0$ . The optical rigidity and damping vanishes for  $\Delta = 0$ . Right: interferometer operated with approx.  $1/30\lambda$  dark-fringe offset.

where  $\delta_{sr}$  and  $\delta_m$  are the detuning of the signal-recycling cavity and interferometer respectively.

The optical spring  $\kappa$  for the Michelson-Sagnac interferometer exhibits a more complex shape than that in case of a Fabry-Perot cavity, even with the approximation of close-to dark-fringe operation. It especially depends on both, interferometer detuning from dark-fringe  $\epsilon$  and cavity detuning  $\delta_{sr}$ . Some special cases shall be considered here briefly. Tuning the interferometer to dark-fringe ( $\epsilon = 0 \rightarrow \delta_m = 0$ ) simplifies the Eq. (5.42), such that the expression resembles the ones from the Fabry-Perot cavity. It then exists only one zero-crossing of damping  $\Gamma$ ,  $\Gamma(\omega) = 0 \Leftrightarrow \delta_{sr} = 0$ . This situation is depicted on the left of Fig. 5.19. Thus, for the signal-recycling cavity on resonance and the interferometer precisely on dark-fringe, the oscillator parameters are unmodified by the coupling to the cavity field. Therefore, the noise budget in [86] holds.

For  $\epsilon \neq 0$ , another feature of the coupling becomes evident directly out of Eq. (5.42). Even if the detuning  $\delta_{sr}$  contribution of signal-recycling mirror is zero,  $\delta_{sr} = 0$ , not all terms disappear, implying optical modification of the oscillator on signal-recycling cavity resonance. This is most obvious by the last contribution  $\delta_m \omega^2$  in the imaginary part of the optical spring in Eq. (5.42). This situation is

## 5 Signal-recycled Michelson-Sagnac interferometer

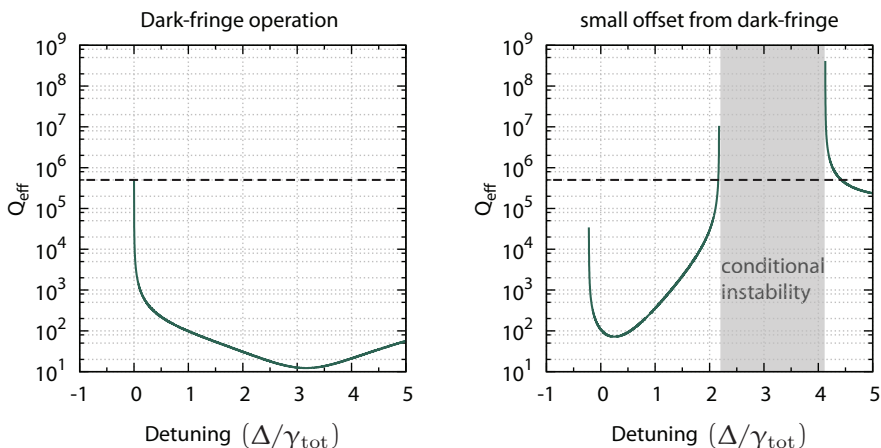


**Figure 5.20:** Numerically calculated modification of the membrane mechanical quality factor due to the optical spring. Here, an optical input power  $P_{\text{in}} = 50$  mW was assumed. Left: Operation on dark-fringe. The quality factor is reduced for positive detunings  $\Delta$ . Right: dark-fringe offset of  $k_{\text{si}} = 0.03\lambda$ . The initial quality factor (shown as dashed line) can be decreased by several orders of magnitude on resonance, e.g.  $\Delta = 0$ . The initial quality factor is depicted as black, dashed line. A region of anomalous (conditional) instability is expected on for  $2\gamma_{\text{tot}} < \Delta < 4\gamma_{\text{tot}}$ .

depicted on the right side in Fig. 5.19.

These exemplary situations highlight the difference to the linear, Fabry-Perot cavity setup, in which the optical spring vanishes on cavity resonance.

### 5.3.4 Conditional instability

For a sufficiently large dark-fringe offset, a second region of anomalous instability is predicted by theory [140, 142] for the (otherwise) damping detuning of the signal-recycling cavity. A comparison of the modified mechanical quality factor for operation on and off dark-fringe is depicted in Fig. 5.20. The anomalous instability occurs in the right figure, in a region of  $2\gamma_{\text{tot}} < \Delta < 4\gamma_{\text{tot}}$ . It is referred to as *conditional* instability in the following context, as it emerges only if the optical input power and the dark-fringe offset of the interferometer exceed a certain threshold.

According to Eq. (5.42), the threshold detuning of the signal-recycling cavity  $\delta_{\text{sr}}$  for this instability depends on the optical input power and the interferometer detuning from dark-fringe. Indeed, this behaviour is observable in the experiment. For a demonstration, the interferom-

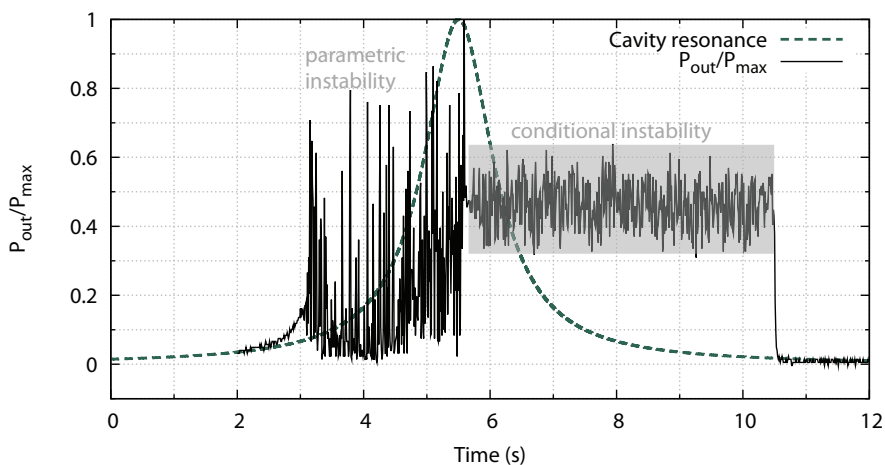


**Figure 5.21:** Instability on both sides of the cavity resonance. The green line is the undisturbed cavity resonance peak (as captured with a fast scan). Grey shows the interferometer output power, normalised to the maximum transmittable power  $P_{\max}$ . The expected instability on the left side of the resonance is observed as well as a second region of conditional instability for the opposite detuning. Here, the input power was  $P_{\text{in}} = 50$  mW.

eter was manually detuned from dark-fringe, and the signal-recycling cavity mirror position was scanned once again with a triangular voltage, applied to the SRM piezo actuator. The output power time series was monitored with the locking photo detector (compare Fig. 5.10). The measurement outcome is depicted in Fig. 5.21.

The green trace shows the unperturbed cavity resonance profile as captured with a high scan velocity (as shown in Fig. 5.11). The grey line depicts the actual measured fraction of output power  $P_{\text{out}}/P_{\max}$  as function of time (cavity detuning from resonance), approaching resonance from the left side. At  $t = 2$  s, the cavity reached the regime of parametric instability, causing an exponential increase of oscillations with the membrane resonance frequency  $\omega_0$ . At  $t = 5.5$  s, the cavity reached resonance (zero detuning). The parametric instability stops instantly, and the oscillator behaviour switches into a self-sustaining oscillation with increased amplitude. During this 'conditional' instability, no exponential amplification is observed, in contrast to the parametric instability for the opposite detuning. The conditional instability is interrupted only by the ongoing shift of the signal-recycling mirror at around  $t = 10.5$  s. The conditional instability can not be produced in a purely dispersive coupling, in which case the damp-

## 5 Signal-recycled Michelson-Sagnac interferometer

---

ing for this sign of the signal-recycling cavity detuning  $\delta_{\text{sr}}$  is always positive, never negative.

During the parametric instability, the time series of the interferometer output power contained a dominant modulation at the frequency of the fundamental mechanical resonance of  $\omega_{\text{m}}/(2\pi) = 133$  kHz. During the self-sustaining conditional instability, the frequency spectrum of the output power time series was dominated by one a multiple of the fundamental mechanical resonance frequency, such that the time series contained a dominant modulation at  $\omega/(2\pi) = n \cdot 133$  kHz, with  $n$  being an integer. For multiple measurements,  $n$  was mostly found within a small interval,  $n \in \{1, 2, 3\}$ . At this time, the exact dynamics causing this behaviour are not fully understood and need to be investigated in more detail, both experimentally and theoretically. It is possible that the effect is in analogy with the so-called *limit-cycle* behaviour [135, 143], known from linear cavity opto-mechanical setups. Here, the threshold of the conditional instability was investigated closer. Therefore, the membrane microscopic position was first chosen to maximize the transmittable output power  $P_{\text{trans}}$  of the cavity while scanning the microscopic position of the recycling-mirror. The cavity resonance profile in transmission of the cavity was monitored continuously with the locking photo detector again.

The scanning of the recycling mirror was stopped, and the SRM position was manually shifted towards cavity resonance by applying a high-voltage to the piezo ceramic transducer of the SRM mirror. Thus, both  $\Delta$  and  $\delta_{\text{sr}}$  were reduced from an initial positive detuning (approaching the cavity from the conditionally stable side of the resonance), and the relative height of the cavity resonance profile was denoted, allowing to calculate the detuning  $\delta_{\text{SR}}$ . This threshold tuning was determined for different optical input powers and interferometer positions. The result is depicted in Fig. 5.22.

Here, different lines correspond to measurements at constant interferometer detuning from dark-fringe (constant  $k_{\text{si}}$ ). The dark-fringe offsets were chosen such as to (first) maximise the transmittable laser power through the system. Then, the dark-fringe offset was reduced to transmit a half (quarter) of the maximum transmittable power. For each input power and dark-fringe offset, the green areas indicate an area of conditional instability. On the right side of the figure, the relative height was converted to corresponding total detuning  $\Delta$  in units of the total cavity linewidth  $\gamma_{\text{tot}}$ . The existence of the conditional instability confirms the theoretical prediction qualitatively. However,



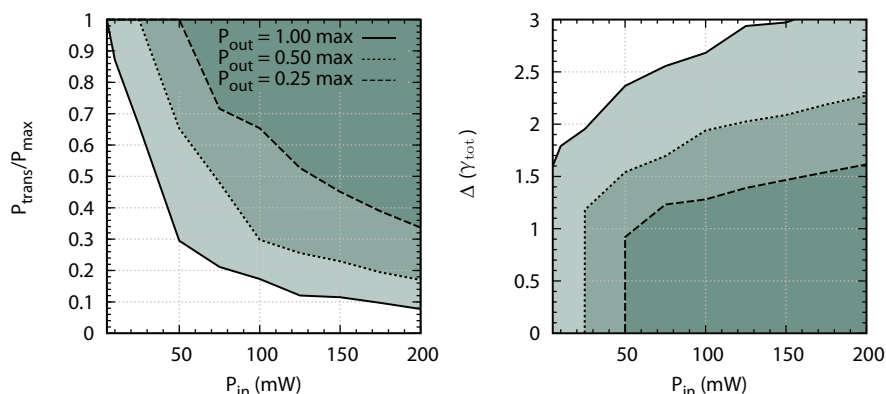


**Figure 5.22:** Measured threshold of the signal-recycling cavity detuning for the conditional instability. Lines are used to indicate measurements at a particular interferometer offset from dark-fringe (constant  $k_{si}$ ). Green areas depict regions of conditional (anomalous) instability. Right: Conversion of the left data into total detuning  $\Delta$ , given in units of total linewidth  $\gamma_{tot}$ .

a quantitative comparison of experimental data for the threshold and the numerically calculated values is the subject of ongoing research.

To summarise this section, it can be stated that lock acquisition of the cavity is possible but non-trivial. The error-signal for the cavity lock becomes meaningful (exhibits the right sign) only within the cavity linewidth (see Fig. 5.12). Tuning the cavity length to resonance manually from a far detuned state is not possible if the combined input power and dark-fringe offset of the interferometer will result in a conditional instability, before the cavity is resonant. Approaching the resonance from an opposite, far detuned state will encounter the parametric instability before resonance is reached. The huge amplitude of the increasing oscillation was found to saturate the mixer electronic and thereby spoofing the error-signal.

A possible solution for high optical input powers with non-vanishing dark-fringe offset might be to make the cavity resonant with a low optical input power and to switch on the stabilisation. In this state, it should be possible to increase the input power, such that instabilities would occur for the detuned cavity, but since the cavity is already resonant (tuned) there is no need to leave resonance. This method would require an adaptable gain in the electronic feed-back to initiate the lock with low input powers ( $P_{in} < 10$  mW), which then needs to be reduced when increasing the optical gain by a higher input power.

## 5 Signal-recycled Michelson-Sagnac interferometer

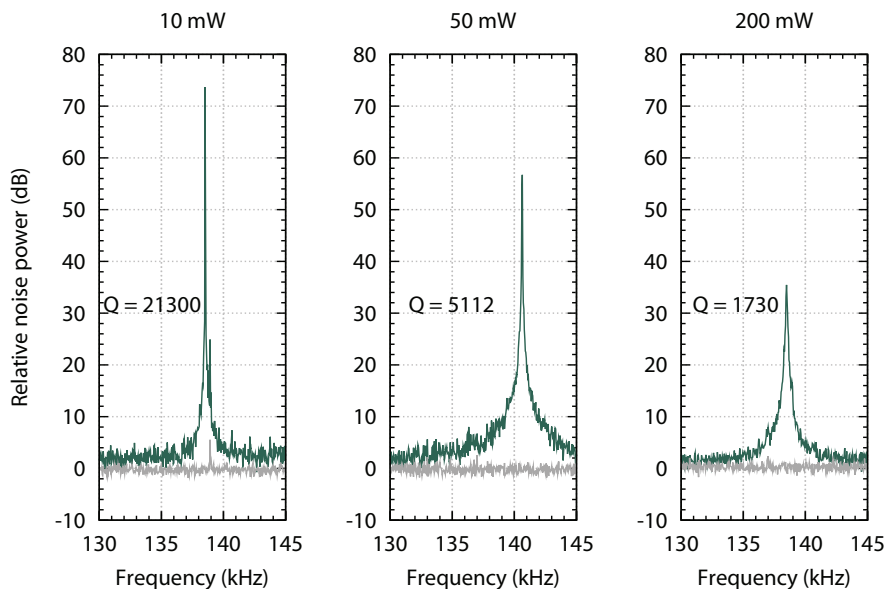


**Figure 5.23:** Interferometer output power spectra (green lines) around the mechanical resonance frequency for different optical input powers  $P_{\text{in}}$ . The noise level were normalised to the individual, measured shot noise level (plotted in grey). The effective quality factor  $Q_{\text{eff}}$  was inferred from the FWHM of the mechanical resonance.

The realisation of such an electronic feed-back is feasible and should then allow to operate the experiment precisely on resonance. For the interferometer on dark-fringe and operation precisely on cavity resonance, the optical spring is 'switched off' and the quantum noise calculations in [86] hold.

### 5.3.5 Observation of optical damping

When increasing the optical input power  $P_{\text{in}}$ , the shape of the mechanical resonance in the interferometer output spectrum was broadened, indicating optical damping as expected from the complex optical spring Eq. (5.42). Moreover, the signal to shot noise ratio seems reduced, even though the optical input power was increased. This was attributed to the effect of optical cooling to an effective temperature  $T_{\text{eff}} < T_{\text{ini}} = 300$  K, as is anticipated from Eq. (5.40). Interferometer output spectra for three different optical input powers are shown in Fig. 5.23.

The FWHM of the resonances was inferred from the measured output

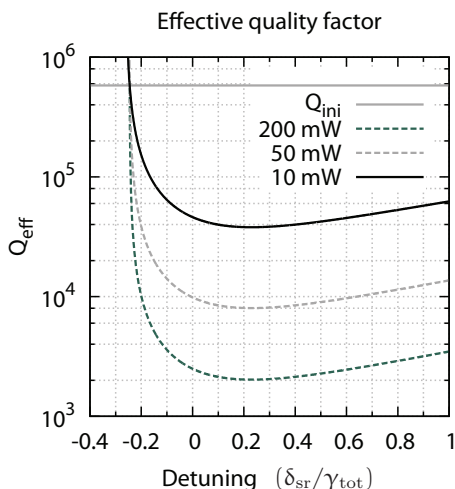


**Figure 5.24:** Calculated effective quality factor  $Q_{\text{eff}}$  as function of signal-recycling detuning  $\delta_{\text{sr}}$  in units of total cavity linewidth  $\gamma_{\text{tot}}$ . The optical damping is calculated for three different optical input powers  $P_{\text{in}} = 10 \text{ mW}$ ,  $50 \text{ mW}$  and  $200 \text{ mW}$  with an interferometer arm length imbalance of  $0.0125\lambda$ . An optical loss of 1% was taken into account. For  $P_{\text{in}} = 200 \text{ mW}$ ,  $|\delta_{\text{sr}}| \leq 0.1\gamma_{\text{tot}}$ , an effective quality factor of approximately 2300 is expected.

spectra, allowing for a direct determination the mechanical quality factor by Eq. (3.17). Because of high initial quality factor, this method is less reliable for small damping because of the absolute error due to the minimum frequency resolution of 1 Hz of the spectrum analyser. For a quality factor of  $5.8 \cdot 10^5$  and a resonance frequency of  $f = 130 \text{ kHz}$ , the FWHM is 224 mHz.

To obtain the spectra, the signal-recycling cavity was locked on cavity resonance,  $\delta_{\text{sr}} \leq 0.1\gamma_{\text{sr}}$ . In case of  $P_{\text{in}} = 200 \text{ mW}$ , it was not possible to lock the cavity precisely on resonance, despite an appropriate error signal with correct offset (as shown in Fig. 5.12). If locked with a 100 mV pk-pk error signal, a non-vanishing error of  $V_{\text{lock}} = 10 \text{ mV}$  was noticed during lock and could not be reduced by a higher control-loop gain, nor by an increased control loop bandwidth. The signal-recycling cavity was thus detuned by about  $160 \text{ kHz} \approx 0.1\gamma_{\text{sr}}$ . It is possible that this effect was related to the optical spring, which pre-

**Table 5.1:** Determined mechanical quality factors for different optical input powers  $P_{\text{in}}$  with an arm length imbalance of  $k_{\text{si}} = 0.0125\lambda$ . An absolute measurement error of  $\pm 2\text{Hz}$  causes a minimum and maximum effective quality factor  $Q_{\text{eff}}^{\text{max}}$ ,  $Q_{\text{eff}}^{\text{min}}$

$P_{\text{in}}$	FWHM	$f_{\text{res}}(\text{kHz})$	$Q_{\text{eff}}$	$Q_{\text{eff}}^{\text{min}}$	$Q_{\text{eff}}^{\text{max}}$
10 mW	6.5 Hz	138.5	21307	16235	30666
50 mW	27.5 Hz	140.6	5112	4766	5513
200 mW	80 Hz	138.4	1730	1687	1774

## 5 Signal-recycled Michelson-Sagnac interferometer

---

vents operation precisely on cavity resonance. This seems conceivable because this detuning bears resemblance to the membrane mechanical resonance frequency.

The setup for the measurement is shown in Fig. 5.10. The output power spectra were analysed with the balanced homodyne detector in transmission of the cavity. Thereby, the full laser power was avoided on the detector, which would be the case for a detection in reflection of the cavity. All spectra were limited by optical shot noise. According to Eq. (5.40), a reduced quality factor is associated with a reduced, effective temperature  $T_{\text{eff}}$ . When laser noise is neglected, this allows to calibrate the spectrum to  $\text{m}/\sqrt{\text{Hz}}$ , as the displacement noise close to the mechanical resonance has to match the predicted thermal noise. Then, the relative shot noise level is determined as thereby. It was found at  $8.0 \cdot 10^{-16} \text{ m}/\sqrt{\text{Hz}}$ , and therefore higher than the value that was estimated from the model presented in Sec. 5.2.3. This was attributed to the dark-fringe offset of the interferometer, which results in an over coupled signal-recycling cavity and thereby reduced the signal-recycling gain significantly. However, an independent calibration is required in a future setup. Here, the calibration follows out of  $T_{\text{eff}} \approx 1 \text{ K}$  and Eq. (5.40).

An accordingly calibrated interferometer output spectrum for an input power of  $P_{\text{in}} = 200 \text{ mW}$  is depicted in Fig. 5.25. It shows the interferometer output spectrum around the fundamental resonance of the membrane, which was increased by about 5 kHz (3.8% of the initial frequency). The orange line depicts thermal noise of the membrane with  $T_{\text{eff}} \approx 1.0 \text{ K}$  and  $Q_{\text{eff}} \approx 1730$ . The measured mechanical quality factors are in reasonable agreement with the theoretical prediction, if optical loss is considered and given the uncertainty of the experimental parameters. Also, the interferometer was not locked during these measurements. Instead, a constant dark-fringe offset during the measurements was ensured by scanning the position of the signal-recycling mirror before and after the measurement of the spectrum. Subsequently, the cavity resonance output power profiles were compared measurements were. In the case of same mean membrane position, the maximum transmitted power through the cavity is the same. The calculated optical damping for this particular optical input power is shown in Fig 5.24. The resulting shot noise level is higher than the value derived in Sec. 5.1.4. This was attributed to the fact that the measurements were taken with a small dark-fringe offset and

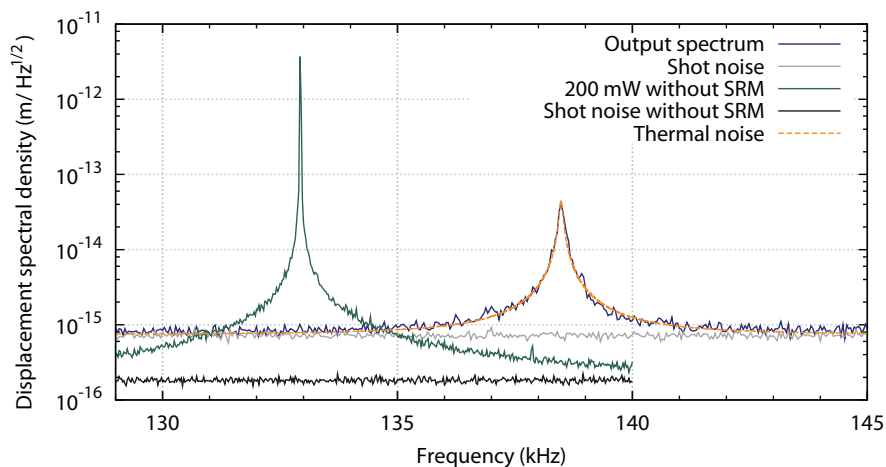


**Figure 5.25:** Calibrated output power spectrum with (blue trace) and without signal-recycling mirror (green trace). In the first case, the cavity was close to resonance  $\delta_{\text{sr}} < 0.1\gamma_{\text{tot}}$ . The mechanical resonance is clearly broadened. The resonance frequency is increased due to the ordinary long-term drift of the mechanical resonance. The sum of shot noise (grey trace) and thermal noise of the oscillator is depicted as orange, dashed line. The effective quality factor was  $Q_{\text{eff}} \approx 1730$ , corresponding to  $T_{\text{eff}} \approx 1.0$  K. The relative shot noise level then yields  $8.0 \cdot 10^{-15} \text{ m}/\sqrt{\text{Hz}}$ .

to the impedance mismatch of the cavity due to internal optical loss. In the measurement, the resonance frequency of the fundamental oscillation mode was shifted by about 3 kHz towards higher frequencies. The difference to the measured resonance frequency without the recycling mirror is not caused by the optical spring, but by long-term drifts of the resonance. The resonance frequency of the investigated SiN membrane is long-term stable only to a fraction of about few percent and is influenced, for example by laboratory conditions such as temperature. However, no perceivable influence on the mechanical quality factor of a SiN membrane was observed in all previous measurements.

### Comment about the marker peak

The marker-peak method was not used to calibrate the spectra because its displacement varied in an unpredictable manner. In particular, the signal-to shot noise level of the marker was reduced for higher optical input powers, indicating that the excitation of the membrane center of mass had changed - otherwise, this effect is unexplainable.

## 5 Signal-recycled Michelson-Sagnac interferometer

---

This was interpreted as follows: The excitation for the calibrated marker was not directly given to the membrane fundamental mode (as this is not possible), but instead was applied to the piezo indirectly connected to the silicon frame. In presence of a strong optical spring with perceivable suppression of membrane motion (optical damping), the frame might still perform the same movement but the membrane center does not. Since only the membrane displacement is read out, the marker peak will not be a reliable calibration method. If this explanation is correct, a possible solution is to actuate not the membrane (as it is subject to the optical spring), but introduce a signal by actuating one of the steering mirrors instead. The effect of the optical spring to this massive object is expected small, such that it could provide a more reliable and independent calibration method.

### 5.3.6 Reduction of interferometer loss

If the optical losses within the interferometer can be reduced by one order of magnitude to about 0.1 %, an even stronger optical damping (and cooling) is expected. Such loss should be feasible given the considerations in Sec. 5.1.5. In the case of this loss value, the effect of the optical spring on the effective mechanical quality factor and the mechanical resonance frequency is shown in Fig. 5.26. Here, different values for  $\kappa_{\text{si}}$  are considered to illustrate the emergence of the conditional instability. The right subplot depicts the induced frequency shift of the mechanical resonance, which is found approximately 1 kHz around zero detuning of the signal-recycling cavity  $\delta_{\text{sr}}$ .

A minimum value for  $Q_{\text{eff}} \approx 20$  is achieved for a detuned signal-recycling cavity in the case of operation on dark-fringe. For a dark-fringe offset of ( $\kappa_{\text{si}} = 0.005 \lambda$ ), the effective quality factor on signal-recycling cavity resonance is reduced to about 60, a reduction of about 4 orders of magnitude. The achievable temperature in this case would be estimated according to Eq. (5.40) to  $T_{\text{eff}} = 30$  mK, which, in turn results in a mean occupation number oscillator occupation number of (compare Eq. (6.3)) of  $\bar{n} = \kappa_{\text{B}} T_{\text{eff}} / (\omega_{\text{m}} \hbar) \approx 4718$ , in the case of an initial oscillator temperature of  $T = 300$  K (room temperature). Conducting the experiment at cryogenic temperatures can decrease this number significantly. Subsequently, the application of cryogenic cooling is presented in the next chapter.

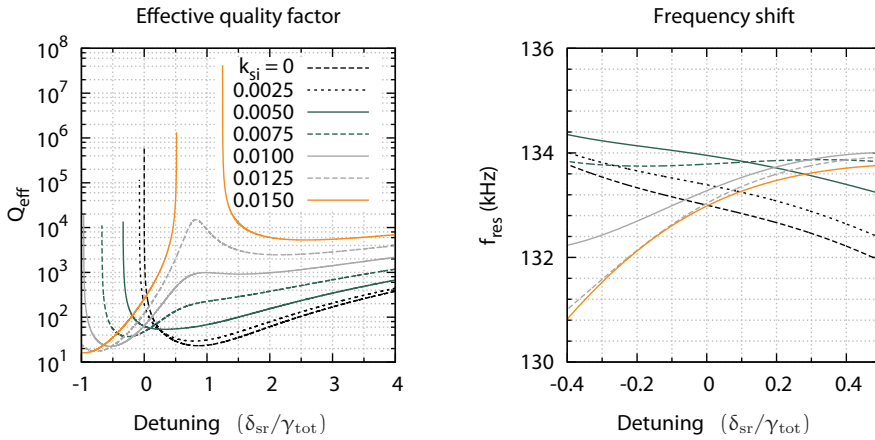


**Figure 5.26:** Modification of the mechanical quality factor with 0.1% optical loss within the interferometer for different values of  $k_{\text{si}}$  in units of wavelength  $\lambda$ . Here,  $P_{\text{in}} = 200$  mW,  $Q_{\text{ini}} = 5.8 \cdot 10^5$  and  $\omega_{\text{m}}/(2\pi) = 133$  kHz are assumed. The abrupt end of the traces in the left figure is due to the method of the numerical calculation.

## 5.4 Chapter summary

This chapter described the principle of opto-mechanics in the example of a two-mirror linear cavity and summarised definitions to describe this arrangement. An effective cavity, established by placing a high-reflective mirror in the Michelson-Sagnac interferometer output was investigated with regard to the cavity transfer functions, both for external as internal (signal) input. A model to estimate the impact of optical loss was introduced, and its implications to the (recycled) interferometer sensitivity was discussed. The chapter also presents the experimentally realised cavity setup and explains the locking scheme used to keep the cavity resonant for the laser field. The opto-mechanical interaction in the signal-recycled Michelson-Sagnac interferometer exhibits multiple features known from linear, Fabry-Perot type opto-mechanical experiments. Thus, both setups were compared with regard to their individual optical spring. The theoretical model for the optical spring was tested and qualitatively confirmed by observing a conditional instability on the (otherwise) cooling side of the signal-recycling cavity resonance. This instability is both dependent on the interferometer offset from dark-fringe as on the input laser power. The mechanical resonance was broadened in the interferometer output spectra for high optical input powers, as expected from additional optical damping due to the complex optical spring. From

## 5 Signal-recycled Michelson-Sagnac interferometer

---

the FWHM of the mechanical resonance, a minimal effective quality factor of  $Q_{\text{eff}} = 1730$  could be inferred, which is in good agreement with the theoretical prediction of  $Q_{\text{eff}}^{\text{calc}} = 2300$ . In contrast to previous experiments [111], a balanced homodyne detector was used for read out, and it could be confirmed that the spectra were limited by optical shot noise.



# 6

## Chapter 6

# Cryogenic cooling of the interferometer

This chapter addresses the effort of operating a Michelson-Sagnac interferometer at cryogenic temperatures and associated experimental challenges. The cryogenic system, its function principle and an custom interferometer prototype for operation at cryogenic temperatures are presented. The chapter closes with the presentation of membrane displacement spectra at temperatures below 10 K and an overview about identified problems and possible solutions.

## 6.1 The need for low temperatures

In a situation in which the interferometer is limited by the thermal noise of the oscillator (compare Fig. 4.29), the application of cryogenic cooling can cause a significant enhancement of the displacement sensitivity. This is of particular interest when the measurement precision is to be increased by signal-recycling, as the measurement will be limited by the phase fluctuation caused by thermally excited motion of the membrane long before radiation pressure effects will be observable. The ratio of thermal noise to radiation pressure noise can be derived from Eq. (3.25) and Eq. (4.26), yielding

$$\sqrt{\frac{G_{\text{therm}}^{\text{vis}}}{G_{\text{rpn}}}} = \sqrt{\frac{mk_{\text{B}}T\omega_0/Q}{4\pi\hbar r_m^2 G_{\text{sr}}P_0/(c\lambda)}} \propto \sqrt{\frac{T}{Q}} \quad (6.1)$$

For a realistic scenario ( $r_m^2 = 0.3$ ,  $\omega_0/(2\pi) = 75$  kHz,  $m = 125$  ng) and experimental parameters, their ratio is given by

$$\sqrt{\frac{G_{\text{therm}}^{\text{vis}}}{G_{\text{rpn}}}} = 442.5 \cdot \sqrt{\frac{1 \text{ W}}{P}} \sqrt{\frac{\lambda}{1064 \text{ nm}}} \sqrt{\frac{10^6}{Q}} \sqrt{\frac{T}{300 \text{ K}}} \sqrt{\frac{1}{G_{\text{sr}}}} \quad (6.2)$$

For the reasons discussed in Section 5, the signal-recycling gain will be limited and probably  $\sqrt{G_{\text{sr}}} < 30$ . Without significant enhancement of the input power (power-recycling), and for typical laser wavelengths  $532 \text{ nm} < \lambda < 1550 \text{ nm}$ , achieving a unity ratio is rendered impossible at room temperature.

### 6.2 Concepts for cryogenic cooling

Cryogenic cooling can be provided in several ways, and there are various cryogenic topologies for manifold experimental situations [144]. The choice of which cryogenic system to use depends on several aspects. Obviously, the minimal achievable temperature is important, but the complexity of the cryogenic system itself and the effort to operate it also impact the decision. Operation and maintenance costs are to be considered as well.

Usage of ultra cold gases, such as  $^4\text{He}$  or its rare, much more expensive isotope  $^3\text{He}$  allow for temperatures below 4 K and  $< 300 \text{ mK}$ , respectively. Modern dilution refrigerators also allow for a 'dry operation', without the need of external supply of liquid gases, which simplifies their application as infrastructural requirements are eased, e.g. no helium gas recovery lines and collecting is necessary. However, pumps and compressors are still required. These components typically contain moving parts and produce noise and vibrations, which are to be kept to a minimal when performing low frequency ( $f \leq 10 \text{ kHz}$ ), high precision measurements nearby.

Thus, application of cryogenic cooling in gravitational wave detectors is still uncommon. Future gravitational wave detectors are expected to be limited by mirror thermal noise in their most sensitive frequency region however (compare the anticipated noise budget of the advanced LIGO detector in Fig. 1.1). For this reason, the usage of cryogenic temperatures in a GW detector will be realised in the Japanese KAGRA [145] detector for the first time. Beyond this, temperatures of around 10 K are also anticipated for the Einstein telescope [146] to overcome sensitivity limitations caused by thermal noise.

In opto-mechanical experiments, cryogenic cooling is well-established. This is mainly due to two reasons. First, the majority of these exper-

iments typically operate at very high frequencies  $f > 100$  kHz, where mechanical disturbances less likely degrade the measurements outcome. And second, the required setups are often times very compact in size, such that the working volume of the cryogenic system can be kept small or designed to only cool the micro-mechanical oscillator. One major motivation for cryogenic cooling in opto-mechanical experiments is to achieve the mechanical ground state of a mechanical oscillator, e.g. a small phonon occupation number  $n$ . For a harmonic oscillator of resonance frequency  $\omega_0$  and temperature  $T$ , the occupation number is given by

$$E = n\hbar\omega_m = k_B T \Leftrightarrow n = \frac{k_B T}{\hbar\omega_m} . \quad (6.3)$$

Per definition, the mechanical ground state of motion is reached when  $\bar{n} < 1$  is fulfilled. Considering Eq. (6.3) it is not surprising that the first micro-oscillator brought to its mechanical ground state had a resonance frequency of  $\omega_m/(2\pi) = 6$  GHz [51]. For this frequency, the system is in its ground state for temperatures  $T < 280$  mK, a temperature one order of magnitude larger than state-of-the-art dilution-refrigerators base temperatures of about 20 mK and two orders of magnitude higher than the base temperature reported in [147]. For an extended overview about cryogenic methods the reader is referred to [148].

For oscillators with lower resonance frequencies (such as in [149]), the ground state is not achievable by pure coupling to the ultra cold heat bath supplied by the cryostat. Instead, the ground state can be reached by a combination of cryogenic assisted resolved optical side-band cooling techniques [49, 50]. Optical cooling in the unresolved side band regime can also lead to close-to ground state occupation numbers [53].

### 6.3 The Gifford-McMahon cryocooler

During this thesis, and within a supervised masters thesis [150], a first cryogenic system for operation of a Michelson-Sagnac interferometer at low temperatures has been set up at the Albert-Einstein Institute (AEI). The system is a custom made, closed cycle  $^4\text{He}$  cryocooler by *Jannis Research* [151]. It uses a two-staged Gifford-McMahon [152–154] thermodynamic cycle [144, 155, 156]. By controlled compression and expansion of an ideal gas (here, helium), a base temperature of

## 6 Cryogenic cooling of the interferometer

---

6 K is achieved. A review about the state of art cryocoolers is given in [157]. Their principle of operation can be understood when recalling the ideal gas law

$$pV = nRT \quad , \quad (6.4)$$

where  $p$  is the pressure,  $V$  is the volume,  $n$  is the amount of substance,  $T$  is the temperature and  $R$  the universal gas constant. Equation (6.4), which can be used to understand individual steps of the cryocooler's thermodynamic cycle.

### 6.3.1 Thermodynamic cycle

This section outlines the working principle of the Gifford-McMahon cryocooler and its thermodynamic cycle. The system is composed of a closed volume (cold head) and a motorized displacer unit, which separates the volume into two parts (which will be referred to as cool and warm side of the volume). The displacer is tight, such that gas can only be exchanged via the so-called regenerator in the displacer. Moreover, the warm side can be selectively connected to a high pressure reservoir of gaseous helium at 200 bar ( $P_2$ ) or atmospheric pressure ( $P_1$ ). A schematic of the cold head is depicted in Fig. 6.1 a). GM cryocoolers are simple, cost efficient devices with a high reliability, as there are few, slow moving parts at room temperature. Generally they are cheaper than pulse type cryocoolers, but exhibit a higher vibration level due to the moving mechanical displacer unit. Vibrations caused by the expansion and compression of the gas inside are present in both types, however.

The system undergoes a thermodynamic cycle which can be split into four consecutive steps c) - f) , which will be described briefly in the following and are depicted in Fig 6.1.

- c) The displacer is on the left side of the cold head, the high pressure valve is opened. Gas streams into the volume and is stored on the right (warm) side of the cold head. The pressure is increased from  $P_1$  to  $P_2$  at constant volume, such that according to Eq. (6.4) the temperature of the gas must increase. The water cooling of the compressor is used to cool the gas.
- d) With the high pressure valve opened, the displacer is moved to the right side. The working volume (on the left, cool side) is maximised, the gas streams through the regenerator. The pressure

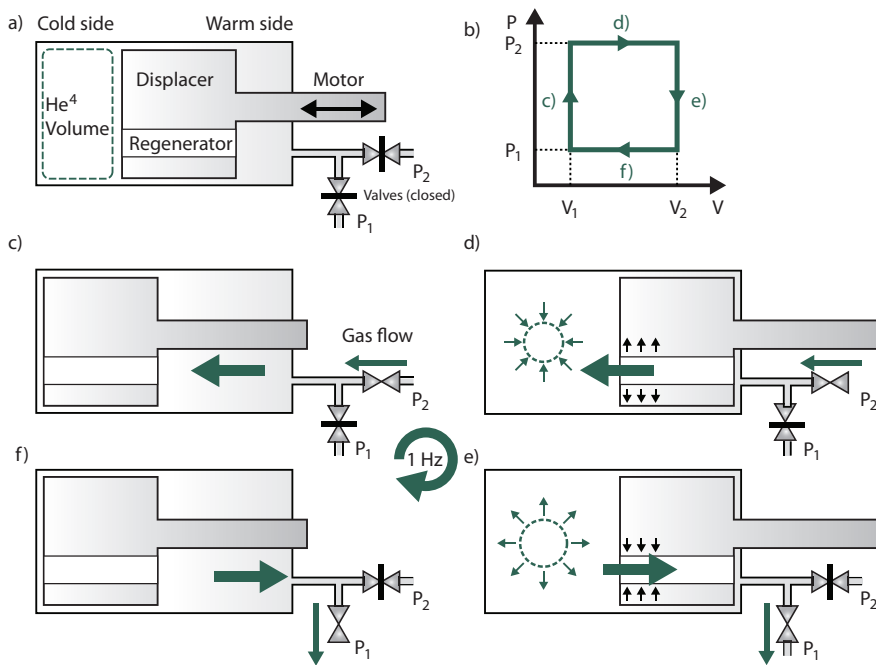


**Figure 6.1:** a) The cold head. A motorised displacer contains the regenerator, through which gas can flow from the left-sided volume to the right. Two valves allow for high or atmospheric pressure inside the cold head volume. b) pressure-volume plane and Gifford-McMahon cycle. c) - e) represent different situations in the cycle.

remains constantly high during this step. When the gas passes through the regenerator, a part of its heat energy is stored in the regenerator.

- e) Now, the high pressure valve is closed and the low pressure valve is opened. The gas on the left side is cooled, because the pressure drops at constant volume, such that its temperature is further decreased. A part of the gas flows through the regenerator in reverse direction and extracts some heat energy out of the regenerator, the regenerator is slightly cooled.
- f) With the same, low-pressure valve opened, the displacer is now moved back to the left side, minimizing the working volume. More exhaust gas is flowing through the regenerator, taking some heat energy out of the latter. The cycle is in the initial state and can start over again from state c). The entire cycle repeats with a frequency of 1 Hz.

## 6 Cryogenic cooling of the interferometer

---

It can be shown [158, 159], that the total refrigeration  $Q$  of the cycle is

$$Q = \oint V dP = \oint P dV = V(P_2 - P_1) \quad , \quad (6.5)$$

where  $P_2$  and  $P_1$  are high and low pressures and  $V$  is the working volume inside the cold head.

### 6.3.2 Cryocooler components

This section briefly outlines all components required to operate the cryocooler. A schematic of the setup is shown in Fig. 6.2.

**Cold head** As described, the cold head consists of a motorized displacer unit with integrated regenerator. An inlet and an outlet valve connect the room temperature side of the cold head with the compressor unit.

**Vibration isolation stage** Cold head and vacuum stage are connected via a passive isolation stage of rubber bellows as depicted in Fig. 6.2. Internal heat links are flexible, such that no rigid connection is required to establish a thermal contact between the cold stages and the sample stage. During operation, the cold head is fixed rigidly to a massive superstructure of *Item* profiles with no connection to the optical table. To open the vacuum chamber, the cold head and vacuum stage are fixed with steel spacers, and the connection to the superstructure is released. Thus lifting the cryocooler by means of a crane is possible. A similar vibration isolation has been developed for CLIO, a precursor of KAGRA [160].

**Exchange gas** Purified helium 4.6 (purity > 99.996%) was used as exchange gas. To avoid contamination of the system, the cold head had to be evacuated to  $10^{-2}$  mbar before inlet of the helium.

**Regenerator** The regenerator consists of a porous or granular material with small flow resistance and ideally no thermal conductivity in flow direction. Lead was formerly used, but modern regenerators use lanthanide materials like  $\text{Er}_3\text{Ni}$  or  $\text{HoCu}_2$ , which are well suited due to their high heat capacity [161].

**Compressor unit** A compressor unit was used to recycle the exhaust, low-pressure gas from the cold head. The compressor type was a

## 6.4 Interferometer prototype for cryogenic environment

---

HC-4E1 from *Sumitomo*. It also filtered the helium gas to eliminate residual oil. The compressor itself required water cooling to avoid overheating.

**Heat shield** A metallic shield protects the inner part of the vacuum chamber from heat radiation of the 'hot' outside walls. It contains two small holes to allow the laser light to reach the centre of the chamber. The shield is connected to the first cold stage at 60 K, such that before the interferometer is brought in thermal contact with the cold finger residual gas will condensate on the heat shield, instead of the interferometer optics.

**Vacuum system** To provide the required vacuum level, a combination of three pumps was used. A *Variant TriScroll 300* scroll pump provided pre vacuum of  $10^{-2}$  mbar to operate a second, turbo molecular pump. This unit was a *Pfeiffer Vacuum HiPace 300*, providing a pressure of  $10^{-5}$  mbar due to the limited cross section of the only available connection to the vacuum chamber. An ion getter pump was used to keep the vacuum level with the mechanical pumps switched off to avoid vibrations. The pressure inside of the vacuum tank was monitored with a combined Penning/ Pirani gauge PTR 90 from *Oerlikon Leybold*.

**Temperature controller** When started, the cryocooler begins to cool down the low temperature side of the cold head, until the minimal base temperature is reached. The temperature of the cold finger is measured with a calibrated silicon diode attached to the sample holder and can be displayed or stabilised to a desired working temperature. The controller unit is a Model 335, manufactured by *Lake Shore Cryogenics Inc.* An integrated PID feedback control loop contacts the cold finger thermally to room temperature, if necessary, and thereby actuates the temperature.

## 6.4 Interferometer prototype for cryogenic environment

The design of the prototype interferometer for operation at cryogenic temperatures was based on the experience with the initial experiment. A compact and stable configuration was desired. It was decided not only to cool the membrane, but the entire interferometer, including

## 6 Cryogenic cooling of the interferometer

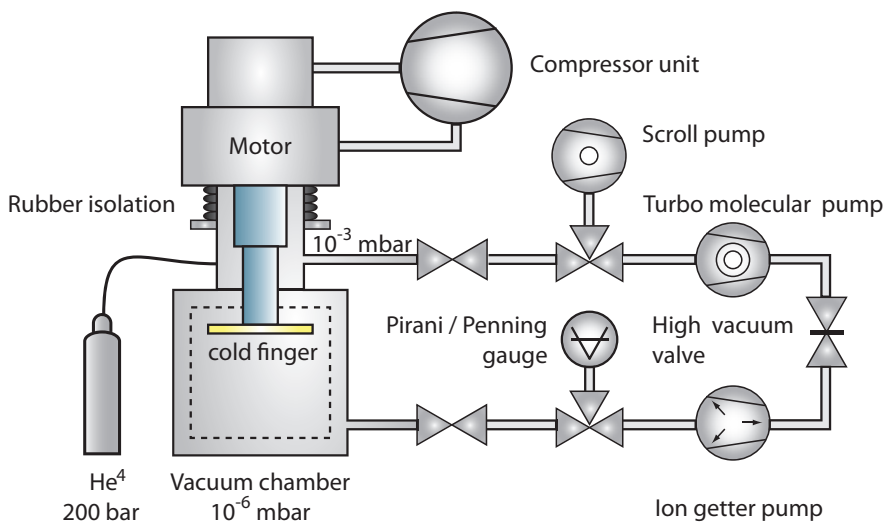


**Figure 6.2:** Schematic of the cryogenic system. A compressor is used to recycle the exhaust helium from the cold head. The motor and cold head are separated against the lower (vacuum stage) by a rubber isolation and fixed to an external superstructure of *item* profiles. The heat shield is depicted as dashed black line. The cold plate is depicted gold. A combination of scroll, turbo pump and ion getter pump provides the necessary vacuum level, which was measured with a combined Pirani/Penning gauge.

all optics and the interferometer baseplate in order to eliminate heat radiation from close-by components to the membrane. Such effect has shown to limit the achievable base temperature in other experiments, for example in [130]. The heat transfer rate per unit area  $\dot{Q}/A$  caused by heat radiation of a nearby component of area  $A_1$  can be calculated with the modified Stefan-Boltzmann law [144] to be

$$\frac{\dot{Q}}{A_1} = F_{12}\epsilon_{12}\sigma(T_1^4 - T_2^4) \quad , \quad (6.6)$$

where  $T_1$  and  $T_2$  are the temperatures the two surfaces and  $F_{12}$  is a configuration factor relating the two surfaces.  $\epsilon_1$  is the emissivity of surface 1 ( $\epsilon = 1$  is a perfectly reflective surface,  $\epsilon = 0$  corresponds to a perfect black-body radiator) and  $\sigma$  is the Stefan-Boltzmann constant. If geometrical aspects shall be left out, it becomes clear from equation (6.6) that, if possible, all components should be cooled, such that no or little net heat flow is present.

Due to the cryocooler layout, the interferometer had to be attached



## 6.4 Interferometer prototype for cryogenic environment

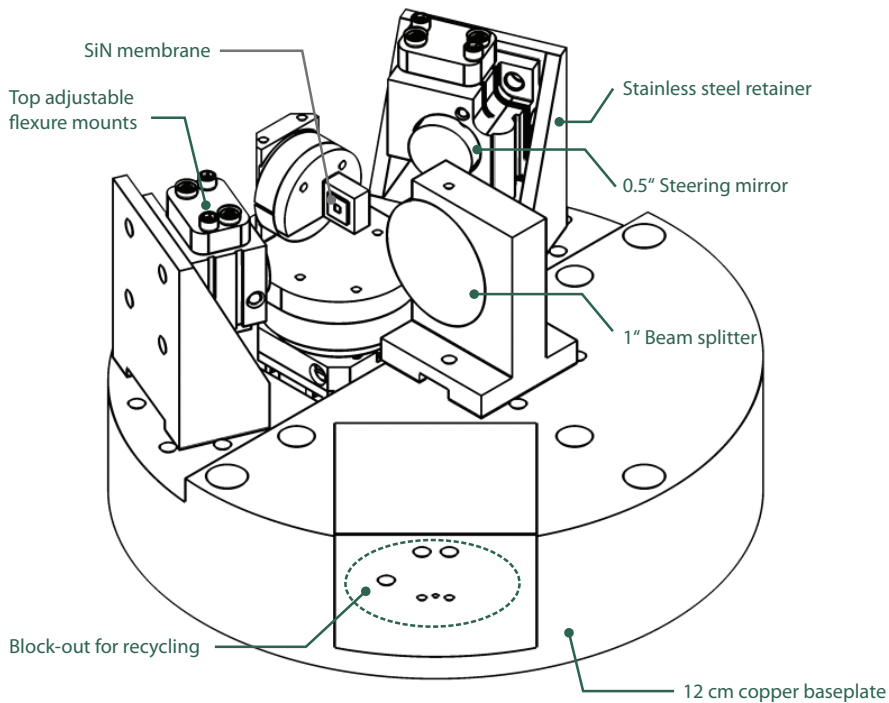


**Figure 6.3:** CAD design of the low-temperature Michelson-Sagnac interferometer prototype. The interferometer baseplate is a 5 cm thick plate of de-oxidized copper, with 12 cm diameter. The steering mirrors are mounted in *Siskyou* top adjustable flexure mounts. The central beam splitter is rigidly mounted into a custom holder and has a diameter of 2.54 cm.

upside down to the cold-plate of the cryocooler. Copper was chosen as baseplate material due to its good thermal conductivity.

### 6.4.1 Membrane alignment and positioning

Positioning and aligning the membrane is crucial. Three essential requirements were to be met. First, the membrane had to be replaceable (as in all experiments). Moreover, the membrane holder must allow for fine alignment of the membrane in order to overlap Sagnac and Michelson mode of the interferometer and, third, it had to be possible to shift the membrane along the beam path to 'scan' an interferometer fringe. Since standard piezo ceramic transducers are not specified for operation at low temperatures, it was decided to use a stack of three *Attocube* positioners. The lowest positioner in this stack is a linear stepper/ scanning stage ANPx101. A rotation stage ANR101

## 6 Cryogenic cooling of the interferometer

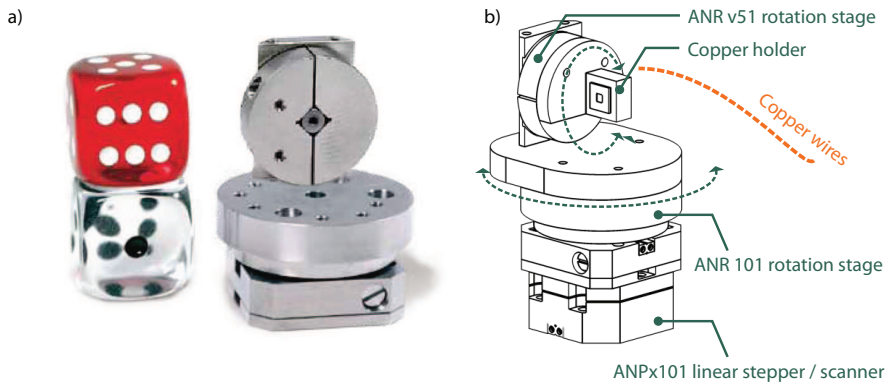


**Figure 6.4:** Left: *Attocube* positioner stack. Right: The membrane is glued on a copper holder, which is connected to the cryocooler cold plate by copper wires. Two remote controllable *Attocube* positioners allow for adjusting the orientation of the membrane in pitch and yaw. A third linear stage below allows to scan and step the membrane along the direction of the beam.

is mounted on top, allowing for rotation in the plane of the interferometer baseplate (yaw) and, finally, another rotation stage ANRv51 allowed for pitch alignment. The two rotation stages are depicted in Fig. 6.4. The positioner specifications are given in Table 6.1.

The use of piezo actuators between the interferometer baseplate and the membrane was expected to provide poor thermal conductivity and reduced thermal contact between the interferometer baseplate and the membrane. The best cooling was expected for a direct connection from the membrane to the cold plate. Thus, the membrane was finally mounted on a small holder made of copper, which was connected to the cold stage directly by several copper wires. The mount contained a cone-shaped drilling on the back side to avoid beam clipping.

The *Attocube* positioners were found to introduce a significant noise level because of the noise in the applied high-voltage. Without electronic low-pass filtering, the output spectra were spoiled by the positioner noise. The controller unit *ANC300* provides two integrated low-pass filters with corner frequencies of 16 Hz and 160 Hz respectively, which provided a sufficient noise suppression and thus had to be enabled during measurements of the interferometer output spectrum.

## 6.4 Interferometer prototype for cryogenic environment

**Table 6.1:** *Attocube* remote positioner data for membrane alignment and positioning at cryogenic temperatures [162]

		ANP <sub>x</sub> 101	ANR101	ANRv51
		linear	rotation	rotation
travel range		5 mm	360°	360°
min. step size	@ 300 K	50 nm	1 m°	1 m°
min. step size	@ 4 K	10 nm	0.5 m°	0.5 m°
scanning range	@ 300 K	≤ 5 μm	≤ 70 m°	≤ 40 m°
scanning range	@ 4 K	≤ 0.8 μm	≤ 14 m°	≤ 6 m°
resolution		sub- nm	μ°	μ°
load capacity		100 g	100 g	30 g

### 6.4.2 The optical setup

SiN membranes were investigated for their optical absorption at different laser wavelengths in [163]. It was found that the minimal heat entry to the membrane was achieved at a laser wavelength of 1550 nm. As heat entry to the membrane was to be minimised, it was decided to operate the experiment at this optical wavelength. The laser system of choice was a *Koheras Boostik E-15* manufactured by *NKT Photonics*. It consisted of a 50 mW fibre laser, which was used as seed laser for a 5 W amplifier stage. Within a supervised masters thesis, the RIN level of this laser was measured to be  $2.5 \cdot 10^{-6}$  for the relevant frequency ( $f < 1$  MHz), compare Fig. 6.5. [150]. This was found in good agreement with the manufacturer specifications, and about one order of magnitude worse than typical NPRO lasers. Here, the same intensity stabilisation scheme was set up, providing 15 dB noise suppression at 100 kHz (compare Fig. 6.5). The laser relaxation oscillation at 330 kHz could be suppressed by an internal noise eater function, which was already included in the laser source. The laser light was emitted from a combined fibre collimator with an internal Faraday optical isolator. An additional Faraday isolator was used on the optical table to provide an even higher extinction rate in backward direction. After transmission through an EOM for modulation and the active power stabilisation stage (see Section 4.3.4), the laser light was spatially filtered by a ring mode cleaner cavity and now available for injection into the interferometer.

## 6 Cryogenic cooling of the interferometer

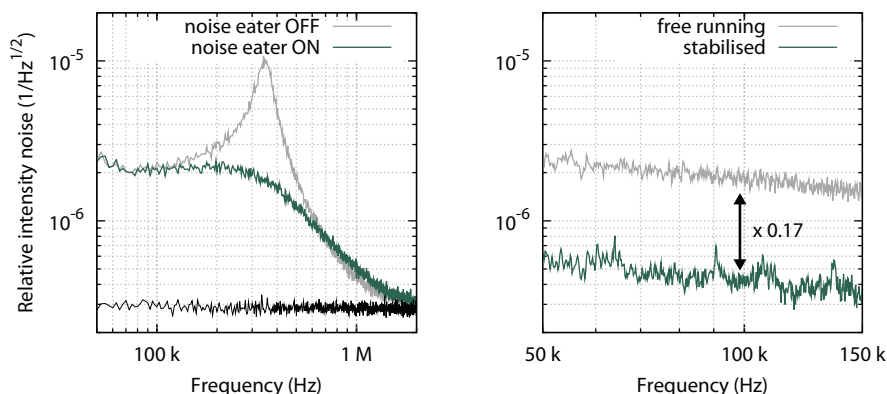


**Figure 6.5:** Left: Relative intensity noise measurement of the 1550 nm laser system. The RIN level at 100 kHz was found to be  $2.0 \cdot 10^{-6} 1/\sqrt{\text{Hz}}$ . For  $\approx 10$  A amplifier current, the laser relaxation oscillation was found at 330 kHz and could be suppressed by an internal noise eater. Right: performance of the laser stabilisation. The RIN level is suppressed by a factor of about 5.6.

### 6.4.3 Interferometer installation procedure

Because of the cryocooler layout, in which the interferometer is hanging upside down in the closed vacuum chamber, the interferometer could not be aligned in the cryocooler. The alignment of both, Sagnac and Michelson mode is already difficult when IR-Cameras provide vision and optical sensor cards can be used to follow the various beam paths within the interferometer. Aligning the combined interferometer as 'black-box' is not possible. Thus, another installation procedure was chosen.

First, the distance between the last steering mirror (or any other point of reference along the beam path) was determined by the CAD construction of the interferometer and the lengths specifications of the cryo chamber and an auxiliary optical path of the same length was established outside of the tank. A flip mirror was used to switch between a position for the interferometer in- or outside of the cryocooler. The interferometer was then assembled and aligned on the optical table following the procedure given in Section 4.4.4, using the auxiliary beam. The outside alignment of the interferometer was complete when an interference contrast of  $C = 97\%$  was established, and the beam reflected by the interferometer was transmitted through the initial mode cleaner cavity.

In this situation, the interferometer could be treated as a 'black-box', which is an effective mirror for the 'correct' optical input mode. Thus,

## 6.4 Interferometer prototype for cryogenic environment

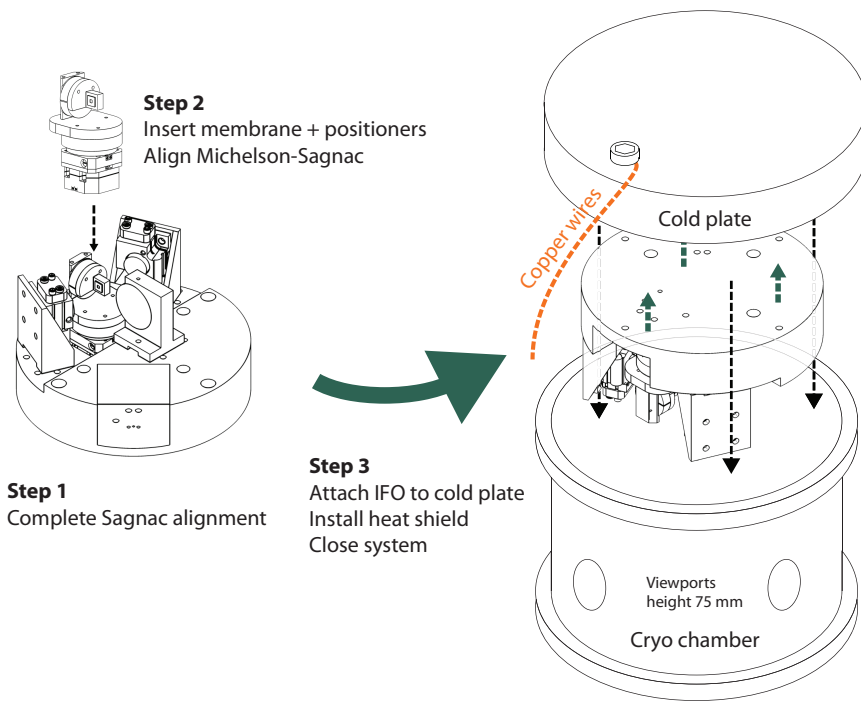


**Figure 6.6:** Installation procedure of the interferometer into the cryo chamber and cold plate. First, the Sagnac interferometer is aligned on the optical table. In a second step, the membrane is installed and aligned. When both, Sagnac and Michelson mode are overlapped on the beam splitter with sufficient interference contrast, the entire interferometer is installed upside down and attached directly to the cryocooler cold plate. A thermal contact between the membrane holder and the cold plate is established by thin, insulated copper wires. When attached, the cryo head (including cold plate and interferometer) is lowered (closed) and the optical input beam is aligned to the interferometer by a set of external mirrors. Note that in this figure, the interferometer has to be rotated by 180 degree to account for the viewports. The heat shield encased the installed interferometer, but is not shown here for simplicity.

it could be installed into the cryocooler, assuming that the internal alignment remains stable. In case of the interferometer installed to the cryo chamber, a reduced interference contrast can thus only be caused by the wrong input mode, which could be corrected by a set of two steering mirrors close the optical viewports.

Next, the cryo chamber was opened and the interferometer could be installed upside down to the cryocooler's cold-finger. Cables for connection of the piezo positioners were guided through drillings in the interferometer baseplate. Thin copper wires were clamped to the mem-

## 6 Cryogenic cooling of the interferometer

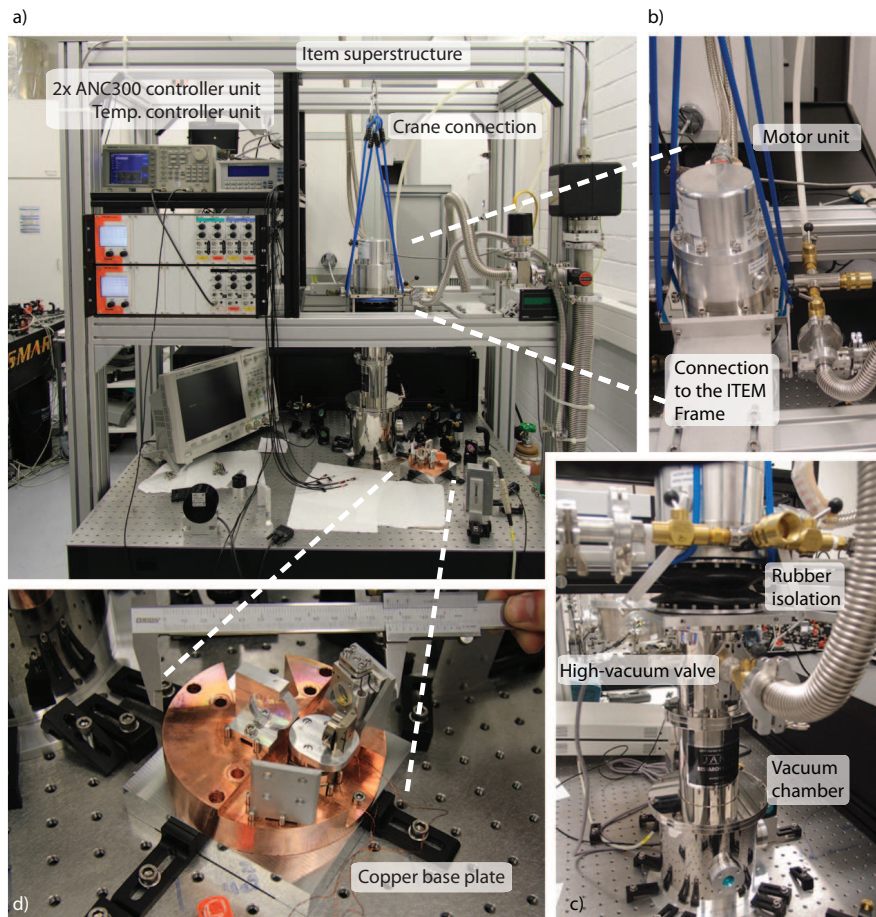


**Figure 6.7:** Photos of the realised cryocooler setup. a) Cryocooler, *Item* superstructure, temperature and *Attocube* controller units (left). b) Cold head and connection to the *Item* structure. Helium inlet and evacuation hose for the cold head are attached. c) Lower part of the cryocooler: Vacuum chamber with view ports, rubber Viton isolation and vacuum hoses for the high vacuum chamber. d) Interferometer during external alignment process (without membrane holder installed).

brane holder in order to improve heat exchange between membrane and cold plate. After isolating the copper wires with thin *Teflon* tape, the cryocooler radiation shield was attached and the cryo chamber was closed by lowering the cryocooler. The *Teflon* was used to bundle the copper wires, avoiding contact to other surfaces (and thereby reducing the heat transfer) and also allowing to prevent the wires from hanging in the beam path. The work flow of the installation process is depicted in Fig. 6.6.

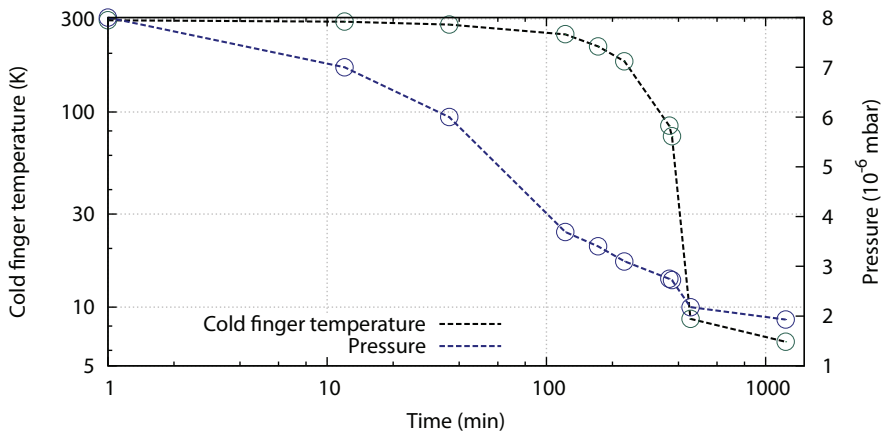


**Figure 6.8:** Cool-down of the system with interferometer installed. The temperature is measured at the cryocooler cold finger via a calibrated, temperature dependent electrical resistance. The pressure within the system is decreasing for gas molecules freeze out on the cold surfaces of, for example, the heat shield. A temperature below 10 K is measured after 360 minutes.

## 6.5 Results

This section describes the effect of low temperatures on the interferometer sensitivity and the membrane and presents obtained data for an interferometer operation below 10 K.

### Cooling performance

In a first cool down sequence with the interferometer mounted below the cold plate, the cold finger temperature and the pressure within the cryogenic system were measured. The measurement is depicted in Fig. 6.8. Although the compressor immediately starts working when switched on, the temperature just drops slowly. According to the manufacturer specifications, a base temperature of 8 K should be reached after 1.5 hours of operation. The difference in cool down time was attributed to the fact that the massive interferometer base plate had to be cooled. During the cool-down, all pumps except the ion getter pump were kept running, and the valves to the cryo chamber were opened.

After the cryocooler reached the base temperature, the compressor unit was switched off and the cold-finger temperature as well as the pressure within the system were monitored. The ion getter pump was switched on before the measurement, and the high vacuum valve to



## 6 Cryogenic cooling of the interferometer

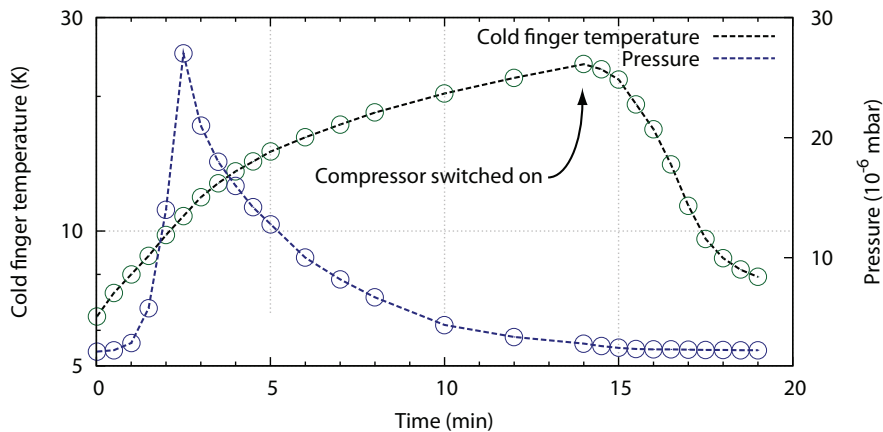


**Figure 6.9:** Switching off the compressor of the cryocooler results in a slow increase of cold-finger temperature. The pressure inside the vacuum chamber shortly increases, but then stabilises on a sufficiently low level to operate the experiment.

the TMP and scroll pump was close, only the evacuation valve to the sample chamber was remained open.

After 14 minutes, the compressor was started again. The temperature immediately started to drop, reaching 7 K after about 5 minutes. The measurement indicates that the temperature increase is rather fast without the compressor running. Averaging the output spectra was thus not possible at minimal temperature, because the mechanical resonance frequencies shifted by more than the mechanical linewidth during two consecutive measurements of the output spectrum (compare Sec. 6.5.2).

### 6.5.1 Cryogenic interferometer performance

During the cool process, the membrane position was continuously scanned to observe the interferometer contrast, piezo travel range and optical output mode. All positioners were found to be operational at 8 K. The interferometer fringe with the maximal amplitude of the applied high voltage ( $U = 150$  V) contained two dark-fringes, corresponding to a maximal scanning range of 400 nm, which is within the manufacturer specifications for the ANPx101 under load and at low temperatures.

The interferometer contrast was found to be severely reduced from 97% to about 70% within the first 20 – 40 K below room temperature, and was found to stabilise at  $C \approx 20\%$  at a temperatures of



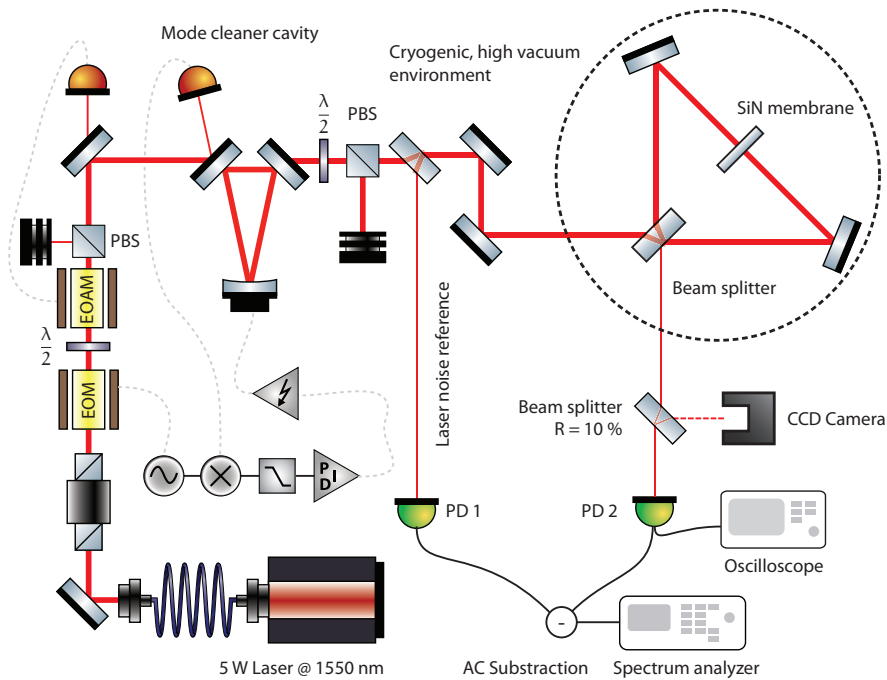


**Figure 6.10:** Schematic of the cryogenic experiment. The laser light is spatially filtered by a mode cleaner cavity. A fraction of the laser light is picked up on an auxiliary photo detector in reflection of a polarising beam splitter. The residual laser is incident onto the interferometer, which is installed into the cryocooler. The AC filtered output of the two photo detectors is subtracted electronically and fed into a spectrum analyser.

20 K. Both, the reduced interferometric contrast and the high technical laser noise resulted in a laser noise dominated output spectrum. Thus, a readout with a single photodetector in the output port of the interferometer was unable to resolve the thermally excited resonances of the membrane. Therefore, the setup was extended to cancel the laser noise in the readout with an auxiliary photo detector. This detector was positioned in front of the interferometer and picked up a fraction of the input laser light. The detectors electronic transfer functions were adjusted to match, and both were operated with the same mean beam power. The two AC outputs could be subtracted and therefore cancelled the correlated laser noise. The thermal signal was generated inside the interferometer, and thus was not subtracted. The setup used is depicted in Fig. 6.10.

## 6 Cryogenic cooling of the interferometer

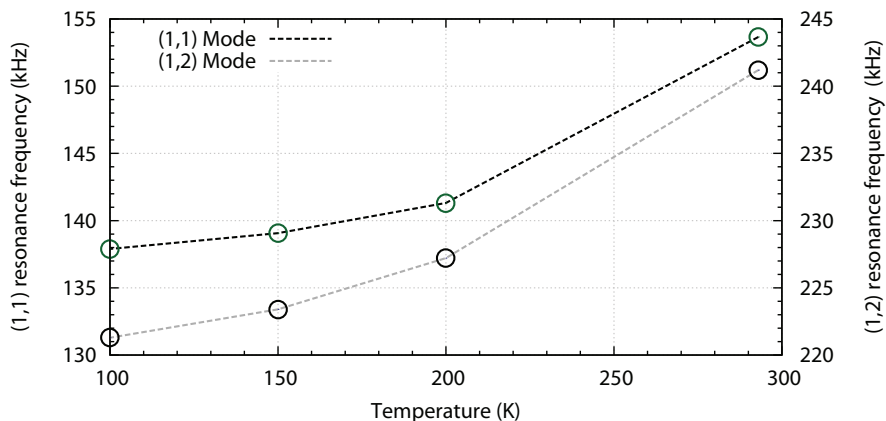


**Figure 6.11:** Resonance frequencies of the (1,1) and the (1,2) oscillation mode during cool down. Both modes experience a frequency decrease of about 10 % of their initial resonance frequency.

### 6.5.2 Influence of low temperatures on the membrane

Cryogenic temperatures also affected the SiN membrane mechanical resonance frequencies. Figure 6.11 depicts the measured resonance frequencies for the (1,1) and (1,2) mode of a low-stress membrane during the cool down process. The resonance frequencies were found to decrease to about 90 % of their initial values, indicating a reduction of internal stress (compare Sec. 3.4.2). A direct measurement of the membrane temperature was impossible as no temperature sensor could be attached to the fragile membrane. It could be assumed that the membrane resonance frequencies are stable in case of thermal equilibrium with the membrane environment.

The membrane mechanical quality factor was determined for both, cryogenic and close-to room temperature ( $T = 260$  K) environment by ring-down measurements. As already reported in [77], the quality factor increased by about one order of magnitude,  $Q_{300\text{ K}} = 5.2 \cdot 10^5$  and  $Q_{8\text{ K}} = 6.8 \cdot 10^6$  for temperatures below 20 K. Our observation is different from [77], where the Q factor increased rapidly for temperatures below 8 K, such that it might be attributed to a different mechanism, which might be related to the method of fixing the membrane frame. Figure 6.12 shows a comparison of the exponential decay of the oscillation amplitude after sudden stop of the excitation.

Calibrated interferometer output spectra were obtained at temperatures  $T = 260$  K, 20 K and at 8 K, respectively, and are shown in Fig. 6.13. All three spectra all three are dominated by laser noise due to

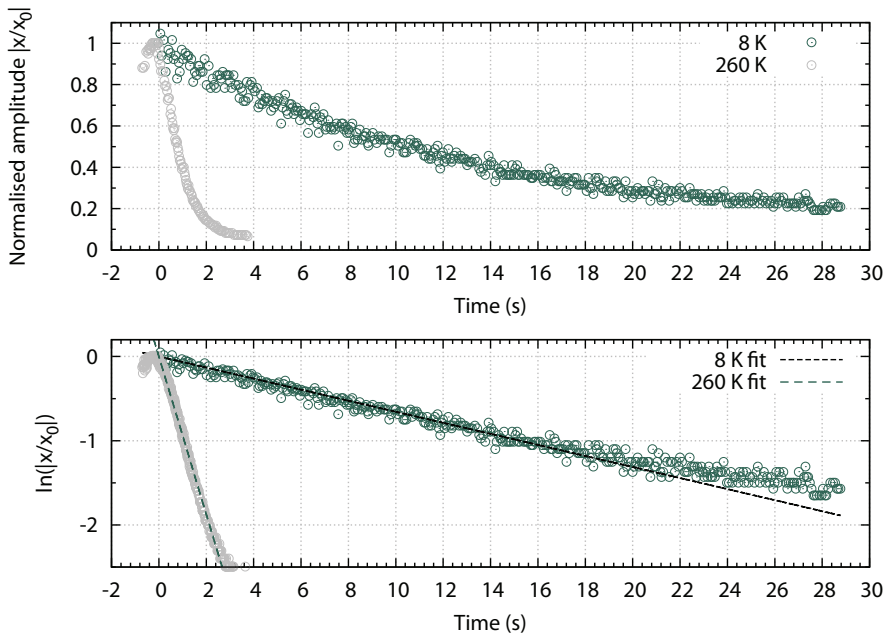


**Figure 6.12:** Ring-down measurements of a low-stress, clamped silicon nitride membrane at 260 K (grey circles) and at  $T = 8$  K (green circles). An exponential fit is depicted on the lower, semi-logarithmic graph. Note that the two measurements had a slightly different relative dark-noise level (such that green does not approach the same zero), such that the last seconds were not used for the fit.

a reduced contrast at low temperatures as discussed in the next section, with a displacement sensitivity of  $5 \cdot 10^{-15} \text{m}/\sqrt{\text{Hz}}$  around the mechanical resonance frequency.

The spectra for low temperatures were obtained without running compressor unit. This was due to high vibrations of the compressor, which were transferred to the experiment via the vacuum connections (as these were fixed on the outer *item* profiles, and thereby transferred the motion of the motor indirectly. Because of the narrow mechanical linewidth (high mechanical quality factor), the spectra could not be averaged, as the temperature immediately started to increase steadily when the compressor was switched off. This also caused the resonance frequency to shift by more than the mechanical linewidth per second.

## 6 Cryogenic cooling of the interferometer

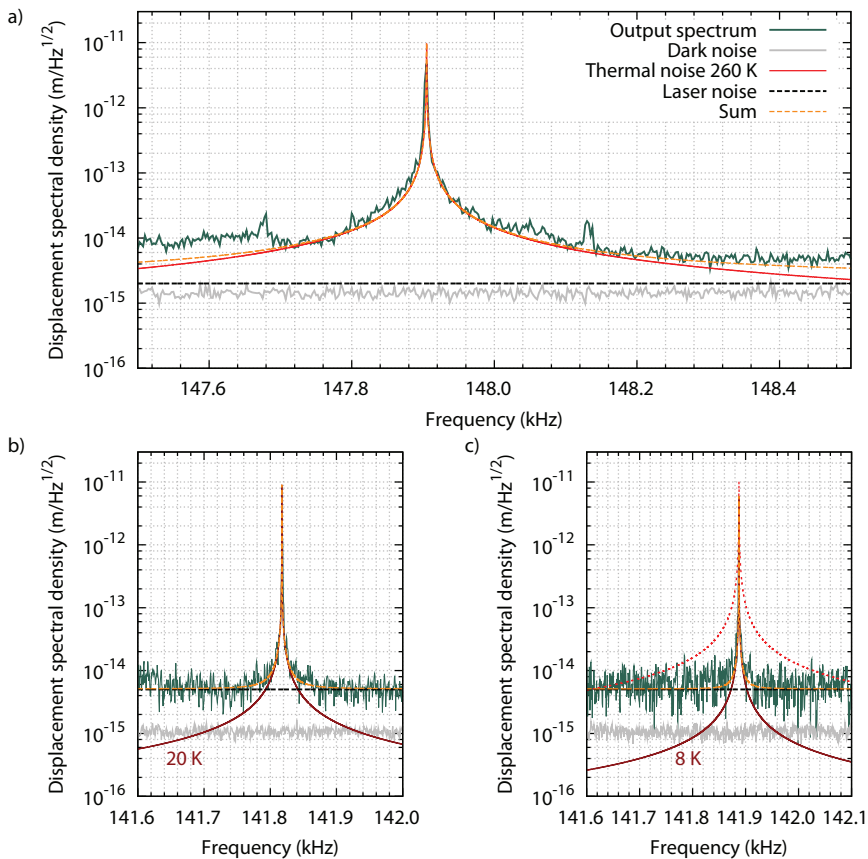


**Figure 6.13:** Displacement noise linear spectral densities for the interferometer operated at a)  $T = 260$  K. The temperature was inferred from the calibrated output spectrum. The orange trace depicts the sum of technical, thermal (red) and electronic dark noise. b) Calibrated output spectrum for  $T = 20$  K. The quality factor was measured to  $Q_{20\text{K}} = 6.5 \cdot 10^6$ . The spectrum is limited by technical laser noise, which is at a higher level due to the reduced contrast of  $C \approx 20\%$ . c) Spectrum for  $T = 8$  K. The thermal noise is plotted as dark red line. For a comparison, the expected thermal noise at 260 K is depicted as red dashed trace. The measurement agrees with the anticipated thermal noise, given the oscillator parameters.

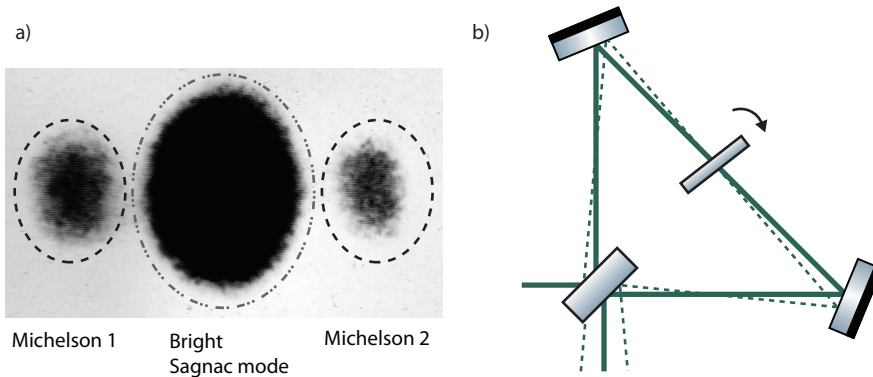


**Figure 6.14:** a) CCD picture of the interferometer output mode with intentional misalignment of the membrane (inverted colors). A bright central spot is observed, originating from a misalignment of the Sagnac interferometer. b) Intentional misalignment of the membrane to separate Michelson- and Sagnac modes.

### 6.5.3 Identified problems

The cool-down process caused misalignment of the steering mirrors, which resulted in non-ideal destructive interference of the Sagnac mode at the interferometer output port. This was verified by manually misaligning the membrane to separate the Michelson and Sagnac modes. For a balanced beam splitter and ideal alignment, the Sagnac amplitude should be vanishing, and only two spots, corresponding to the reflection on each membrane side were expected. The interferometer output mode was analysed with a CCD camera and the result is depicted in Fig. 6.14. The non-vanishing electric field in the central (Sagnac) mode cannot be compensated by the Michelson modes, as can be seen from the output power in the respective individual modes. The Michelson modes are still present (here, intentionally misaligned). The signal-to-noise ratio is reduced, however. The misalignment occurred within the first 30 K below room temperature.

The contrast constantly degraded from 97 % at room temperature to about 70 % at 260 K, and was reduced to about 20 % at temperatures as low as 20 K. As a result, technical laser noise coupled into the measurement and dominated the output power spectrum at the relevant frequencies. The Sagnac interferometer could not be realigned without a complete disassembly of the system. Moreover, the misalignment was found to be irreversible by heating up the system to room temperature again.

### 6.5.4 Next steps

To increase the interferometer sensitivity, a list of possible improvements could be derived. First, the reduction technical laser noise in the read out is the major priority. The cryogenic experiment highlighted the necessity for a remote control of the interferometer key components, namely the steering mirrors. Currently, the steering mirror mounts are exchanged for additional *Attocube* positioners. Full remote control is expected to provide an interferometer contrast of  $C > 99\%$  at low temperatures, as it has been demonstrated for the Michelson-Sagnac with signal-recycling already. Moreover, a new seed laser model with significantly reduced RIN level of  $10^{-7}/\sqrt{\text{Hz}}$  was ordered and is currently being installed.

Second, the isolation stage between cold head and experimental stage may not be 'shortened' with the flexible hoses for the vacuum system. Those were fixed at the *item* superstructure, which also supported the cold head with a rigid connection. This is a clear weakness, which can be eliminated by a separating the cold head and hoses support. A better isolation should allow for running the compressor while taking (and averaging) output spectra, providing a clearer measurement of the oscillator displacement spectrum.

Beside these technical improvements, the experiment is planned to operate with injection of a squeezed vacuum state into the interferometer output. Within a masters thesis, a squeezed light source is currently being set up and is expected to provide a reduced shot noise level of  $6 - 10$  dB. Thereby, the relative shot noise level can be decreased. At the same time, injection of a squeezed vacuum state is compatible with signal-recycling [94], such that both can be used to enhance the displacement sensitivity.

## 6.6 Chapter summary

The last chapter contains provides an overview about the installation and operation of a Michelson-Sagnac at cryogenic temperatures. For this purpose, the first cryogenic system at the Albert-Einstein Institute was set up from scratch. The utilised Gifford-McMahon cryocooler was presented and its working principle was explained. An interferometer prototype for operation at cryogenic temperatures was designed and tested. An oscillator temperature of  $T = 8$  K was inferred from the calibrated interferometer output spectra. The re-

sults highlighted the need for remote control of the steering mirrors in order to maintain a high interferometer contrast. The result is promising, as remote access to the alignment can easily be enabled by low-temperature specified piezo positioners, which were already used for alignment of the membrane. The situation is then similar to the alignment at room temperature and under vacuum conditions. For this situation, the interferometer contrast of  $> 99\%$  was already demonstrated within this thesis.





# 7

## Chapter 7

### Summary

In the framework of this thesis, a signal-recycled Michelson-Sagnac interferometer was realised and investigated. The interferometer incorporated a translucent silicon nitride membrane, which acted as high-quality, micro-mechanical oscillator and common end-mirror in a Sagnac interferometer, giving rise to a combined Michelson-Sagnac interferometer. A small interferometer arm length of about 7.5 cm diminished the influence of angular misalignment of the interferometer optical components. Moreover, these components were mounted in remote controllable positioners. Thereby, an interference contrast as high as 99.7% was achieved in high-vacuum ( $p \leq 10^{-6}$  mbar). Hence, technical power fluctuations of the laser light were suppressed to a high degree in the interferometer readout port. To eliminate remaining laser noise, a high-speed laser intensity stabilisation was set up and a balanced homodyne readout scheme was established. A shot noise limited displacement sensitivity of  $1.9 \cdot 10^{-16}$  m/ $\sqrt{\text{Hz}}$  for frequencies from 60 kHz up to 25 MHz was achieved.

The high interferometer contrast in particular allowed the interferometer to be operated as a compound mirror in an effective cavity, established by a high-reflective signal-recycling mirror in the interferometer output port. An analytical model for the recycled interferometer sensitivity in the presence of cavity internal optical losses is given. This is of importance for signal-recycling mirror transmissivities that are close to, or below, the intrinsic optical loss within the cavity. In the latter case, the signal-recycling gain falls below unity, and the displacement sensitivity is reduced. This situation occurred in the experiments when a recycling mirror with a power reflectivity of

## 7 Summary

---

$R_{\text{sr}} = 99.97\%$  was installed. The high power reflectivity is required in order to achieve a strong dissipative opto-mechanical coupling, as described in [53]. A model for the resulting complex optical spring in the case of close-to dark-fringe operation of the interferometer has been developed in close collaboration with the theoretical quantum optics group [140], and its implications are discussed. In particular, the optical spring depends on both the signal-recycling cavity detuning and the interferometer offset from the dark-fringe. This dependence gives rise to anomalous, opto-mechanical back-action effects, such as a conditional instability and cooling on signal-recycling cavity resonance. The former was observed in the experiment, confirming the theoretical model. In addition, the predicted optical damping was verified qualitatively in the experiment by inferring a reduced effective quality factor of the oscillator for different optical input powers. For an optical input power of 200 mW, the mechanical quality factor was reduced by more than two orders of magnitude, yielding  $Q_{\text{eff}} = 1730$ , limited by a 1% optical loss within the interferometer.

In a second experiment, a full Michelson-Sagnac interferometer was cooled to cryogenic temperatures. Therefore, a Gifford-McMahon type cryocooler was set up, and an interferometer prototype for operation at temperatures close to absolute zero was realised. The experiment was carried out at a laser wavelength of 1550 nm to minimise optical absorption. The analysis of calibrated interferometer output spectra demonstrated a reduction of the oscillator temperature from  $T = 300$  K down to 8 K, reducing the associated displacement thermal noise around the fundamental mechanical resonance by more than one order of magnitude.

In conclusion, a signal-recycled Michelson-Sagnac interferometer was established as a novel opto-mechanical topology. It allows the study of dissipative opto-mechanical coupling and associated optical cooling in the unresolved side band regime. The theoretical model for the complex optical spring was confirmed in the experiment by observing a predicted conditional instability, as well as the anticipated optical damping. Moreover, the achievement of cryogenic oscillator temperatures resolves the restriction to conduct the experiments at room temperature, and hence marks a major step towards the regime of an all-quantum noise dominated experiments.

# 8

## Chapter 8

### Appendix A

#### 8.1 Finesse Simulation File

To calculate the interferometer output field and the shot noise limited sensitivity of the Michelson-Sagnac interferometer, a Finesse (version 0.998) [120] script was used. For more information about this open source software, the reader is kindly referred to [118].

```
# ===== Laser modulation

const fMi 100k
const demod 12.14M
l l1 0.05 0 nin
mod eom1 $fMi 0.17 2 pm 0 nin n1
```

In this part of the code, the laser input and modulation via a first EOM are defined.

```
# ===== Michelson-Sagnac Interferometer

const uloss 0.002
#const uloss 0

bs msbs 0.5 0.5 0 45 n1 n2 n3 n4

s airgaparm1 0.0375 n2 n5

bs1 ul1 0 $uloss 0 45 n5 nMem1 dump dump
```

## 8 Appendix A

---

```
m mMembran 0.17 0.83 135 nMem1 nMem2
fsig sig1 mMembran 1 0
```

```
bs1 ul2 0 $uloss 0 45 nMem2 n9 dump dump
```

```
s airgaparm2 0.0375 n9 n3
```

The simulation is either done with or without loss being considered. Then the central beam splitter is defined, as well as the interferometer arm lengths. The steering mirrors to fold both arms are defined as beam splitters here, for mirrors only having two optical ports in Finesse and are usually considered under normal incidence.

```
# ===== Signal recycling mirror
```

```
const delta 0.99970
```

```
s airgapsr 0.012 n4 n13
```

```
m2 mSR $delta 0 102.175 n13 n14 # Rsr = 99.97 % Tuned
```

```
s airgapst2 0.01 n14 n15
```

Straight forward, the distance from the central beam splitter to the recycling mirror as well as the signal recycling mirror are defined. Some tuning is necessary to calculate the resonant case (or a detuned one). The detuning depends on the mirror reflectivity.

```
# ===== Propagation loss to detector
```

```
bs2 verlustbs 0.64 0 0 45 n15 ndump n16 ndump
```

A beam splitter is placed between the homodyne detector to pick up light. In the experiment, this pickup provided the error signal to keep the signal recycling cavity resonant. Changing the achievable displacement sensitivity due to its power reflectivity, it has to be considered in the simulation file. The same argument also applies for the quantum efficiency of the detector in use, which was set to 0.7 for the simulations.

```
# ===== Power recycling mirror

#const delta 0.99

#s airgappr 0.01 npr2 n1
#m2 mPR $delta 0 0 npr1 npr2
```

A power recycling mirror can be added to the simulation. It was not used in the experiment, however, such that it was left unconsidered here as well.

```
# ===== Read out 2 (Homodyne)

pd out n16

qshot qnoise 2 $fMi max 1 max n16
noplplot qnoise
set qn1p qnoise re
func qn2p = sqrt($qn1p*6.6262E-34*299792458.0 / 1064E-9)
noplplot qn2p
pd2 pdmisa $fMi max 1 max n16
noplplot pdmisa
set tr1p pdmisa abs
func tr2p = 2*3.141 / 1064.0E-9* $tr1p
noplplot tr2p

#yaxis lin abs

xaxis sig1 f log 10 1000M 3000
put pdmisa f2 $x1
put qnoise f2 $x1

GNU PLOT
noplplot
set yrange [0.9:1]
set xlabel 'Membrane detuning (rad)'
set ylabel 'P_{out}/P_{in}'
plot "misasr2012.out" u ($1):($2) notitle
END
```

The last paragraph contains plotting options used by Gnuplot.

### 8.2 Matlab Files

A Matlab file allows to calculate the optical spring in the signal-recycled Michelson-Sagnac interferometer [164]. Note that the script assumes the interferometer to be tuned close to dark-fringe, also, the optical spring is not calculated as function of frequency  $\omega$ , but as function of detuning.

```
clear;
clc;

c = 299792458;
hbar = 1.054e-34;

L_sr0 = 0.087;
tau_sr0 = L_sr0/c;

lambda_initial = 1.064*10^(-6);
N = round(2*L_sr0/lambda_initial);
k0 = pi*N/L_sr0;
lambda0 = 2*pi/k0;
omega0 = c*k0;
P_in = 200*10^(-3);

R_m_power = 17;
R_m = sqrt(R_m_power/100);
T_m = sqrt(1 - R_m^2);
R_sr_power = 99.97;
R_sr = sqrt(R_sr_power/100);
T_sr = sqrt(1 - R_sr^2);

delta_bs_percent = 0.1;
delta_bs = delta_bs_percent/100;
R_bs = sqrt(0.5 - delta_bs/2);
T_bs = sqrt(0.5 + delta_bs/2);

m = 80*10^(-12);
f_m = 130*10^3;
omega_m = 2*pi*f_m;
Q_m = 5.8*10^5;
gamma_mem = omega_m/(2*Q_m);

delta_l_DP = (1/k0)*acos((T_m/R_m)*(-delta_bs/sqrt(1-delta_bs^2)));
ksi = 0.0125*lambda0;
```

```

delta_l = delta_l_DP + ksi; delta_l/lambda0;
Omega = omega_m;

loss = 0.01;
gamma_s = c*(T_sr^2+loss)/(4*L_sr0);

gamma_m = c*R_m^2*(k0*ksi/2)^2/L_sr0;
gamma = gamma_s + gamma_m;

delta_m = -c*R_m*T_m*(k0*ksi/2)^2/L_sr0;

y = 0;
for delta = -10*gamma:0.001*gamma:10*gamma

    y = y + 1;
    delta_s = delta - delta_m;

    K(y) = (4*k0*R_m^2*P_in/L_sr0)*(1/((gamma-i*Omega)^2+delta^2)) ...
        *(delta_s*(gamma^2+delta^2-4*(gamma*gamma_m+delta*delta_m)) ...
        + 2*i*(gamma_s*delta_m+gamma_m*delta_s)*Omega+delta_m*Omega^2)...
        /(delta^2+gamma^2);

    gamma_OM(y) = -(1/(2*m*Omega))*imag(K(y));
    gamma_full(y) = gamma_mem + gamma_OM(y);
    Q(y) = omega_m/(2*gamma_full(y));

    Q_intr(y) = Q_m;
end

delta = -10*gamma:0.001*gamma:10*gamma;
x = (delta)/gamma;
x_sr = (delta-delta_m)/gamma;
figure;

semilogy(-x,Q_intr,-x,Q,'Linewidth',1.5); legend('Initial','Final')
xlabel('\Delta / \gamma');
grid on;

ifoarray = [];
ifoarray = [x;real(K);imag(K);Q;Q_intr];

filename1 = 'springdata.dat';

fid = fopen(filename1, 'w');
fprintf(fid, '%E %E %E %E %E\n', ifoarray);
fclose(fid);

```





## Bibliography

- [1] A. Einstein, *Über einen die Erzeugung und Verwandlung des Lichtes betreffenden heuristischen Gesichtspunkt*, Annalen der Physik **322**, Nr. 6, 132 (1905). 1
- [2] M. Planck, *Ueber das Gesetz der Energieverteilung im Normalspectrum*, Annalen der Physik **309**, 553 (1901). 1
- [3] P. Lebedew, *Untersuchungen über die Druckkräfte des Lichtes*, Annalen der Physik **311**, 433 (1901). 1
- [4] E. F. Nichols and G. F. Hull, *A Preliminary Communication on the Pressure of Heat and Light Radiation*, Phys. Rev. (Series I) **13**, 307 (1901). 1
- [5] A. Einstein, *Strahlungs-Emission und Absorption nach der Quantentheorie*, Deutsche Physikalische Gesellschaft **18**, 318 (1916). 1
- [6] T. H. Maiman, *Stimulated Optical Radiation in Ruby*, Nature **187**, 493 (1960). 1
- [7] A. L. Schawlow and C. H. Townes, *Infrared and Optical Masers*, Phys. Rev. **112**, 1940 (1958). 1, 41
- [8] M. E. Gertsenshtein and V. I. Pustovoit, *On the detection of low frequency gravitational waves*, J. Exp. Theoret. Phys. (U.S.S.R.) **42**, 605 (1962). 2
- [9] J. H. Taylor, L. A. Fowler and P. M. McCulloch, *Measurements of general relativistic effects in the binary pulsar PSR1913 + 16*, Nature **277**, 437 (1979).
- [10] *The Detection of Gravitational Waves*, edited by D. G. Blair (Cambridge Univ. Press., Cambridge, 1991). 2
- [11] A. Abramovici, W. E. Althouse, R. W. P. Drever, Y. Gürsel, S. Kawamura, F. J. Raab, D. Shoemaker, L. Sievers, R. E. Spero, K. S. Thorne, R. E. Vogt, R. Weiss, S. E. Whitcomb and M. E. Zucker, *LIGO: The Laser Interferometer Gravitational-Wave Observatory*, Science **256**, 325 (1992). 2
- [12] B. P. Abbott et al., *LIGO: the Laser Interferometer Gravitational-Wave Observatory*, Reports on Progress in Physics **72**, 076901 (2009). 2

## BIBLIOGRAPHY

---

- [13] B. Willke et al., *Status of GEO 600*, Classical and Quantum Gravity **21**, S417 (2004). 2
- [14] F. Acernese et. al, *Status of VIRGO*, Classical and Quantum Gravity **21**, S385 (2004). 2
- [15] M. Ando and the TAMA Collaboration, *Current status of the TAMA300 gravitational-wave detector*, Classical and Quantum Gravity **22**, S881 (2005). 2
- [16] C. M. Caves, *Quantum-Mechanical Radiation-Pressure Fluctuations in an Interferometer*, Physical Review Letters **45**, 75 (1980). 2, 33
- [17] M. T. Jaekel and S. Reynaud, *Quantum Limits in Interferometric Measurements*, EPL (Europhysics Letters) **13**, 301 (1990). 2, 3
- [18] Gravitational Wave Interferometer Noise Calculator, 2010, <https://workarea.ego-gw.it/ego2/virgo/advanced-virgo/osd/simulations/gwinc.2>
- [19] G. M. Harry and the LIGO Scientific Collaboration, *Advanced LIGO: the next generation of gravitational wave detectors*, Classical and Quantum Gravity **27**, 084006 (2010). 3
- [20] C. M. Caves, *Quantum-mechanical noise in an interferometer*, Phys. Rev. D **23**, 1693 (1981). 3, 36
- [21] W. G. Unruh, in *Quantum Optics, Experimental Gravitation, and Measurement Theory*, edited by P. Meystre and M. O. Scully (Plenum, New York, 1982), p. 647.
- [22] H. Vahlbruch, S. Chelkowski, B. Hage, A. Franzen, K. Danzmann and R. Schnabel, *Demonstration of a Squeezed-Light-Enhanced Power- and Signal-Recycled Michelson Interferometer*, Phys. Rev. Lett. **95**, 211102 (2005). 33
- [23] E. E. Mikhailov, K. Goda, T. Corbitt and N. Mavalvala, *Frequency-dependent squeeze-amplitude attenuation and squeeze-angle rotation by electromagnetically induced transparency for gravitational-wave interferometers*, Phys. Rev. A **73**, 053810 (2006). 3
- [24] S. Vyatchanin, *The estimation of signal force parameters in quantum variation measurement*, Physics Letters A **239**, 201 (1998). 3
- [25] H. J. Kimble, Y. Levin, A. B. Matsko, K. S. Thorne and S. P. Vyatchanin, *Conversion of conventional gravitational-wave interferometers into quantum nondemolition interferometers by modifying their input and/or output optics*, Phys. Rev. D **65**, 022002 (2001). 3, 36

- [26] V. B. Braginsky and A. B. Manukin, *Ponderomotive effects of electromagnetic radiation*, Sov. Phys. JETP **25**, 653 (1967). 3
- [27] V. B. Braginsky, A. B. Manukin and M. Y. Tikhonov, *Investigation of dissipative Ponderomotive effects of electromagnetic radiation*, Sov. Phys. JETP **31**, 829 (1970). 3
- [28] A. Dorsel, J. D. McCullen, P. Meystre, E. Vignes and H. Walther, *Optical Bistability and Mirror Confinement Induced by Radiation Pressure*, Phys. Rev. Lett. **51**, 1550 (1983). 3, 89
- [29] T. Corbitt, D. Ottaway, E. Innerhofer, J. Pelc and N. Mavalvala, *Measurement of radiation-pressure-induced optomechanical dynamics in a suspended Fabry-Perot cavity*, Phys. Rev. A **74**, 021802 (2006). 3, 89
- [30] C. H. Metzger and K. Karrai, *Cavity cooling of a microlever*, Nature **432**, 1002 (2004). 3
- [31] D. Kleckner and D. Bouwmeester, *Sub-kelvin optical cooling of a micromechanical resonator*, Nature **444**, 75 (2006). 3
- [32] S. Gigan, H. R. Bohm, M. Paternostro, F. Blaser, G. Langer, J. B. Hertzberg, K. C. Schwab, D. Bauerle, M. Aspelmeyer and A. Zeilinger, *Self-cooling of a micromirror by radiation pressure*, Nature **444**, 67 (2006). 3
- [33] O. Arcizet, P.-F. Cohadon, T. Briant, M. Pinard and A. Heidmann, *Radiation-pressure cooling and optomechanical instability of a micromirror*, Nature **444**, 71 (2006). 3
- [34] T. Carmon, H. Rokhsari, L. Yang, T. J. Kippenberg and K. J. Vahala, *Temporal Behavior of Radiation-Pressure-Induced Vibrations of an Optical Microcavity Phonon Mode*, Phys. Rev. Lett. **94**, 223902 (2005). 3
- [35] A. Schliesser, P. Del'Haye, N. Nooshi, K. J. Vahala and T. J. Kippenberg, *Radiation Pressure Cooling of a Micromechanical Oscillator Using Dynamical Backaction*, Phys. Rev. Lett. **97**, 243905 (2006). 3
- [36] J. D. Thompson, B. M. Zwickl, A. M. Jayich, F. Marquardt, S. M. Girvin and J. G. E. Harris, *Strong dispersive coupling of a high-finesse cavity to a micromechanical membrane*, Nature **452**, 72 (2008). 3, 21, 89
- [37] A. M. Jayich, J. C. Sankey, B. M. Zwickl, C. Yang, J. D. Thompson, S. M. Girvin, A. A. Clerk, F. Marquardt and J. G. E. Harris, *Dispersive optomechanics: a membrane inside a cavity*, New Journal of Physics **10**, 095008 (2008). 3, 21, 81

## BIBLIOGRAPHY

---

- [38] J. Roels, I. De Vlaminck, L. Lagae, B. Maes, D. Van Thourhout and R. Baets, *Tunable optical forces between nanophotonic waveguides*, *Nat Nano* **4**, 510 (2009). 3
- [39] M. Aspelmeyer, S. Gröblacher, K. Hammerer and N. Kiesel, *Quantum optomechanics - throwing a glance*, *J. Opt. Soc. Am. B* **27**, A189 (2010). 4
- [40] F. Marquardt and S. M. Girvin, *Optomechanics*, *Physics* **2**, 40 (2009). 4
- [41] P. Meystre, *A short walk through quantum optomechanics*, *Annalen der Physik* **525**, 215 (2013). 4
- [42] Y. Chen, *Macroscopic quantum mechanics: theory and experimental concepts of optomechanics*, *Journal of Physics B: Atomic, Molecular and Optical Physics* **46**, 104001 (2013).
- [43] M. Aspelmeyer, T. J. Kippenberg and F. Marquardt, *Cavity Optomechanics*, ArXiv e-prints (2013). 4
- [44] T. Corbitt, Y. Chen, E. Innerhofer, H. Müller-Ebhardt, D. Ottaway, H. Rehbein, D. Sigg, S. Whitcomb, C. Wipf and N. Mavalvala, *An All-Optical Trap for a Gram-Scale Mirror*, *Phys. Rev. Lett.* **98**, 150802 (2007). 4, 92
- [45] D. G. Blair, E. N. Ivanov, M. E. Tobar, P. J. Turner, F. van Kann and I. S. Heng, *High Sensitivity Gravitational Wave Antenna with Parametric Transducer Readout*, *Phys. Rev. Lett.* **74**, 1908 (1995). 4
- [46] P. F. Cohadon, A. Heidmann and M. Pinard, *Cooling of a Mirror by Radiation Pressure*, *Phys. Rev. Lett.* **83**, 3174 (1999). 4
- [47] I. Wilson-Rae, N. Nooshi, W. Zwerger and T. J. Kippenberg, *Theory of Ground State Cooling of a Mechanical Oscillator Using Dynamical Backaction*, *Phys. Rev. Lett.* **99**, 093901 (2007). 4
- [48] F. Marquardt, A. A. Clerk and S. M. Girvin, *Quantum theory of optomechanical cooling*, *Journal of Modern Optics* **55**, 3329 (2008). 4
- [49] J. Chan, T. P. M. Alegre, A. H. Safavi-Naeini, J. T. Hill, A. Krause, S. Gröblacher, M. Aspelmeyer and O. Painter, *Laser cooling of a nanomechanical oscillator into its quantum ground state*, *Nature* **478**, 89 (2011). 4, 89, 111
- [50] J. D. Teufel, T. Donner, D. Li, J. W. Harlow, M. S. Allman, K. Cicak, A. J. Sirois, J. D. Whittaker, K. W. Lehnert and R. W. Simmonds, *Sideband cooling of micromechanical motion to the quantum ground state*, *Nature* **475**, 359 (2011). 4, 111

- [51] A. D. O’Connell, M. Hofheinz, M. Ansmann, R. C. Bialczak, M. Lenander, E. Lucero, M. Neeley, D. Sank, H. Wang, M. Weides, J. Wenner, J. M. Martinis and A. N. Cleland, *Quantum ground state and single-phonon control of a mechanical resonator*, *Nature* **464**, 697 (2010). 4, 111
- [52] F. Elste, S. M. Girvin and A. A. Clerk, *Quantum Noise Interference and Backaction Cooling in Cavity Nanomechanics*, *Phys. Rev. Lett.* **102**, 207209 (2009). 5, 69, 94
- [53] A. Xuereb, R. Schnabel and K. Hammerer, *Dissipative Optomechanics in a Michelson-Sagnac Interferometer*, *Phys. Rev. Lett.* **107**, 213604 (2011). 5, 69, 94, 111, 134
- [54] G. Heinzl, *Advanced optical techniques for laser-interferometric gravitational-wave detectors*, PhD Thesis, Universität Hannover, 1999. 6, 72, 74, 79, 86
- [55] H. Grote, *Making it Work: Second generation Interferometry in GEO600!*, PhD Thesis, Universität Hannover, 2003.
- [56] *Advanced Gravitational Wave Detectors*, edited by D. Blair, E. J. Howell, L. Ju and C. Zhao (Cambridge Univ. Press., 2012). 6
- [57] F. Hohls, *Strahlungsdruck in Laserinterferometern*, Diploma thesis, Universität Hannover, Institut für Atom- und Molekülphysik der Universität Hannover, 1995. 8, 9, 15
- [58] N. Wiener, *Generalized Harmonic Analysis*, *Acta Mathematica* **55**, 117 (1930). 8
- [59] A. Khintchine, *Korrelationstheorie der stationären stochastischen Prozesse*, *Mathematische Annalen* **109**, 604–615 (1943). 8
- [60] A. Van der Ziel, *Noise* (Englewood Cliffs, N.J. : Prentice-Hall, 1956). 9
- [61] J. C. Maxwell, *A Dynamical Theory of the Electromagnetic Field*, *Philosophical Transactions of the Royal Society of London* **155**, 459 (1865). 9
- [62] C. C. Gerry and P. L. Knight, *Introductory Quantum Optics* (Cambridge Univ. Press., 2010). 9, 10, 11
- [63] R. J. Glauber, *Coherent and Incoherent States of the Radiation Field*, *Phys. Rev.* **131**, 2766 (1963). 11
- [64] E. Schrödinger, *Der stetige Übergang von der Mikro- zur Makromechanik*, *Naturwissenschaften* **14**, 664 (1926). 12

## BIBLIOGRAPHY

---

- [65] S. Chelkowski, *Squeezed Light and Laser Interferometric Gravitational Wave Detectors*, PhD Thesis, Leibniz Universität Hannover, 2007. 12, 14
- [66] A. G. White, *Classical and quantum dynamics of optical frequency conversion*, PhD Thesis, Australian National University, 1997. 12
- [67] M. Mehmet, *Squeezed light at 1064 nm and 1550 nm with a nonclassical noise suppression beyond 10 dB*, PhD Thesis, Leibniz Universität Hannover, 2012. 12, 64
- [68] H. P. Yuen and J. H. Shapiro, *Optical communication with two-photon coherent states-Part III: Quantum measurements realizable with photoemissive detectors*, IEEE Transactions on Information Theory **26**, 78 (1980). 13
- [69] P. R. Saulson, *Fundamentals of interferometric gravitational wave detectors* (World scientific publishing Co., 1994), Vol. 1. 17, 18
- [70] P. R. Saulson, *Thermal noise in mechanical experiments*, Phys. Rev. D **42**, 2437 (1990). 19
- [71] H. Nyquist, *Thermal Agitation of Electric Charge in Conductors*, Physical Review **32**, 110 (1928). 19
- [72] H. B. Callen and T. A. Welton, *Irreversibility and Generalized Noise*, Phys. Rev. **83**, 34 (1951). 19
- [73] H. B. Callen and R. F. Greene, *On a Theorem of Irreversible Thermodynamics*, Phys. Rev. **86**, 702 (1952). 19
- [74] N. Ohishi, S. Otsuka, K. Kawabe and K. Tsubono, *Estimation of thermal noise by a direct measurement of the mechanical conductance*, Physics Letters A **266**, 228 (2000). 19
- [75] Norcada - MEMS Design & Development, 4465 - 99 Street Edmonton, Alberta, Canada T6E 5B6, <http://www.norcada.com>. 21
- [76] D. Friedrich, *Laser interferometry with coating-free mirrors*, PhD Thesis, Leibniz Universität Hannover, 2011. 21, 22, 23, 30, 48, 56, 78, 79
- [77] B. M. Zwickl, W. E. Shanks, A. M. Jayich, C. Yang, A. C. B. Jayich, J. D. Thompson and J. G. E. Harris, *High quality mechanical and optical properties of commercial silicon nitride membranes*, Applied Physics Letters **92**, 103125 (2008). 21, 34, 126
- [78] J. G. E. Gardeniers, H. A. C. Tilmans and C. C. G. Visser, *LPCVD silicon-rich silicon nitride films for applications in micromechanics, studied with statistical experimental design*, J. Vac. Sci. Technol. A **14**, 2879 (1996). 21

- [79] P. Temple-Boyer, C. Rossi, E. Saint-Etienne and E. Scheid, *Residual stress in low pressure chemical vapor deposition  $\text{SiN}_x$  films deposited from silane and ammonia*, J. Vac. Sci. Technol. **16**, 2003 (1998). 21
- [80] D. J. Wilson, C. A. Regal, S. B. Papp and H. J. Kimble, *Cavity Optomechanics with Stoichiometric  $\text{SiN}$  Films*, Phys. Rev. Lett. **103**, 207204 (2009). 21
- [81] T. Westphal, *Opto-mechanische Kopplung in einem Michelson-Sagnac Interferometer*, Diploma thesis, Leibniz Universität Hannover, 2009. 21, 23, 24, 27, 48, 53, 57, 58
- [82] J. C. Slater and N. H. Frank, *Introduction to theoretical physics* (International series in physics, 1933). 22
- [83] T. Westphal, D. Friedrich, H. Kaufer, K. Yamamoto, S. Gößler, H. Müller-Ebhardt, S. L. Danilishin, F. Y. Khalili, K. Danzmann and R. Schnabel, *Interferometer readout noise below the standard quantum limit of a membrane*, Phys. Rev. A **85**, 063806 (2012). 27, 36
- [84] D. Friedrich, H. Kaufer, T. Westphal, K. Yamamoto, A. Sawadsky, F. Y. Khalili, S. Danilishin, S. Gößler, K. Danzmann and R. Schnabel, *Laser interferometry with coating-free mirrors*, New Journal of Physics **13**, 093017 (2011). 32, 81
- [85] H. Kaufer, A. Sawadsky, T. Westphal, D. Friedrich and R. Schnabel, *Tomographic readout of an opto-mechanical interferometer*, New Journal of Physics **14**, 095018 (2012). 65
- [86] K. Yamamoto, D. Friedrich, T. Westphal, S. Gößler, K. Danzmann, K. Somiya, S. L. Danilishin and R. Schnabel, *Quantum noise of a Michelson-Sagnac interferometer with a translucent mechanical oscillator*, Phys. Rev. A **81**, 033849 (2010). 27, 33, 34, 75, 97, 102
- [87] A. Zeilinger, *General properties of lossless beam splitters in interferometry*, American Journal of Physics **49**, 882 (1981). 28
- [88] I. N. Bronstein and K. A. Semendjajew, *Taschenbuch der Mathematik*, 5 (Harri Deutsch, 2000). 29, 31
- [89] W. Schottky, *Über spontane Stromschwankungen in verschiedenen Elektrizitätsleitern*, Annalen der Physik **362**, 541 (1918). 32
- [90] W. A. Edelstein, J. Hough, J. R. Pugh and W. Martin, *Limits to the measurement of displacement in an interferometric gravitational radiation detector*, Journal of Physics E: Scientific Instruments **11**, 710 (1978). 32

## BIBLIOGRAPHY

---

- [91] H. Vahlbruch, S. Chelkowski, B. Hage, A. Franzen, K. Danzmann and R. Schnabel, *Coherent Control of Vacuum Squeezing in the Gravitational-Wave Detection Band*, Phys. Rev. Lett. **97**, 011101 (2006). 33
- [92] M. Mehmet, T. Eberle, S. Steinlechner, H. Vahlbruch and R. Schnabel, *Demonstration of a quantum-enhanced fiber Sagnac interferometer*, Opt. Lett. **35**, 1665 (2010).
- [93] M. Mehmet, S. Ast, T. Eberle, S. Steinlechner, H. Vahlbruch and R. Schnabel, *Squeezed light at 1550 nm with a quantum noise reduction of 12.3 dB*, Opt. Express **19**, 25763 (2011). 33
- [94] The LIGO Scientific Collaboration, *A gravitational wave observatory operating beyond the quantum shot-noise limit*, Nature Physics **7**, 962 (2011). 33, 130
- [95] H. Grote, K. Danzmann, K. L. Dooley, R. Schnabel, J. Slutsky and H. Vahlbruch, *First Long-Term Application of Squeezed States of Light in a Gravitational-Wave Observatory*, Physical Review Letters **110**, 181101 (2013). 33
- [96] T. P. Purdy, R. W. Peterson and C. A. Regal, *Observation of Radiation Pressure Shot Noise on a Macroscopic Object*, Science **339**, 801 (2013). 33, 37
- [97] D. W. C. Brooks, T. Botter, S. Schreppler, T. P. Purdy, N. Brahms and D. M. Stamper-Kurn, *Non-classical light generated by quantum-noise-driven cavity optomechanics*, Nature **advance on**, (2012). 34
- [98] T. P. Purdy, P.-L. Yu, R. W. Peterson, N. S. Kampel and C. A. Regal, *Strong Optomechanical Squeezing of Light*, ArXiv e-prints (2013). 34
- [99] J. D. Teufel, T. Donner, M. A. Castellanos-Beltran, J. W. Harlow and K. W. Lehnert, *Nanomechanical motion measured with an imprecision below that at the standard quantum limit*, Nature Nanotechnology **4**, 820 (2009). 36
- [100] G. Anetsberger, O. Arcizet, Q. P. Unterreithmeier, R. Riviere, A. Schliesser, E. M. Weig, J. P. Kotthaus and T. J. Kippenberg, *Near-field cavity optomechanics with nanomechanical oscillators*, Nat Phys **5**, 909 (2009). 36
- [101] L. Schnupp, Talk at the European Collaboration Meeting on Interferometric Detection of Gravitational Waves, 1988, sorrento, Italy. 41
- [102] O. S. Brozek, *Frequenzstabilisierung eines Nd:YAG-Hochleistungs-Laser-Systems für den Gravitationswellendetektor GEO600*, PhD Thesis, Universität Hannover, 1999. 41



- [103] Coherent Inc. (formerly Innolight), Mephisto/Mephisto S Data Sheet, 2012, <http://www.www.coherent.com>. 41
- [104] T. Day, *Frequency stabilized solid state lasers for coherent optical communications*, PhD Thesis, Stanford, 1990. 41
- [105] P. Kwee and B. Willke, *Automatic laser beam characterization of monolithic Nd:YAG nonplanar ring lasers*, Appl. Opt. **47**, 6022 (2008). 41
- [106] P. Kwee, *Laser Characterization and Stabilization for Precision Interferometry*, PhD Thesis, Leibniz Universität Hannover, 2010. 41, 45, 46
- [107] H. Johnson and M. Graham, *High-speed signal propagation: advanced black magic* (Prentice Hall, 2003). 44
- [108] I. Freitag, A. Tünnermann and H. Welling, *Power scaling of diode-pumped monolithic Nd:YAG lasers to output powers of several watts*, Optics Communications **115**, 511 (1995). 46
- [109] B. Willke, *Stabilized lasers for advanced gravitational wave detectors*, Laser & Photonics Reviews **4**, 780 (2010). 46
- [110] R. Drever, J. Hall, F. Kowalski, J. Hough, G. Ford, A. Munley and H. Ward, *Laser phase and frequency stabilization using an optical resonator*, Applied Physics B **31**, 97 (1983). 46
- [111] A. Sawadsky, *Das Michelson-Sagnac-Interferometer mit SiN-Membran und Signal-recycling*, Master thesis, Leibniz Universität Hannover, 2012. 50, 51, 108
- [112] Newport Corporation, 1791 Deere Avenue, Irvine, California 92606 <http://www.newport.com>. 53, 57
- [113] N. Lastzka, Just another mode matching tool, 2011, <http://www.sr.bham.ac.uk/dokuwiki/doku.php?id=geosim:jammt>. 55
- [114] W. E. Newell, *Miniaturization of Tuning Forks*, Science **161**, 1320 (1968). 56
- [115] M. Bao, H. Yang, H. Yin and Y. Sun, *Energy transfer model for squeeze-film air damping in low vacuum*, Journal of Micromechanics and Microengineering **12**, 341 (2002). 56
- [116] D. Vitali, S. Gigan, A. Ferreira, H. R. Böhm, P. Tombesi, A. Guerreiro, V. Vedral, A. Zeilinger and M. Aspelmeyer, *Optomechanical Entanglement between a Movable Mirror and a Cavity Field*, Phys. Rev. Lett. **98**, 030405 (2007). 66

## BIBLIOGRAPHY

---

- [117] S. Mancini and P. Tombesi, *Quantum noise reduction by radiation pressure*, Phys. Rev. A **49**, 4055 (1994). 66
- [118] A. Freise and K. A. Strain, *Interferometer Techniques for Gravitational-Wave Detection*, Living Reviews in Relativity **13**, 1 (2010). 70, 87, 135
- [119] G. Heinzel, *Resonant Sideband Extraction Neuartige Interferometrie für Gravitationswellendetektoren*, Diploma thesis, Universität Hannover, 1995. 70, 86
- [120] Frequency domain INterFERometer Simulation Software, GPL3 license, <http://www.gwoptics.org/finesse/>. 73, 135
- [121] B. J. Meers, *Recycling in laser-interferometric gravitational-wave detectors*, Phys. Rev. D **38**, 2317 (1988). 74
- [122] K. A. Strain and B. J. Meers, *Experimental demonstration of dual recycling for interferometric gravitational-wave detectors*, Phys. Rev. Lett. **66**, 1391 (1991).
- [123] P. Fritschel, D. Shoemaker and R. Weiss, *Demonstration of light recycling in a Michelson interferometer with Fabry-Perot cavities*, Appl. Opt. **31**, 1412 (1992).
- [124] M. B. Gray, A. J. Stevenson, H.-A. Bachor and D. E. McClelland, *Broadband and Tuned Signal Recycling with a Simple Michelson Interferometer*, Appl. Opt. **37**, 5886 (1998).
- [125] J. Mizuno, *Comparison of optical configurations for laser-interferometric gravitational wave detectors*, PhD Thesis, Universität Hannover, 1995. 74
- [126] A. E. Siegman, *Lasers* (University Science Books, Sausalito, CA, 1986). 78
- [127] Heraeus Quarzglas GmbH & Co. KG, Product information sheet 2013, 2013, quarzstrasse 8, D-63450 Hanau, <http://www.optik.heraeus-quarzglas.com>. 81
- [128] Advanced Thin Films, Coating specifications, 2013, <http://www.atfilms.com>. 81
- [129] N. Uehara and K. Ueda, *Accurate measurement of ultralow loss in a high-finesse Fabry-Perot interferometer using the frequency response functions*, Applied Physics B **61**, 9 (1995). 86
- [130] S. Gröblacher, S. Gigan, H. R. Böhm, A. Zeilinger and M. Aspelmeyer, *Radiation-pressure self-cooling of a micromirror in a cryogenic environment*, EPL (Europhysics Letters) **81**, 54003 (2008). 89, 116

- [131] B. S. Sheard, M. B. Gray, C. M. Mow-Lowry, D. E. McClelland and S. E. Whitcomb, *Observation and characterization of an optical spring*, Phys. Rev. A **69**, 051801 (2004). 91
- [132] F. Khalili, *Frequency-dependent rigidity in large-scale interferometric gravitational-wave detectors*, Physics Letters A **288**, 251 (2001). 91
- [133] J. M. Aguirregabiria and L. Bel, *Delay-induced instability in a pendular Fabry-Perot cavity*, Phys. Rev. A **36**, 3768 (1987). 92
- [134] V. Braginsky, S. Strigin and S. Vyatchanin, *Parametric oscillatory instability in Fabry-Perot interferometer*, Physics Letters A **287**, 331 (2001).
- [135] F. Marquardt, J. G. E. Harris and S. M. Girvin, *Dynamical Multistability Induced by Radiation Pressure in High-Finesse Micromechanical Optical Cavities*, Phys. Rev. Lett. **96**, 103901 (2006). 100
- [136] T. J. Kippenberg, H. Rokhsari, T. Carmon, A. Scherer and K. J. Vahala, *Analysis of Radiation-Pressure Induced Mechanical Oscillation of an Optical Microcavity*, Phys. Rev. Lett. **95**, 033901 (2005). 92
- [137] S. Huang and G. S. Agarwal, *Reactive coupling can beat the motional quantum limit of nanowaveguides coupled to a microdisk resonator*, Phys. Rev. A **82**, 033811 (2010). 94
- [138] M. Li, W. H. P. Pernice and H. X. Tang, *Reactive Cavity Optical Force on Microdisk-Coupled Nanomechanical Beam Waveguides*, Phys. Rev. Lett. **103**, 223901 (2009). 94
- [139] A. Buonanno and Y. Chen, *Scaling law in signal recycled laser-interferometer gravitational-wave detectors*, Phys. Rev. D **67**, 062002 (2003). 95
- [140] S. P. Tarabrin, H. Kaufer, F. Y. Khalili, R. Schnabel and K. Hammerer, *Anomalous dynamic backaction in interferometers*, Phys. Rev. A **88**, 023809 (2013). 95, 96, 98, 134
- [141] S. L. Danilishin and F. Y. Khalili, *Quantum Measurement Theory in Gravitational-Wave Detectors*, Living Reviews in Relativity **15**, (2012). 95
- [142] T. Weiss, C. Bruder and A. Nunnenkamp, *Strong-coupling effects in dissipatively coupled optomechanical systems*, New Journal of Physics **15**, 045017 (2013). 98
- [143] M. Poot, K. Y. Fong, M. Bagheri, W. H. P. Pernice and H. X. Tang, *Backaction limits on self-sustained optomechanical oscillations*, Phys. Rev. A **86**, 053826 (2012). 100

## BIBLIOGRAPHY

---

- [144] T. M. Flynn, *Cryogenic Engineering*, 2 (CRC Press, Taylor & Francis Group, 2005). 110, 111, 116
- [145] K. Kuroda and the LCGT Collaboration, *Status of LCGT*, Classical and Quantum Gravity **27**, 084004 (2010). 110
- [146] ET Science Team, Einstein design study, 2011, <http://www.et-gw.eu/etdsdocument>. 110
- [147] G. Frossati, *Obtaining ultralow temperature by dilution of  $^3\text{He}$  into  $^4\text{He}$* , J. de Physique **39 (C6)**, 1578 (1978). 111
- [148] G. Ventura and L. Risegari, *The Art of Cryogenics: Low-Temperature Experimental Techniques*, 1 (Elsevier Science, 2007). 111
- [149] T. J. Kippenberg and K. J. Vahala, *Cavity Optomechanics: Back-Action at the Mesoscale*, Science **321**, 1172 (2008). 111
- [150] R. Moghadas Nia., *Kryogene Laserinterferometrie mit einer SiN-Membran*, Master thesis, Leibniz Universität Hannover, 2013. 111, 119
- [151] Janis Research Company, 2 Jewel Drive, Wilmington, MA 01887-3350 USA, <http://www.janis.com>. 111
- [152] H. O. McMahon and W. E. Gifford, *A new low-temperature gas expansion cycle*, Adv. Cryog. Eng. **5**, 354 (1960). 111
- [153] W. E. Gifford, The Gifford-McMahon cycle, 1965, cryogenic Engineering Conference, Houston Texas.
- [154] W. E. Gifford, *The Gifford-McMahon cycle*, Adv. Cryog. Eng. **11**, 152 (1966). 111
- [155] R. F. Barron, *Cryogenic Systems*, 2 (Oxford University press, 1985). 111
- [156] A. Waele, *Basic Operation of Cryocoolers and Related Thermal Machines*, Journal of Low Temperature Physics **164**, 179 (2011). 111
- [157] R. Radebaugh, *Cryocoolers: the state of the art and recent developments*, Journal of Physics: Condensed Matter **21**, 164219 (2009). 112
- [158] W. E. Gifford and H. O. McMahon, A Low Temperature Heat Pump, 1959, proc. of 10th Int. Cong. of Refrig. , Denmark 1959. 114
- [159] W. E. Gifford and T. E. Hoffman, in *A New Refrigeration System for 4.2 K* (Plenum Press, New York, 1961), Vol. 6, pp. 411–416. 114

- [160] R. Li, Y. Ikushima, T. Koyama, T. Tomaru, T. Suzuki, T. Haruyama, T. Shintomi and A. Yamamoto, in *Cryocoolers 13*, edited by J. Ross, RonaldG. (Springer US, 2005), pp. 703–710. 114
- [161] J. Gschneidner, K.A., A. Pecharsky and V. Pecharsky, in *Cryocoolers 12*, edited by J. Ross, RonaldG. (Springer US, 2002), pp. 457–465. 114
- [162] attocube systems AG, Product catalogue 2012/2013, 2012, <http://www.attocube.com>. 119
- [163] J. Steinlechner, *Optical absorption measurements for third generation gravitational wave detectors*, PhD Thesis, Leibniz Universität Hannover, 2013. 119
- [164] S. Tarabrin, 2013, personal communication. 138



## List of publications

### Publications within the Quantum interferometry group

- [Tarabrin] S. P. Tarabrin, **H. Kaufer**, F. Y. Khalili, R. Schnabel and K. Hammer, *Anomalous dynamic back-action in interferometers: beyond the scaling law*, Phys. Rev. A **88**, 023809 (2013)
- [Kaufer] **H. Kaufer**, T. Westphal, D. Friedrich and R. Schnabel, *Tomographic readout of an opto-mechanical interferometer*, New Journal of Physics, **14**, 095018, (2012).
- [Friedrich] D. Friedrich, **H. Kaufer**, A. Sawadsky., T. Westphal, K. Yamamoto, A. Sawadsky, F. Y. Khalili, S. Danilishin, S. Gossler, K. Danzmann and R. Schnabel, *Laser interferometry with coating-free mirrors*, New Journal of Physics **13**, 093017 (2011).
- [Westphal] T. Westphal, D. Friedrich, **H. Kaufer** K. Yamamoto, S. Gossler, H. Müller-Ebhardt, S. L. Danilishin, F. Y. Khalili, K. Danzmann and R. Schnabel, *Interferometer readout noise below the standard quantum limit of a membrane*, Phys. Rev. A, **85**, 063806, (2012).

### Publications within the LIGO Scientific Collaboration

- [lsc1] J. Aasi ... **H. Kaufer** ... J. Zweizig, *Search for gravitational waves from binary black hole inspiral, merger, and ringdown in LIGO-Virgo data from 2009-2010*, Phys. Rev. D, **87**, 22002, (2013).
- [lsc2] J. Aasi ... **H. Kaufer** ... D. P. Anderson, *Einstein@ Home all-sky search for periodic gravitational waves in LIGO S5 data*, Phys. Rev. D, **87**, 42001, (2013).
- [lsc3] J. Aasi ... **H. Kaufer** ... J. Zweizig, *Swift Follow-up Observations of Candidate Gravitational-wave Transient Events*, The Astrophysical Journal Supplement Series, **203**, 28, (2012).
- [lsc4] J. Aasi ... **H. Kaufer** ... J. Zweizig, *The characterization of Virgo data and its impact on gravitational-wave searches*, Classical and Quantum Gravity, **29**, 155002, (2012).
- [lsc5] J. Abadie ... **H. Kaufer** ... J. Zweizig, *All-sky search for gravitational-wave bursts in the second joint LIGO-Virgo run*, Phys. Rev. D, **85**, 122007, (2012).

## List of publications

---

- [lsc6] J. Abadie ... **H. Kaufer** ... J. Zweizig, *Search for gravitational waves from intermediate mass binary black holes*, Phys. Rev. D, **85**, 102004, (2012).
- [lsc7] J. Abadie ... **H. Kaufer** ... J. Zweizig, *Upper limits on a stochastic gravitational-wave background using LIGO and Virgo interferometers at 600-1000 Hz*, Phys. Rev. D, **85**, 122001, (2012).
- [lsc8] Abadie ... **H. Kaufer** ... J. Zweizig, *First low-latency LIGO+Virgo search for binary inspirals and their electromagnetic counterparts*, Astronomy & Astrophysics, **541**, (2012).
- [lsc9] J. Abadie ... **H. Kaufer** ... J. Zweizig, *Search for gravitational waves from low mass compact binary coalescence in LIGO's sixth science run and Virgo's science runs 2 and 3*, Phys. Rev. D, **85**, 82002, (2012).
- [lsc10] J. Abadie ... **H. Kaufer** ... J. Zweizig, *All-sky search for periodic gravitational waves in the full S5 LIGO data*, Phys. Rev. D, **85**, 22001, (2012).
- [lsc11] J. Abadie ... **H. Kaufer** ... W. Zheng, *Implementation and testing of the first prompt search for gravitational wave transients with electromagnetic counterparts*, Astronomy & Astrophysics, **539**, (2012).



# Acknowledgements

First, I would like to thank Prof. Karsten Danzmann, not only for leading this institute the way he does. His enthusiasm about physics is infectious and was one of the reasons I joined the field of laser interferometry.

I am grateful to Prof. Roman Schnabel for accepting me as a member in his group and for supervising my thesis. You managed to establish a great working group, I enjoyed being part of it and had the chance to work on a really exciting experiment.

For their excellent theoretical support, I would like to thank Prof. Klemens Hammerer and Dr. Sergey Tarabrin. It was great to work with you. I thank Gerhard Heinzl, who was always willing to answer some questions about signal-recycling. I would like to thank the master students I was allowed to accompany, Andreas Sawadsky and Ramon Moghadas Nia.

Most of my work would not have been possible without our excellent electronics and mechanical workshop, particularly not without Andreas Weidner, who was kind enough to ignore all the cruelties that might occur to the electronics in the laboratories.

For all the fun we had, I thank my PhD companions and bureau mates, Stefan Ast and Oliver Gerberding. I would not want to miss the time we had, both in and outside of the institute, although you made my Nerd-Level skyrocket. Not to forget the rest of the Mensa-crew: Amrit Pal-Singh, Heather Audley, Lisa Kleybolte and Melanie Meinders. I had good times with the grating group: Dr. Daniel Friedrich and Dr. Michael Britzger.

I want to thank all members of the Schnabel group, past and present for the pleasant working atmosphere. I would also like to thank our Postdocs Dr. Henning Vahlbruch and Dr. Moritz Mehmet, who were always willing to help in solving experimental problems and to provide electronics, which were still 'auf Täsch'. A lot of people were so kind to eliminate my enormous number of typos, thanks to all of you.

I am very fortunate for my family: my parents Angelika and Jürgen Käufer, who supported me during my entire life, both financially and in every decision I made, and my brother Steffen, on whom I can always rely. Thank you.

Marina, thank you for your love and encouragement, and for all your forbearing my not-so-good mood during the stressful periods in the past.



# Curriculum vitae

Henning Kaufer  
Buchenweg 1  
88690 Uhdlingen-Mühlhofen  
henningkaufer@gmx.de

Born on November 18th, 1983 in Lehrte, Niedersachsen

---

## University studies

- |                   |  |
|-------------------|--|
| 10/2013 - present | System engineer<br>Spacetechn GmbH, <a href="http://www.spacetechn-i.com">www.spacetechn-i.com</a> |
| 10/2009 - 10/2013 | Scientific assistant<br>Leibniz Universität Hannover   |
| 10/2009 - 10/2013 | Doctoral studies<br>Leibniz Universität Hannover   |
| 03/2008 - 3/2009  | Diploma thesis, <i>Herstellung und Charakterisierung lateraler Split-Gate Quantenpunkte</i>        |
| 10/2003 - 3/2009  | Physics studies,<br>Leibniz Universität Hannover   |

---

## Education

- |                 |                                    |
|-----------------|------------------------------------|
| 8/1996 - 7/2003 | Gymnasium Lehrte, Abschluss Abitur |
| 8/1994 - 7/1996 | Orientierungsstufe Lehrte-Süd      |
| 8/1990 - 7/1994 | Grundschule Ahlten                 |